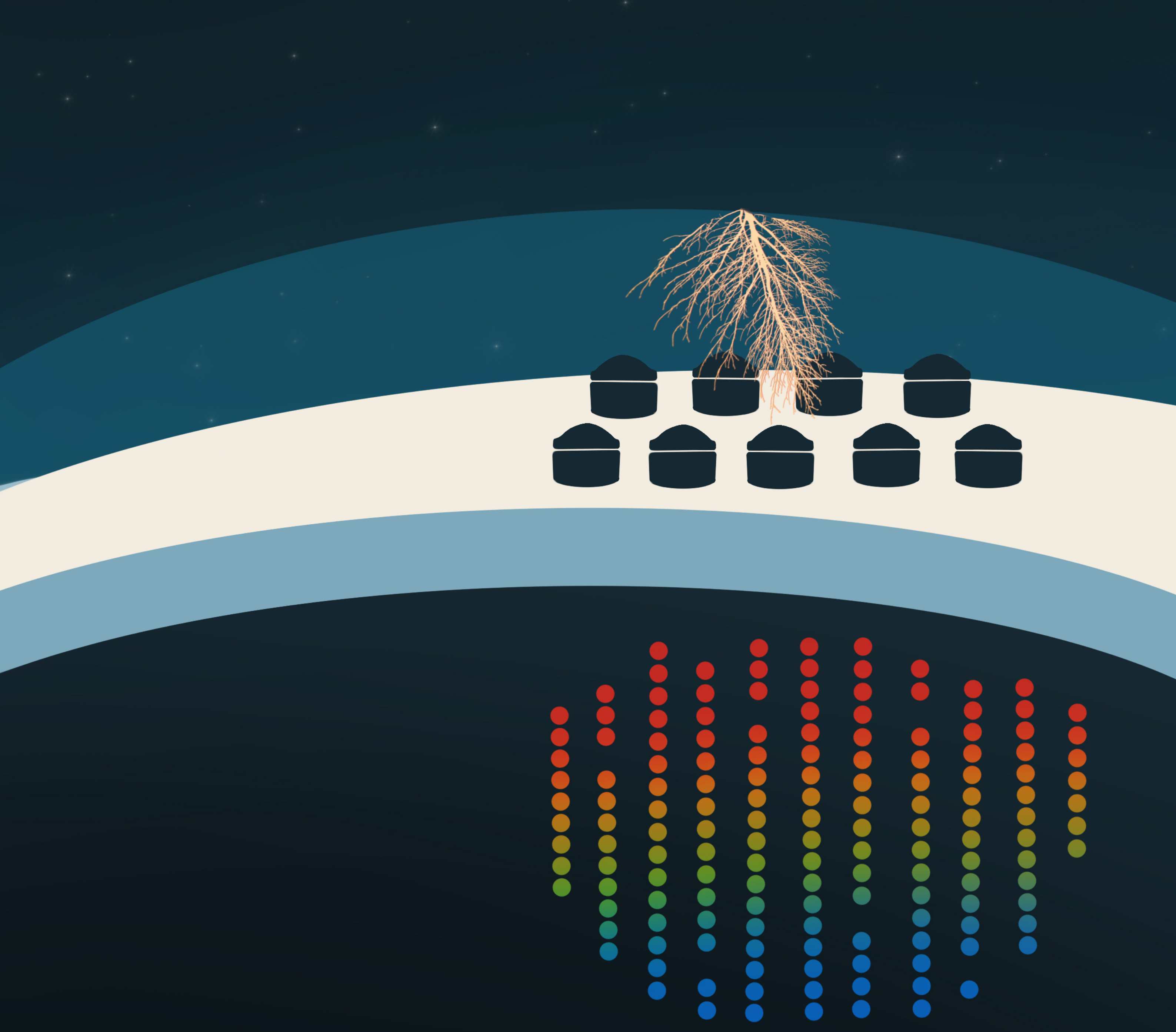

# ENHANCED GAMMA-HADRON SEPARATION AT THE ICECUBE NEUTRINO OBSERVATORY

Federico Bontempo

# Enhanced Gamma-Hadron Separation at the IceCube Neutrino Observatory

Zur Erlangung des akademischen Grades eines
DOKTORS DER NATURWISSENSCHAFTEN (Dr. rer. nat.)
von der KIT-Fakultät für Physik des
Karlsruher Instituts für Technologie (KIT)

genehmigte

DISSERTATION

von

Federico Bontempo
aus Chieti, Italien

| | |
|---|---|
| Tag der mündlichen Prüfung: | 06.06.2025 |
| Referent: | Prof. Dr. Schröder, Frank G.<br>(Associate Professor,<br>University of Delaware, USA) |
| Korreferent: | Prof. Dr. Engel, Ralph |

*A mamma, papà e Paolo,*

*ai miei nonni tutti,*

*a voi che avete creduto in me,*

*Grazie.*

# Abstract

Cosmic rays are energetic particles that constantly reach Earth and can produce air showers of secondary particles when interacting with the atmosphere. They mainly consist of charged nuclei. Additionally, neutral particles, e.g., gamma rays and neutrinos, also account for a percentage of the cosmic-ray composition. High-energy gamma rays are particularly interesting for this work, as they can be used to identify unknown sources of PeV Galactic cosmic rays. Due to their neutral charge, they point back to their astrophysical sources, unlike charged cosmic rays, which are deflected by magnetic fields.

The IceCube Neutrino Observatory is located at the geographic South Pole. The observatory consists of an in-ice optical array and a surface detector. The in-ice array covers a volume of 1 $km^3$ and is composed of more than 5,000 optical modules that measure the Cherenkov light generated by relativistic charged particles. The surface array, called IceTop, extends over a surface of 1 $km^2$ and consists of 81 pairs of Ice-Cherenkov tanks, which allow for the detection of cosmic rays from the sub-PeV to the EeV energy range. This work combines data from both detector parts to study cosmic rays, with a particular focus on gamma-hadron separation. The in-ice detector is used to detect high-energy muons, which are more abundant in the hadronic-generated air showers, and IceTop for the determination of differences in the footprint of the showers in the array.

Encouraged by the recent discovery of photons with energies up to PeV in the Northern Hemisphere, this analysis focuses on the near-PeV energy range. Newly produced simulations have been used for studies of detector efficiency and to develop a new reconstruction method for air showers in this energy range. The goal is to increase the number of observable gamma-ray events because of the larger flux in the near-PeV energy range.

Single pulses, which are measured by one of the two tanks in an IceTop station, have been used to define a new quantity, named Charged-Distance. The Charged-Distance has been investigated and used for improving the gamma-hadron separation, together with the information from the in-ice detector about the high-energy muon component of air showers. Combining the two quantities achieves a separation power of about $10^{-3}$ at 1 PeV, with an improvement of approximately one order of magnitude compared to a previous IceCube study.

With this improvement, IceCube has the potential to detect tens of gamma rays per year if a PeV-pevatron source, similar to the one in the Northern Hemisphere, happens to be within IceCube's field of view, enabling a great discovery potential for future point-source sky searches.

# Zusammenfassung

## Verbesserte Gamma-Hadron-Trennung am IceCube Neutrino-Observatorium

Kosmische Strahlung besteht aus energiereichen Teilchen, die stetig die Erde erreichen und bei Wechselwirkung mit der Atmosphäre Luftschauer aus Sekundärteilchen erzeugen. Sie besteht hauptsächlich aus geladenen Kernen. Zusätzlich tragen auch neutrale Teilchen, wie z. B. Gammastrahlen und Neutrinos, zur Zusammensetzung der kosmischen Strahlung bei. Hochenergetische Gammastrahlen sind dabei besonders interessant, da sie zur Identifizierung unbekannter Quellen galaktischer kosmischer Strahlung im PeV-Bereich verwendet werden können. Aufgrund ihrer neutralen Ladung weisen sie auf ihre astrophysikalischen Quellen zurück, im Gegensatz zu geladenen kosmischen Strahlen, die durch Magnetfelder abgelenkt werden.

Das IceCube Neutrino-Observatorium befindet sich am geografischen Südpol. Das Observatorium besteht aus einer Anordnung von optischen Sensoren im Eis und einem Oberflächendetektor. Das Messfeld im Eis umfasst ein Volumen von 1 km$^3$ und besteht aus mehr als 5.000 optischen Modulen, die das von relativistischen geladenen Teilchen erzeugte Cherenkov-Licht messen. Das Oberflächen-Array IceTop erstreckt sich über eine Fläche von 1 km$^2$ und besteht aus 81 Paaren von Eis-Cherenkov-Tanks, die den Nachweis von kosmischer Strahlung vom Sub-PeV- bis zum EeV-Energiebereich ermöglichen. In dieser Arbeit werden die Daten beider Detektoren kombiniert, um die kosmische Strahlung zu untersuchen, wobei der Schwerpunkt auf der Trennung von primären Gammas und Hadronen liegt. Der Detektor im Eis dient der Detektion hochenergetischer Myonen, die in hadronisch erzeugten Luftschauern häufiger vorkommen als in Luftschauern initiiert von primären Gammas. IceTop wird benutzt zur Bestimmung von Unterschieden im Fußabdruck der Schauer in den Teilchendetektoren.

Angeregt durch die jüngste Entdeckung von Photonen mit Energien bis zu PeV, konzentriert sich diese Analyse auf diesen Energiebereich. Neu erstellte Simulationen wurden für Untersuchungen der Detektoreffizienz und zur Entwicklung einer neuen Rekonstruktionsmethode für Luftschauer in diesem Energiebereich verwendet. Ziel ist es, die Anzahl beobachtbarer Gammastrahlenereignisse aufgrund des größeren Flusses im Energiebereich knapp unterhalb PeV zu erhöhen.

Einzelne Pulse, die von einem der beiden Tanks einer IceTop-Station gemessen werden, wurden zur Definition einer neuen Größe namens „Charged Distance“ verwendet. Diese wurde untersucht und zur Verbesserung der Gamma-Hadron-Trennung genutzt, zusammen mit den Informationen des In-Ice-Detektors über die hochenergetische Myonenkomponente von Luftschauern. Durch die Kombination der beiden

Größen wird eine Trennung von etwa $10^{-3}$ bei 1 PeV erreicht, was eine Verbesserung von etwa einer Größenordnung im Vergleich zu einer früheren IceCube-Studie darstellt.
Mit dieser Verbesserung hat IceCube das Potenzial, Dutzende von Gammastrahlen pro Jahr zu erfassen, wenn sich eine PeV-Pevatron-Quelle, ähnlich den bereits detektierten auf der Nordhalbkugel, im Sichtfeld von IceCube befindet. Dies eröffnet ein großes Entdeckungspotenzial für zukünftige Himmelssuchen nach Punktquellen in der südlichen Hemisphäre.

# Contents

# Introduction

Cosmic-ray physics began in the early 20th century with Victor Hess's now-famous balloon experiments. In 1912, he reached altitudes of up to 5,300 meters to investigate the origin of ionizing radiation detected on Earth. He discovered that radiation levels increased significantly with altitude, indicating an extraterrestrial origin of the former [1]. This discovery opened the doors for studies and experiments in cosmic-ray physics.

Cosmic rays are high-energy particles that originate from outer space, constantly reaching Earth and interacting with the atmosphere. They can be charged particles such as protons, atomic nuclei, or electrons, and also give rise to neutral particles, in particular, gamma rays or neutrinos [2]. They span a vast energy range, from a few MeV to ultra-high energies: up to a few $10^{17}$ eV for cosmic rays from the Galaxy and exceeding $10^{20}$ eV for extra-galactic cosmic rays [3]. Identifying and studying cosmic rays arriving on Earth is crucial for understanding their origins, acceleration mechanisms, and interactions with interstellar media, providing insights into the most energetic astrophysical phenomena, such as supernova remnants, active galactic nuclei, and gamma-ray bursts. These only partially understood phenomena remain one of the fundamental challenges in modern astrophysics.

Gamma rays and neutrinos are not deflected by magnetic fields, and they are generated as a secondary product of interactions of charged cosmic rays with the interstellar medium or matter at sources. In particular, ultra-high-energy (UHE) gamma rays, with energies larger than 100 TeV, originate from interactions of highly energetic charged particles, accelerated by the cosmic-ray sources. Thus, they can offer crucial insights into the mechanisms driving particle acceleration and production mechanisms because, due to their neutrality, they travel undeflected through the galaxy and are ideal candidates for direct source identification.

The detection of cosmic rays and gamma rays up to $10^{11}$ eV can be performed by direct measurements with space-based instruments like Fermi-LAT [4]. Starting from a few tens of GeVs, they can be detected using indirect measurements with ground-based observatories such as LHAASO [5], H.E.S.S. [6], and CTA [7]. Over the years, they provided important insights into the observation of gamma rays, ranging over several orders of magnitude. However, despite the extensive observational efforts that have refined our understanding of cosmic rays and their associated gamma-ray emissions, fundamental questions remain open, e.g., the acceleration mechanisms and the leptonic or hadronic nature of gamma-ray sources.

Recent observations from ground-based air-shower arrays, such as LHAASO and HAWC [8], have identified sources that emit photons at energies beyond 100 TeV, pushing the boundaries of gamma-ray astronomy into the PeV regime. Identifying PeV gamma-ray sources helps the understanding of the highest-energy cosmic accelerators and production in the Galaxy.

LHAASO has measured a population of UHE gamma rays from Galactic sources with energies up to PeV. However, such energetic photons have yet to be observed in the southern sky.

The location of the IceCube Neutrino Observatory [9] at the geographic South Pole is perfect for studying the southern sky. The IceCube Neutrino Observatory is composed of two detector arrays: an in-ice detector array and a surface array called IceTop. The in-ice array measures high-energy charged particles generated in the air-shower development or via the neutrino interaction in the ice. IceTop serves as a veto for neutrino detection and a detector for cosmic-ray air showers. Hence, despite IceCube being built for the neutrino search, the combination of both the in-ice and the surface detector can be exploited for the hunt for gamma-ray sources.

However, detecting PeV gamma-ray air showers is challenging due to their low flux and high background from charged cosmic rays. The goal of this thesis is to identify gamma-ray air showers against air showers initiated by protons and atomic nuclei, with a particular focus on gamma-hadron separation in the sub-PeV energy range. Improved reconstruction methods can extend the sensitivity to lower energies compared to earlier analyses and enhance the gamma-hadron separation with IceCube. Using simulations of air showers, a dedicated low-energy reconstruction method is developed. The expected flux from realistic emission scenarios is estimated based on known LHAASO sources, and, ultimately, the methodology for effective gamma-hadron separation is significantly improved over previous approaches.

In this thesis, Chapter 1 and Chapter 2 give a brief introduction to the cosmic-ray theory and the IceCube Neutrino Observatory, respectively. Chapter 3 presents an overview of the simulated and measured datasets used for this analysis. Chapter 4 introduces the reconstruction method for air showers detected with IceTop and the new low-energy reconstruction method. Chapter 5 explains the importance of calibration for signals from only one of the two tanks in an IceTop station and implements an approach to calibrate them for low-energy air showers. Finally, Chapter 6 describes the new method of gamma-hadron separation based on the combination of in-ice and IceTop.

# 1. Cosmic Rays

This chapter provides a general introduction to cosmic rays, which is the basis of the work carried out in this thesis. It presents the cosmic-ray energy spectrum, their expected production sources, and mechanisms. Following this, the interaction of cosmic rays with the atmosphere will be discussed, highlighting the differences between atmospheric particle cascades initiated by gamma-ray and hadronic interactions. Finally, the chapter will address gamma-hadron separation and state the main motivations for the research done for this thesis. The primary source and reference for this chapter is [2], unless otherwise stated.

## 1.1. Introduction to cosmic rays

The term "cosmic rays" broadly refers to all particles arriving at Earth from space. Their origin and production are not fully understood, making astroparticle physics an active field of research. The flux of cosmic rays on Earth has a frequency of about 1000 particles per second per square meter. The particles that compose the flux are mainly ionized protons, which constitute about 90% of the entire flux. Approximately 9% are made of alpha particles and the remaining 1% are heavy ionized nuclei. Equally interesting is the energy of such particles. As will be discussed in Section 1.2, the energy spectrum follows a power law and extends for orders of magnitude, reaching energies beyond $10^{20}$ eV.

Cosmic rays are correlated with their production in the sources and the surrounding medium. The production of secondary cosmic rays, via interactions with the interstellar medium (ISM), gives valuable insight into the composition of the ISM as well as the propagation of the cosmic rays from the source to Earth. Photons and neutrinos are among the most interesting secondary particles, since, due to their charge neutrality, they are not deflected by magnetic fields. This can enable the identification of possible sources of cosmic rays and subsequently improve the understanding of acceleration mechanisms. The interaction mechanisms that take place in the interstellar medium are of a similar nature to the interaction of cosmic rays with the Earth's atmosphere. In interaction with the Earth's atmosphere, high-energy cosmic rays lead to the production of secondary particles, which in turn develop into a cascade of particles on further interactions. This process generates a so-called "air shower". This topic will be further discussed in Section 1.5.

Cosmic-ray experiments can explore various themes ranging from CR composition, energy spectra, arrival direction, and more. The composition studies offer crucial insights into the diverse abundance of particles and, consequently, the possible interactions that occur in the ISM. Energy spectra can elucidate the attributes of the distinct acceleration processes that particles experience in their origin environment. Lastly, examining the arrival direction can provide information about whether the cosmic-ray distribution is isotropic or anisotropic.

## 1.2. The cosmic ray energy spectrum

The cosmic-ray energy spectrum ranges over multiple orders of magnitude, approximately following a power-law distribution. Thus, the flux of high-energy particles is orders of magnitude lower than at lower energies. Consequently, the measurement of cosmic rays differs depending on the energy. Mainly, the detections can be classified into two categories, direct measurement and indirect measurement. Direct measurements are given by satellites or balloons, which can detect the cosmic rays high up in the atmosphere or in space before any interaction. Indirect measurements are usually performed for high-energy cosmic rays using ground-based detectors measuring the secondary particles generated via the interaction of the primary cosmic rays in the atmosphere.

Satellite experiments are usually small in size because of the high cost of sending and maintaining experiments in space. Thus, the flux measured is limited by their volume. They usually perform calorimetric or spectrometric measurements in a magnetic field, allowing for a combined composition and energy measurement. Because of the small size, they are usually only able to set upper limits at energies above TeV-PeV, depending on the detector. Hence, indirect measurements are used for cosmic rays above TeV, more on this in Section 1.5.

As previously mentioned, cosmic ray energies span several orders of magnitude. Typically, the spectral index is approximately $\gamma = -3.0$. However, as illustrated in Figure 1.1, variations in the spectral index become evident when the spectra are multiplied by energy, specifically $E^2$. The spectrum is harder with $\gamma = -2.7$ for energies between 10 GeV and 1 PeV, and it softens to $\gamma = -3.1$ for energies from 10 PeV to 1 EeV. Notably, a spectral flattening occurs with an approximate $\gamma = -2.6$ before the cutoff around $10^{20}$ eV.

Several other regions and features characterize the spectrum. The region at around 3 PeV, known as the knee [26], is thought to be related to the maximum energy achievable by galactic accelerators (like supernova remnants) or due to propagation effects in

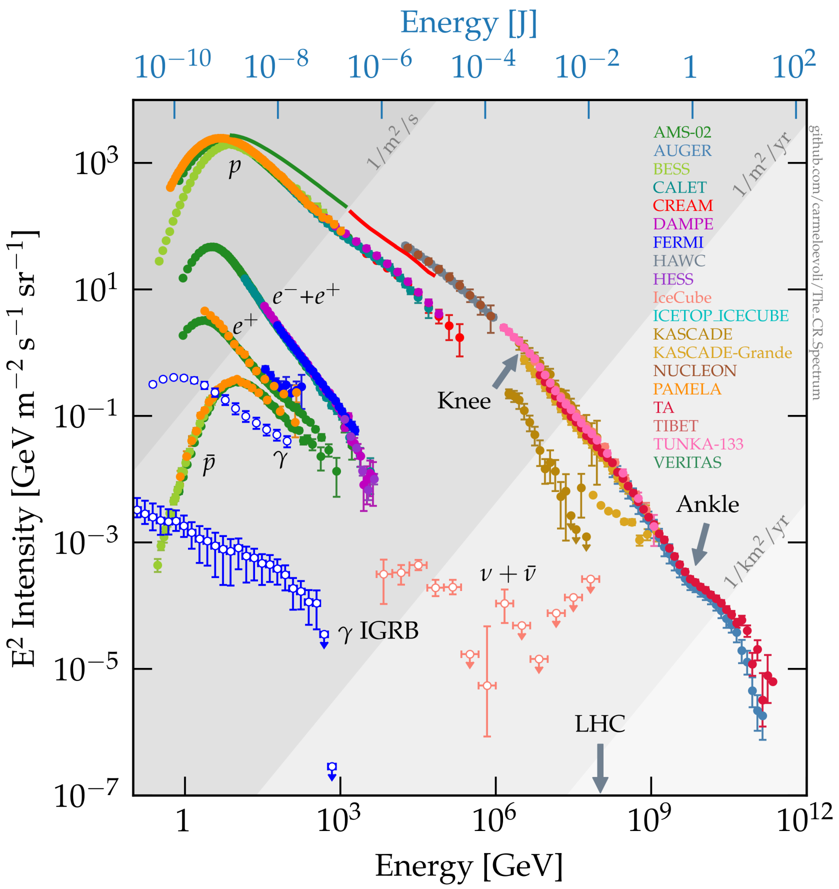

Figure 1.1.: Spectrum of cosmic rays: The flux is scaled by $E^2$. Notable structures, known as the knee and the ankle, occur at 3 PeV and 3 EeV, respectively [10, 11, 12, 13, 14, 15, 4, 8, 6, 16, 9, 17, 18, 19, 20, 21, 22, 23, 24]. Taken from [25].

the interstellar medium. A second transition region called the second knee [27] is visible around $10^{17}$ eV. This region may indicate the end of the heaviest galactic cosmic rays and the start of extra-galactic cosmic rays. Finally, an ankle feature is observed around 3 EeV and may be caused by the interaction of extragalactic cosmic rays with the cosmic microwave background (CMB).

The spectrum observed by high-energy cosmic rays provides insights into atmospheric interactions and the production of secondary particles like hadrons, muons, and neutrinos. In addition, it offers valuable information on cosmic-ray production, their acceleration sources, and propagation mechanisms.

The composition of cosmic rays has an energy dependence, and their study may provide an understanding of their origin, production, and propagation [9, 28]. Figure 1.2 shows the cosmic-ray energy spectrum and composition plot. This is Global Spline Fit [29] and combines direct and indirect measurement, thereby adjusting for differences in the energy scale of the experiments. The all-particle flux is shown with the black solid line, and the red, yellow, green, and blue lines indicate proton, helium, oxygen, and iron group, respectively. The $1\sigma$ uncertainty regions for each component are also shown for each mass component with shaded bands. The top right plot in the inset panel shows the variation of the mean logarithmic mass ($\langle \ln A \rangle$) as a function of energy. Known features of the knee, second knee, ankle, and the mass transition from light to heavy elements at higher energy are visible.

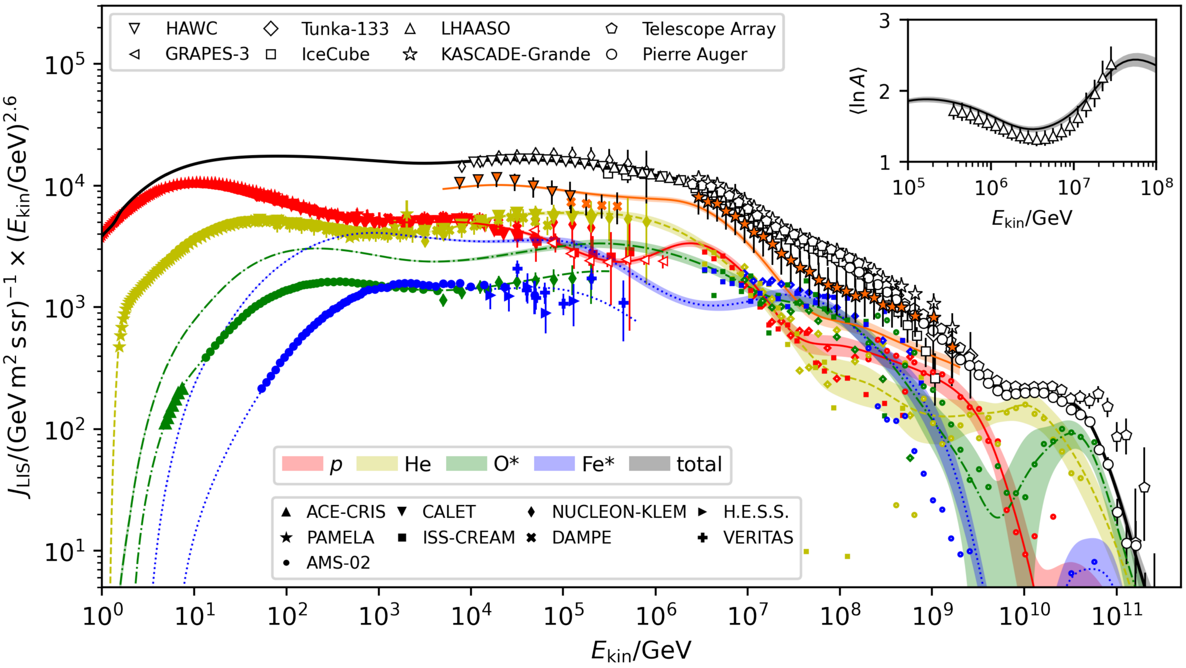

Figure 1.2.: The spectrum of cosmic rays and their composition in four mass groups. Taken from [29].

## 1.3. Production and propagation of cosmic rays

The production and acceleration processes of cosmic rays are linked to their sources and the surrounding environment [30]. Their exact origin is still under debate, but probably linked to violent astrophysical events. Sources can be found both inside and outside our Galaxy and, hence, classified as galactic or extragalactic. In the Milky Way galaxy, the most accredited candidates for cosmic-ray production are supernovae. On the other hand, active galactic nuclei (AGN) are believed to be a source of extragalactic cosmic rays. Other candidates include binary neutron star mergers and starburst galaxies [31].

### 1.3.1. Production of cosmic rays

The high-energy blast wave generated in supernova explosions makes supernova remnants (SNR) good candidates for galactic cosmic-ray sources. For example, a Type II supernova, with an original mass of approximately 10 solar masses and a velocity of $v \approx 5 \times 10^8\,\mathrm{cm/s}$, has an estimated luminosity $L_{\mathrm{SN}} \approx 3 \times 10^{42}\,\mathrm{erg/s}$ over about 30 years. For this luminosity to match the observed cosmic ray luminosity of $L_{\mathrm{CR}} \approx 7 \times 10^{40}\,\mathrm{erg/s}$, only a small fraction of the total energy needs to be transferred to cosmic-ray acceleration, confirming SNRs as a good candidate for the source cosmic-rays acceleration.

Supernovae accelerate cosmic rays due to their shockwave sweeping up the particles in the interstellar medium (ISM). The angle of interaction between these particles and the shockwave determines whether particles are accelerated or decelerated. In the case of an infinite plane shock approximation, the angles are constrained such that the interactions consistently result in an energy gain. A complete calculation of the expected spectral index for the acceleration in the SNR shock waves results in $\gamma = -2$. This spectral index, with the addition of the propagation index, is consistent with the cosmic rays observed on Earth and provides additional support for the candidature of supernovae as cosmic-ray sources.

The propagation or acceleration of cosmic rays is correlated to the magnetic field strength in the environment of the source. Assuming a magnetic field of $B_{\mathrm{ISM}} \approx 3\,\mu\mathrm{G}$, the maximum acceleration achievable is $E_{\mathrm{max}} \leq Z \times 3 \times 10^4\,\mathrm{GeV}$, where $Z$ is the atomic number. This estimation under-predicts the required maximum energy by a factor of 30 to 100. The main cause of this is likely due to two factors. First, the magnetic field within the supernova blast could be much stronger than that of the interstellar medium, potentially around $B_{\mathrm{SN}} \approx 100\,\mu\mathrm{G}$ [32]. Secondly, the magnetic field may vary significantly across the region with a non-linear behavior. Taking into account those reasonable, realistic scenarios, the higher magnetic field could account for the acceleration of protons up to $E_{\mathrm{max}} \approx 1\,\mathrm{PeV}$. This energy is still insufficient to explain the production of Galactic cosmic rays up to $\approx 10^{17}$ eV, leaving the production of the most energetic Galactic cosmic rays an open research topic [33].

### 1.3.2. Propagation of cosmic rays

The propagation of cosmic rays can be analyzed by studying the ratio between primary (produced in the source) and secondary (produced during propagation) particles. The ratio provides insights into the time particles spend traveling throughout the Galaxy. One example is the carbon and boron ratio. Studying this ratio $B/C$, under the assumption that no boron is produced in the sources, it is possible to estimate the time the cosmic ray spent in the Galaxy before reaching Earth.

The Milky Way can be approximated as a disk with an average transverse grammage of about $10^{-3}\,\mathrm{g/cm^2}$. Based on the ratio of the estimated grammage of $5-10\,\mathrm{g/cm^2}$ (equivalent to hydrogen) traversed by cosmic rays from injection to detection and the density of the Galaxy, it is clear that cosmic rays travel multiple times through the galactic disk before observation. Furthermore, the comparison of low-energy to high-energy particles reveals that the effective grammage (the amount of matter traversed) is inversely proportional to energy, showing that higher-energy particles traverse less matter and consequently spend less time in the interstellar medium.

Figure 1.3 shows $B/C$ as a function of energy. Under the assumption that no boron is produced in the sources, it is clear that the higher the energy, the lower the amount of boron. This means that a lower fraction of carbon atoms interacted with the ISM, implying that the high-energy carbon atoms spent less time in the Galaxy.

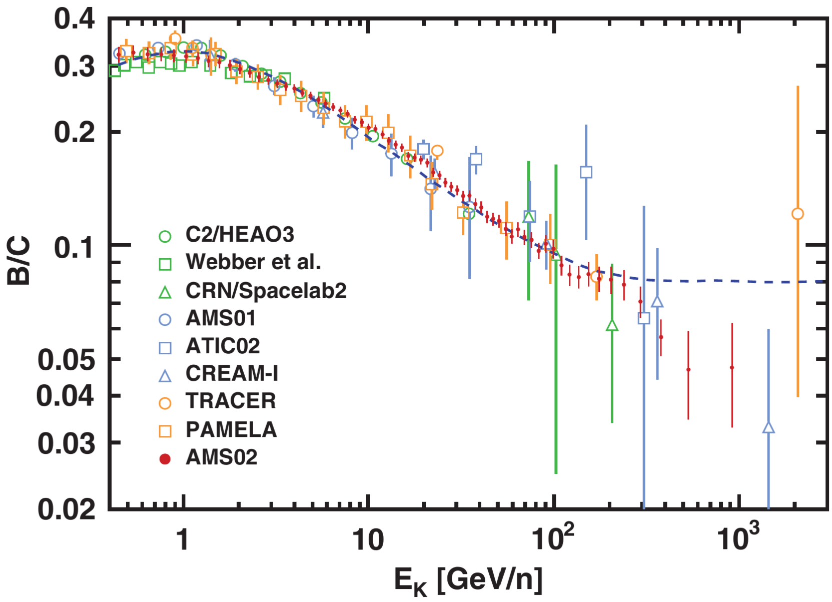

Figure 1.3.: Ratio between boron and carbon B/C. This shows that the higher energetic particles spend less time in the Galaxy than the lower energetic ones. Taken from [34].

In conclusion, all nuclei travel a relatively large amount of grammage before reaching Earth. Because of their charge, they are susceptible to Galactic magnetic fields, which limit their capability to point back to the source. Even if less prominent, this effect is still present at ultra-high energies, weakening the anisotropy in the arrival direction [35, 36]. For this reason, charged cosmic rays cannot be reliably used for source identification.

## 1.4. Gamma rays

The most reliable way to point to the astrophysical sources of cosmic rays is to use neutral particles, namely gamma rays and neutrinos. Because of their neutral state, they are undeflected by the magnetic fields and hence point back to the source of their origins within our Galaxy.

### 1.4.1. Production of gamma rays

Gamma rays and photons in general can be produced through a variety of mechanisms. At very high energy and beyond, two main processes dominate the gamma-ray production: $\pi^0$ decay and Inverse Compton scattering. When accelerated particles interact with the interstellar medium (ISM), they usually produce unstable secondary particles. For instance, hadronic interactions of protons can produce neutral pions that further decay into gammas $\pi^0 \rightarrow \gamma\gamma$. The Inverse Compton scattering is a leptonic acceleration process. High-energy electrons transfer energy to the cosmic-microwave-background photons, boosting them into the gamma-ray regime. This is especially relevant in environments with abundant photon fields and relativistic particle populations, for example, near pulsars or supernova remnants. These two processes are fundamental in distinguishing hadronic and leptonic cosmic ray production. Investigating the production and understanding of which process dominates a specific source is a key component of ultra-high-energy gamma-ray research [37].

In the MeV energy range, photons are mainly produced via other processes, namely Bremsstrahlung and Compton effects. Bremsstrahlung radiation is obtained via the deceleration of charged particles. Electrons are slowed down by the interaction with the atoms, resulting in photon emission. In the Compton effect, an energetic photon scatters away the loosely bound electron of an atom. The electron gains kinetic energy, and the photon loses energy from the process. Bremsstrahlung and Compton effect are typically less relevant in the ultra-high-energy range, but contribute to the lower-energy gamma-ray spectrum.

At energies exceeding a few MeV, photons themselves begin to interact with matter through pair production. A photon is converted into an electron-positron pair upon interaction with a nucleus. This interaction becomes increasingly important as the energy of the gamma rays rises, and will be a key point for the development of an air shower, discussed in Section 1.5.

### 1.4.2. Emissivity and kinematics of gamma rays

For energies above 100 TeV, the neutral pion ($\pi^0$) decay process is the main source of gamma-ray production. This section briefly presents the emissivity, luminosity, kinematics, and the correlation between $\pi^0$ and gamma rays.

The emissivity of the neutral pion $q_{\pi^0}$ can be expressed as follows:

$$q_{\pi^0} = 4\pi\sigma_{pp} \left\{ Z_{p\pi^0} \right\} N_0 \left( E_\pi \right), \tag{1.1}$$

where $Z_{p\pi^0}$ is the spectrum-weighted moment $p \to \pi^0$ of the inclusive proton-proton cross sections $\sigma_{pp}$, and $N_0\,(E_\pi)$ is the power-law approximation for the differential spectrum of nucleons evaluated at the pion energy $E_\pi$. The expected isotropic flux is given by the factor $4\pi$.

Via the convolution with the kinematics of $\pi^0 \to \gamma\gamma$, it is possible to calculate the gamma-ray emissivity $q_\gamma$ and consequently the luminosity of gamma rays $\mathscr{L}_\gamma$:

$$\mathscr{L}_\gamma \approx n_H V_{\mathrm{MW}} \int_{0.1\,\mathrm{GeV}} E_\gamma q_\gamma(E_\gamma)\,\mathrm{d}E_\gamma \approx 10^{39}\,\mathrm{erg/s}, \tag{1.2}$$

where $n_H$ is the density of protons in the interstellar medium (assumed to be 1 hydrogen atom per cm $^3$), and $V_{\mathrm{MW}}$ the volume of the Milky Way.

The kinematics of the decay in the laboratory frame can be calculated from the reference system of the center of mass (CM). In the CM frame, the $\pi^0$ is at rest, and two gamma rays $\gamma$ are produced in opposite directions, isotropically. Each gamma ray will have an energy equivalent to half the rest mass of the pion, i.e.,

$$E_\gamma = \frac{m_{\pi^0}}{2} \approx 70\,\mathrm{MeV}. \tag{1.3}$$

For energies above 100 TeV, the kinetic energy of the pion is much larger than its rest mass ($E_k \gg m_{\pi^0}$). Furthermore, the energy of the gamma rays in the laboratory frame depends on their opening angle $\theta^*$. Specifically, the cosine of $\theta^*$ must satisfy $-1 \leq \cos(\theta^*) \leq 1$. Hence, the energy of the gamma-ray in the lab frame is bounded by:

$$m_{\pi^0}\sqrt{\frac{1-\beta}{1+\beta}} \leq E_\gamma \leq m_{\pi^0}\sqrt{\frac{1+\beta}{1-\beta}}, \tag{1.4}$$

where $\beta = \frac{v_{\pi^0}}{c}$, the velocity of the pion in units of the speed of light.

## 1.5. Air showers

In the energy range above $10^{13}$ eV, the direct detection of cosmic rays becomes challenging with the current technology. The large volume of the satellite detector required for measurements makes it hard to send and maintain the modules in space. Despite this, the detection of cosmic rays at these and higher energies can still be performed indirectly via the measurement of the secondary particles produced in atmospheric interactions. Cosmic rays in fact interact with the Earth's atmosphere and generate a so-called "air shower". Figure 1.4 shows a simplified representation of an air shower reaching the detector at the ground.

The air shower development in the atmosphere depends on many factors, for example, the type of primary particle, its energy, or the angle of interaction with respect to the zenith. Regardless, all the secondary particles will interact again, generating further particles. This process will increase the number of particles exponentially until a critical energy is reached, at which point the number of particles starts to decrease. This mechanism is well-known and described by the Heitler model.

Figure 1.4 shows a sketch of an air shower and some of its components. The secondary particles produced after the interaction of the primary cosmic rays in the atmosphere are discussed in the next sections.

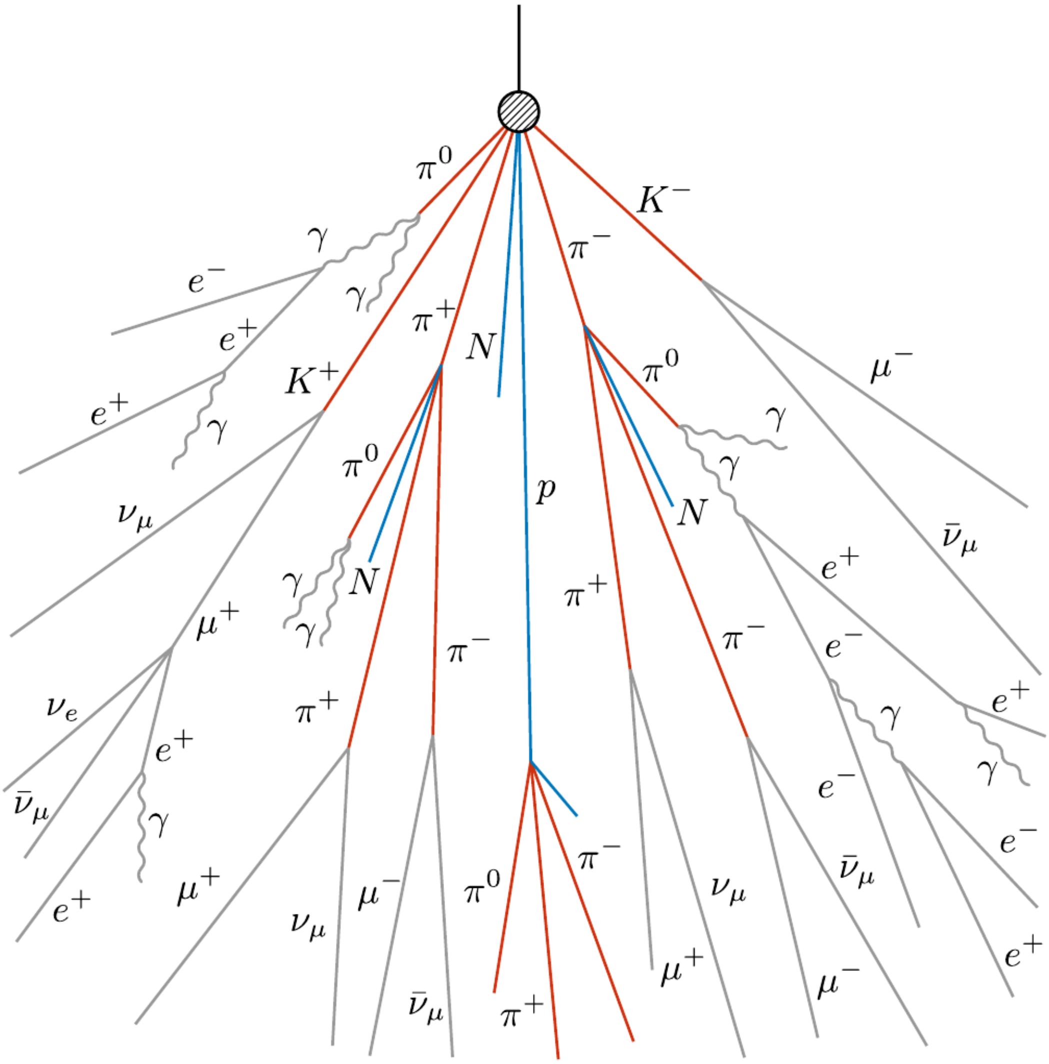

Figure 1.4.: Sketch of a cosmic ray air-shower. Taken from [38].

## 1.5.1. The electromagnetic cascade

The simplified Heitler model can describe, in first approximation, showers generated by a gamma-ray or an electron primary. It models exclusively the electromagnetic component of the air shower, described by pair production of electrons and positrons, and does not include muon production.

$$\gamma \rightarrow e^- + e^+, \tag{1.5}$$

and:

$$e^\pm \rightarrow e^\pm + \gamma. \tag{1.6}$$

Equations 1.5 and 1.6 show that the only elements taking part in the interactions are $\gamma$ and $e^\pm$. This enables the determination of the total number of particles as a function of the atmospheric depth $X$ with a simple power law. The modeling of the number of particles also depends on initial parameters such as the energy of the primary or the angle with respect to the zenith. The number of particles can be modeled by a power law function and calculated as a function of the total number of interactions. The branching occurs after each collision length $\lambda$. Thus, the total number of branches is $n = X/\lambda$. Consequently, the total number of particles is $N(X) = 2^{X/\lambda}$. Finally, the average energy per "particle" is:

$$E(X) = E_0/N(X). \tag{1.7}$$

The splitting process continues until the critical energy per "particle" $E_c \approx 87$ MeV is reached. At this point, the maximum number of particles is reached. Thus, the maximum number of particles at the shower depth $X_{\max}$ will be $N(X_{\max}) = E_0/E_c$. Consequently, the height at which the maximum is reached is:

$$X_{\max} = \lambda \frac{\ln(E_0/E_c)}{\ln 2}. \tag{1.8}$$

After reaching $E_c$, the shower will no longer increase in size, but rather start losing energy, and the number of particles decreases. This happens mainly because of energy loss via Bremsstrahlung and ionization.

## 1.5.2. Hadronic air showers

Hadronic air showers have a more complex development than showers induced by gamma rays. As discussed in Section 1.5.1, gamma-ray air showers are mainly electromagnetic. However, a more general and accurate representation of shower development also has to consider the hadronic and muonic components. They are primarily the result of hadronic interactions in the atmosphere.

Charged mesons and neutral pions are the main ones responsible for the electromagnetic and the muonic components, respectively. The $\pi^0$ generated by the hadronic interaction decays into 2 photons that start electromagnetic sub-showers: $\pi^0 \to \gamma + \gamma$. The muonic component is primarily fed by the decay of charged $\pi^\pm$ and kaons $\kappa^\pm$.
Almost a third of the hadronic interactions go into the electromagnetic component of the air shower, thus, the predominant energy dissipation comes from the electron and positron ionization losses. The maximum number of particles is energy-dependent. Generally, the electromagnetic component is about 90% and the muonic about 10% of the total energy content. After reaching the maximum number of particles in the atmosphere, the number of electrons and positrons starts decaying rapidly. This is because ionization and bremsstrahlung become predominant. The muons in the hadronic component decay slowly, leading to a slow decline in the number of muons. This is because of the low interactions that muons have in the atmosphere. Furthermore, the secondary hadrons and the subsequent muons coming from low-energy $\pi^\pm$ decays will have a larger transverse momentum, resulting in a larger spread of the air shower. On the other hand, the electromagnetic component is more contained because the photons generated by the decays of $\pi^\pm$ generate gammas are nearly parallel to the hadronic core at the shower axis.

### 1.5.3. The Heitler-Matthews splitting model

Matthews generalized the Heitler model, including the hadronic component of the air shower. Given an initial energy $E_0$ and a number of interactions $n_{\text{tot}}$, the energy per particle can be estimated as $E_0/n_{\text{tot}}$. The total number of particles would be approximately divided into 2/3 as charged and 1/3 as neutral. Thus, at iteration $n$, the energy can be calculated as follows:

$$E_{had} = \left(\frac{2}{3}\right)^n E_0 \tag{1.9}$$

and

$$E_{em} = \left[1 - \left(\frac{2}{3}\right)^n\right] E_0 \tag{1.10}$$

After $n \approx 6$ iterations, the electromagnetic component will carry 90% of the energy. The electromagnetic component will increase until the critical energy $E_c \approx 87$ MeV. Afterward, the number of electromagnetic particles starts to decrease because of the ionization losses. The number of muons, on the other hand, almost exclusively depends on the primary energy and is usually determined via simulations and numerical approximations. An estimation of the number of muons with energy larger than 1 GeV can be calculated as follows:

$$N_\mu(> 1\text{GeV}) \approx 10 \left(\frac{E_0}{\varepsilon_\pi}\right)^{0.9}. \tag{1.11}$$

The composition of cosmic rays is still not fully understood and is expected to vary with energy. However, a significant fraction of cosmic rays is made of nuclei, not single atoms. For nuclei, the binding energy is $< 10$ MeV, much smaller than the total energy of the primary nuclei. This means that the total energy can be equally divided between all nucleons after the first interaction. Thus, given an initial energy $E_0$ and a nuclear mass number $A$, the energy for each nucleon can be calculated as $E_h = E_0/A$. The development of the shower also depends on the primary mass, i.e., the number of nucleons. The heavier the primary particle, the higher the muon content and the earlier the shower maximum is reached. It is worth noticing that, given a fixed initial energy, the total number of particles generated is independent of the primary mass. However, the position of the maximum depth in the atmosphere $X_{\max}$ depends on the primary nucleus. For example, protons reach the maximum number of particles between 80 to 100 g/cm$^2$:

$$X_{\max} \propto \lambda \log\left[\frac{E_0}{AE_c}\right] \tag{1.12}$$

The mass number $A$ in Eq. 1.12 shows a dependence in the shower development depending on the primary mass. In particular, air showers initiated by lighter nuclei will reach a maximum lower in the atmosphere compared to heavier ones.

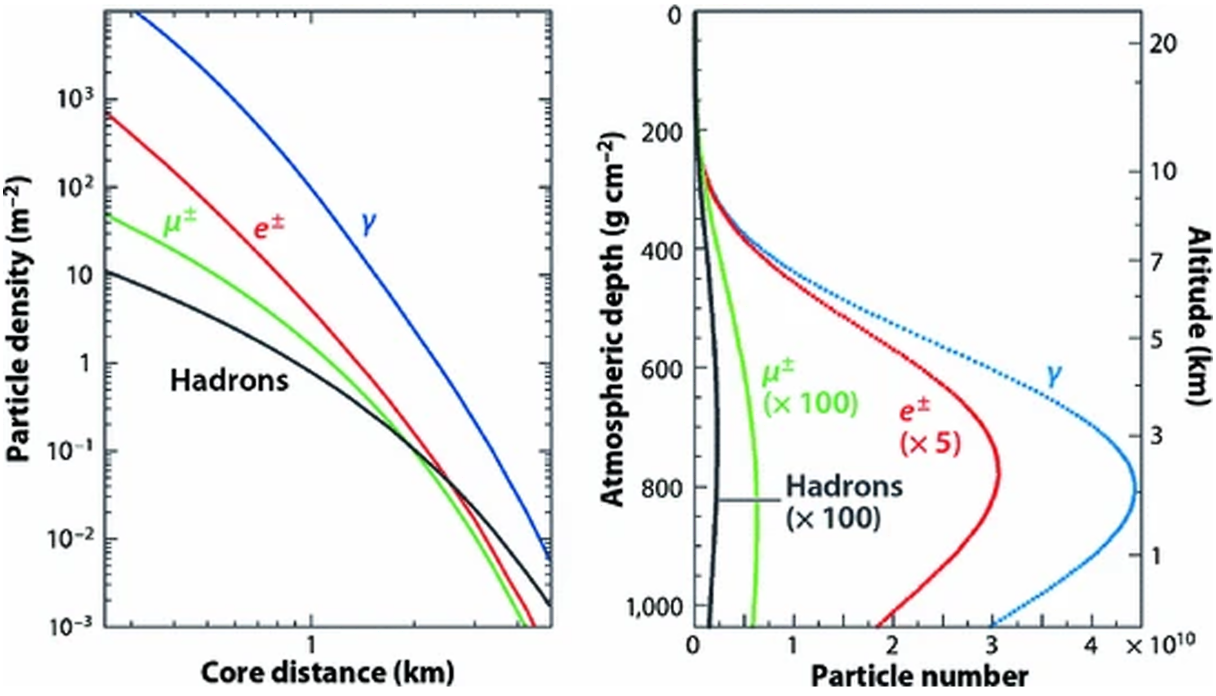

Figure 1.5.: Lateral distribution (left) and longitudinal profile (right) induced by a vertical proton with an energy of $10^{19}$ eV. Taken from [39].

## 1.6. Gamma-Hadron Separation and Detection

Section 1.5.1 and 1.5.2 highlighted the key differences in the development of gamma-ray and hadron-induced air showers. Gamma-ray air showers are predominantly dominated by the electromagnetic component, resulting in a more contained and compact footprint on the ground. In contrast, hadronic air showers exhibit more fluctuations, depending on the primary particle and energy range, resulting in a less compact footprint and larger muon content. These two main aspects will be further studied for gamma-hadron separation in Section 6.3. Specifically, the asymmetry in the air showers' footprint and the muon content of air showers.

Despite these distinct differences between gamma-ray and hadron-initiated air showers, the separation can be challenging. In particular, the two main challenges are shower-to-shower fluctuations, where protons or helium nuclei may occasionally produce a similar shower to a gamma-ray one, and identifying the muon content of the air shower. Thus, this heavily relies on the quality of the muon detector. Section 2.3 will explain how this applies to the case of the IceCube Neutrino Observatory.

CORSIKA [40] is an established software for simulations of air showers. Figure 1.6 shows the CORSIKA simulated development of a gamma-ray and proton air shower. Given a fixed energy, one of the first noticeable differences is the particles generated after the first interaction in the atmosphere. Gamma rays, on average, have a slower development since it is mainly dominated by pair production, whereas protons (and hadrons in general) produce a larger number of secondary particles right after the fist interaction, as shown in Figure 1.6. Also, this is a notable difference in the lateral spread of the shower: hadron-induced showers are less contained compared to gamma-ray-induced ones, and they exhibit larger fluctuations, particularly in particle counts at distances far from the core. Additionally, the shower composition differs significantly. Gamma-ray showers are primarily (though not exclusively) electromagnetic, consisting mostly of photons ($\gamma$) and electrons/positrons ($e^{\pm}$), as shown by the red lines in Figure 1.6a. On the other hand, hadronic showers contain a larger fraction caused by neutrinos, hadrons, and especially muons.

In conclusion, understanding both the muon content and the asymmetries at large distances from the core in air showers is crucial for accurately distinguishing between gamma-ray and hadron-induced showers.

## 1.7. Searches for astrophysical PeV gamma rays

This section presents the main methodology and results of the previous gamma-ray search by the IceCube collaboration [42]. It shows the current status of measurements

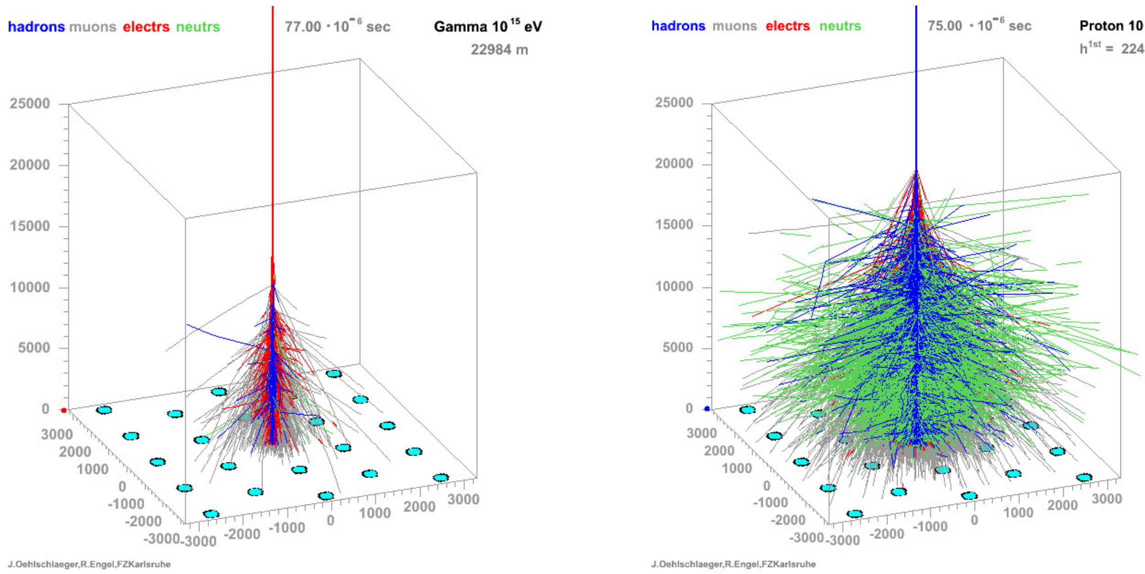

(a) 1 PeV gamma-ray air shower simulated with CORSIKA [40]

(b) 1 PeV proton air shower simulated with CORSIKA [40]

Figure 1.6.: Air shower simulations of a gamma ray (left) and a proton (right) available online [41].

of PeV gamma-rays by underlining the main results from the LHAASO experiment [5]. Finally, it shows the main intent and motivation of this thesis.

### 1.7.1. Previous works at IceCube

The IceCube Neutrino Observatory (Chapter 2) is located at the South Pole and consists of two main components: the in-ice array and the surface array (IceTop). The in-ice array detects Cherenkov light produced by relativistic charged particles. The surface array, IceTop, measures extensive air showers caused by cosmic rays. Thus, the combination of the two arrays enables the study and measurement of cosmic rays and the search for gamma rays.

The first gamma-ray search in IceCube was published in 2013 [43]. In this work, the partially completed in-ice detector with only 40 strings (IC40) and the IceTop surface array were used for the search for high-energy gamma rays. The analysis used one year of data, and no sources were found.

The search for PeV gamma rays at the IceCube Neutrino Observatory was repeated with the fully completed in-ice and surface array and published in 2019 using 5 years of data from 2011 to 2016 [42]. The search combined data from the IceTop surface array and the in-ice detector, performing the gamma-ray search in the energy range up to 100 PeV. The focus was on two primary studies: point source and diffuse emission searches.

The Point Source Search was conducted using two approaches: first, by searching for gamma rays from known TeV gamma-ray sources, and second, by performing an unbiased scan of the sky for potential unknown sources. The detected events were cross-correlated with IceCube's neutrino data to identify possible associations between gamma rays and high-energy neutrinos.

The diffuse gamma-ray emission search targeted gamma-ray emissions from the Galactic plane using a likelihood-based method to match event directions with a diffuse galactic plane emission model.

A machine learning approach was employed for the identification of gamma rays. Specifically, a random forest classifier was used to classify air showers as gamma-ray-like or cosmic-ray-like.

The classifier training was performed using five parameters: the total in-ice signal as an indicator of the high-energy muon component of the air shower, the IceTop energy proxy, the shower inclination, a containment parameter that estimates how well-contained the shower axis is in the in-ice detector array, and a log-likelihood ratio as a probability estimator.

Different classifiers were trained to explore different spectral indices for different source assumptions. For point source searches, two classifiers have been used, one with an $E^{-2}$ (hard spectrum) and another with an $E^{-2.7}$ (softer spectrum).

The key results of the analysis include a 90% confidence level upper limit on point sources, with flux values ranging from $\sim 10^{-21}$ to $10^{-20}$ $\mathrm{cm}^{-2}\mathrm{s}^{-1}\mathrm{TeV}^{-1}$ for a 2 PeV gamma-ray point source. No gamma-ray emission from known H.E.S.S. sources was observed, and no evidence of spectra extending beyond TeV energies into the PeV range was found. For seven H.E.S.S. sources, upper limits were set, excluding unbroken power-law spectra up to PeV levels.

Furthermore, no correlation was found between PeV gamma-ray candidates and high-energy neutrino events detected by IceCube. Figure 1.7 shows the diffuse emission search and the upper limit of $2.61 \times 10^{-19}$ $\mathrm{cm}^{-2}\mathrm{s}^{-1}\mathrm{TeV}^{-1}$ was determined at 2 PeV for gamma-ray flux from the Galactic plane, assuming an $\mathrm{E}^{-3}$ spectrum. A significant limitation of the analysis was the inability to achieve gamma-hadron separation of more than $10^{-2}$ in the PeV energy range, resulting in a large cosmic-ray background in the dataset used for the point-source search.

### 1.7.2. Current status

In May 2021, the LHAASO collaboration reported the first observation of multiple Ultra-High-Energy (UHE) gamma rays (above 100 TeV). In particular, identifying 12 sources and detecting a gamma-ray with an energy of 1.4 PeV from a Galactic source [44]. This discovery was made with only half of the detector array and around 300 days

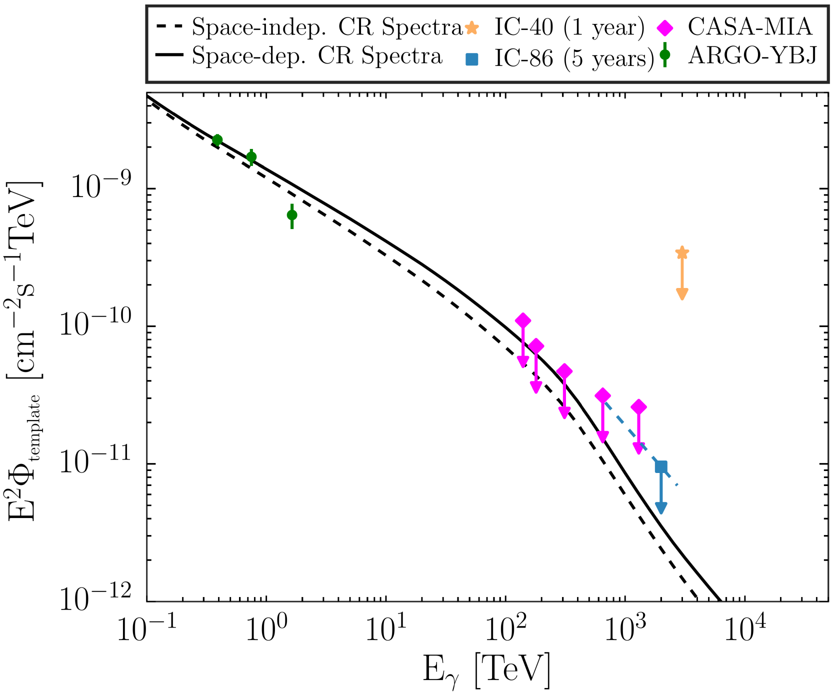

Figure 1.7.: Diffuse emission search and the upper limit of $2.61 \times 10^{-19}$ cm$^{-2}$s$^{-1}$TeV$^{-1}$ was set at 2 PeV for gamma-ray flux from the Galactic plane, assuming an $E^{-3}$ spectrum. Taken from [42].

of data collection. The LHAASO experiment can measure signals from sub-TeV up to the tens of PeV. This is achieved using the Water Cherenkov Detector Array (WCDA) for energy up to tens of TeV and the Kilometer Square Array (KM2A) for the highest energies. For the KM2A, scintillator detectors have been used mainly for measuring the electromagnetic component, and underground water tanks for the muonic component of air showers. The Crab Nebula was confirmed as one of the detected sources. Further studies of the Crab Nebula were conducted in a subsequent publication [45]. Additionally, the Cygnus region was investigated. Here, Cygnus X is one of the most active star-forming areas in the Milky Way, located around 1.4 kpc away from Earth. This region is notable for housing several massive stars and being dense in atomic and molecular gas clouds. Cygnus X was confirmed to be a pevatron for high-energy cosmic ray production and gamma-ray emissions up to PeV energies [46].

LHAASO has also published the first catalog for Ultra-High-Energy (UHE) gamma-ray sources [47]. Many of the sources have been observed with both the kilometer square array and the Water-Cherenkov detector array, showing an energy spectrum that ranges from TeV up to PeV.

In the paper on diffuse emission [48], LHAASO presented the results of the kilometer square array to detect diffuse gamma-ray emissions from the Galactic plane in the energy range from 10 TeV to 1 PeV. The analysis divided the Galactic Plane into two regions: an inner $15^\circ < l < 125^\circ, |b| < 5^\circ$ and an outer $125^\circ < l < 235^\circ, |b| < 5^\circ$, with $l$ and $b$ being the galactic longitude and latitude, respectively. It was shown that there were significant emissions from both the inner and outer regions of the Galactic plane, with $29.1\sigma$ and $12.7\sigma$ significance, respectively. The observed energy spectrum follows a power law as predicted, however, the flux was approximately 2 to 3 times higher than expected. The result is currently under investigation and further studied by extending the energy range of the analysis with the combination of data from the Water Cherenkov Detector Array.

### 1.7.3. This work

This work is encouraged by the recent results outlined in Section 1.7.2 and aims to build upon and enhance the previous search for gamma-rays with IceCube [42]. This is achieved by extending the analysis to lower energies, improving the gamma-hadron separation, and setting the basis for future searching analyses.

The analysis presented here builds on realistic gamma-ray emission scenarios, based on sources observed by the LHAASO experiment. Targeting lower energies will increase the statistics of gamma-ray events and consequently, the possibility of discoveries.

# 2. IceCube Neutrino Observatory

The IceCube Neutrino Observatory is a unique experiment primarily built to detect neutrinos from astrophysical sources. As neutrinos have a low probability of interaction with matter, a large detector volume is necessary to increase the chances of detection. The vast, transparent volume of glacial ice at the South Pole was chosen as the ideal location for such a neutrino observatory. Over millennia, accumulating layers of snow have compacted under immense pressure, forming a thick layer of ice that extends several kilometers below the surface. The clarity is remarkable down to about 2.5 km, except for a thin region known as the dust layer at the depths of 2050–2150 m [49]. This exceptional clarity allows IceCube to detect the Cherenkov radiation emitted when the secondary particles, produced via rare neutrino interactions, move faster than light in the ice. The minimal human-made noise at the South Pole further enhances detection capabilities.

In addition to neutrino detection, IceCube has a key role in studying cosmic rays. In particular, at the surface, an array of detectors called IceTop is dedicated to the detection and reconstruction of cosmic-ray air showers while also providing a veto in neutrino searches against the atmospheric background. Thus, IceCube's in-ice array and IceTop can provide valuable insights into high-energy astrophysical phenomena.

Figure 2.1 shows a complete schematic view of the IceCube Neutrino Observatory. The main characteristics of the detector are highlighted in the schematic. On the surface lies the IceTop detector with 81 stations, and the central IceCube Lab, the main building for the experiment at the South Pole. Deep in the ice, the strings of the in-ice detector are visible. The highlighted part of the strings shows the higher-density region of the detector called DeepCore. The bedrock is at a depth of about 2800 m from the surface.

The primary research focus of the IceCube Neutrino Observatory is astrophysical neutrinos and the identification and characterization of their sources. Some of the major results in this field include the detection of the first astrophysical neutrino flux [50], evidence of neutrino emission from the direction of the blazar TXS 0506+056 [50], and the observation of the diffuse neutrino flux from our Galaxy [51]. In addition, the IceCube collaboration is also actively engaged in related scientific objectives, including searching for dark matter, searching for exotic particles, studies of neutrino oscillation [52], and the search for neutrino bursts from Galactic core-collapse supernovae [53]. IceCube is

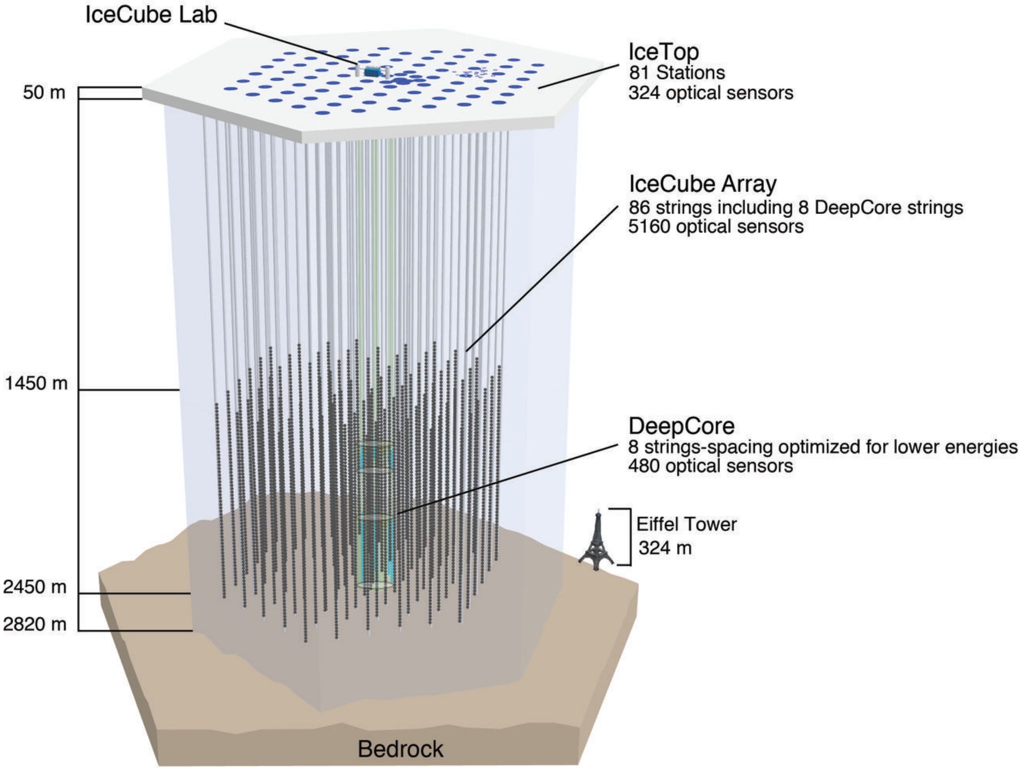

Figure 2.1.: A schematic view of IceTop and IceCube's in-ice array.

also involved in multi-messenger astrophysics through partnerships with optical, X-ray, gamma-ray, radio, and gravitational wave observatories [54].

In the cosmic-ray research area, multiple analyses produced results in the fields of the cosmic-ray energy spectrum [9] and composition [55], anisotropy [56], seasonal variation [57], and gamma-ray searches [42]; the latter being the focus of this thesis.

## 2.1. IceTop: surface air shower detector

The IceTop array covers a surface of 1 km$^2$ and is located above the in-ice detector, at a height of 2835 m above sea level, equivalent to an atmospheric depth of about 680 g/cm$^2$. As mentioned already, the two main purposes for the detector are cosmic-ray detection and veto for down-going neutrino events to distinguish them from air showers.

The design is composed of 81 stations distributed in a hexagonal shape over an area of 1 km$^2$ with a grid spacing between stations of about 125 m. This configuration allows for coverage of the energy range from TeV to EeV for air shower measurements. Each of the 81 stations comprises two ice-Cherenkov tanks, 10 m apart, with a total of 162 Cherenkov tanks. Three of the 81 stations were placed in an "in-fill array" for a denser area near the center of the detector. All tanks have been deployed below the snow level to minimize environmental interference. Figure 2.2 shows the tank distribution on the surface. Each pair of tanks has its corresponding station number shown. The stations with numbers 79, 80, and 81 compose the in-fill detector. Each IceTop tank is filled with clear ice, without any air bubbles. The internal part of the tank is highly reflective to ensure optimal Cherenkov light collection. Each tank houses two Digital Optical Modules (DOMs) operating at different gains (low and high) for extended dynamic range. Figure 2.3 presents a schematic view of a tank during its deployment. Figure 2.3a labels all external components of the tank, while Figure 2.3b illustrates and labels all internal components accordingly.

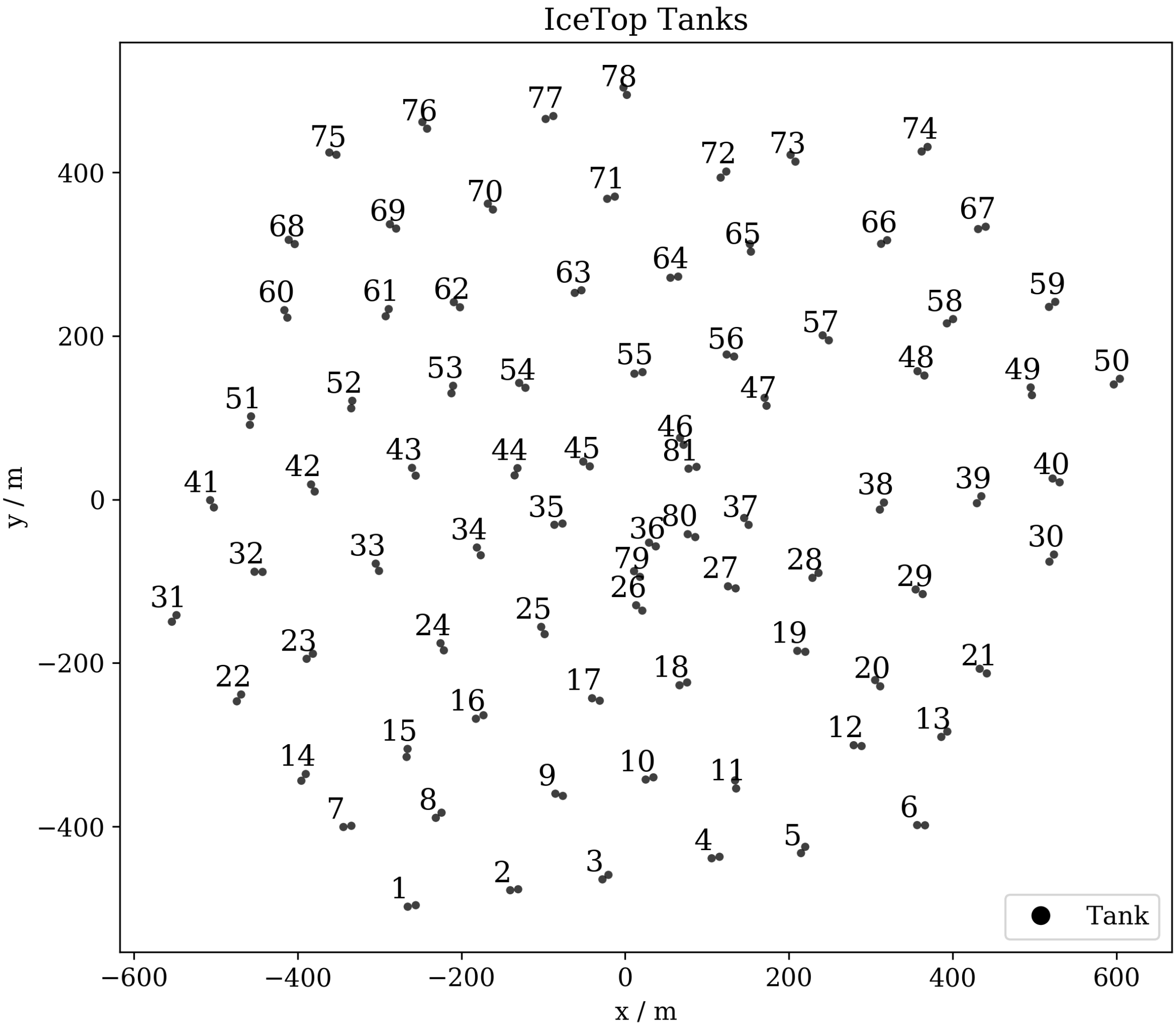

Figure 2.2.: Distribution of IceTop tanks on the surface. The stations that compose the in-fill detector correspond to the numbers 79, 80, and 81.

The IceTop array operates using a multi-level trigger, based on hardware and software. The trigger system identifies and records only significant events that satisfy specific trigger conditions. The required conditions are that the detected signals exceed the threshold

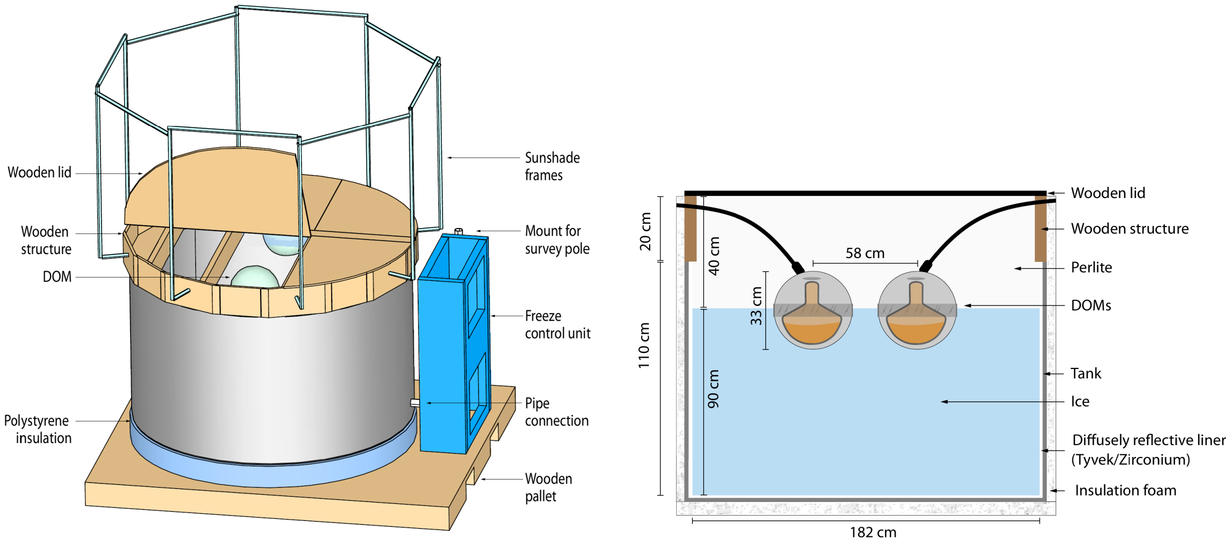

(a) Sketch of the outside view a tank.

(b) Sketch of the inside view a tank.

Figure 2.3.: A sketch of the outside and inside view of a tank. Taken from [58].

and a local coincidence is registered within a defined time window. At the detector level, only events that trigger multiple tanks are retained. There are 2 types of local coincidence hits in IceTop: HLC and SLC. Hard Local Coincidence (HLC) implies that DOMs in both tanks of a station register a hit. In particular, when the high-gain DOM in a tank registers a hit, a signal is sent to the other tank, and if any of the 2 DOMs in this tank register a hit within about 1 $\mu$s, a Hard Local Coincidence is registered and the full waveform is read out. A Soft Local Coincidence (SLC) hit occurs when only one DOM in the pair of tanks records a signal; hence can be seen as a misnomer as it does not require a coincidence. The high-gain signal is used by default, but if this gain channel saturates, the low-gain signal is utilized instead. One trigger condition often used for analysis is the "3-stations trigger", which requires 6 HLC hits in 3 stations. This trigger happens with a frequency of about 30 Hz. After the trigger, the readout starts, and each DOM will have a dead time of about 6.4 $\mu$s whenever a valid local coincidence is registered.

Once triggered, the signal measured from the Digital Optical Modules (DOMs) is digitized and sent to the central data acquisition system at the IceCube Lab. Here, it is further processed, stored, and later sent to the north for analysis. The trigger monitoring is continuous across the entire surface array, and each event timing is synchronized using a master clock at the ICL. Advanced compression algorithms are used to minimize data storage needs without losing significant information from the air shower event.

As later discussed in Section 2.4, each IceTop detector has experienced snow accumulation over the years. The increasing snow cover raised the energy threshold for detection [59]. After the completion of the IceCube array, the first full continuous year of data-taking occurred between 2012 and 2013. This period marked the best year for analysis, as the snow level was at its lowest, providing optimal conditions for gamma-hadron separation.

## 2.2. In-ice array: deep detector

The in-ice part of the IceCube Neutrino Observatory is a cubic-kilometer neutrino detector designed to detect Cherenkov radiation from the secondary charged particles produced by the high-energy neutrinos interacting in the Antarctic ice. It is composed of 5160 DOMs, distributed across 86 vertical strings, between 1450 m and 2450 m below the surface of the ice. Each string is made of 60 DOMs attached along a single cable that provides power and transmits the recorded signals. Figure 2.4 shows a schematic view of an in-ice DOM. The PMTs in the DOMs collect Cherenkov light produced by charged particles traveling through the ice. For this reason, the clarity of the ice is an important factor in the accuracy of the measurement. However, the clarity of the ice is not constant throughout the entire depth, requiring calibration and modulation of the ice.

Figure 2.4.: A schematic view of an in-ice DOM.

Similar to the IceTop array, the in-ice detector is also enhanced with a denser region of strings known as ’DeepCore’, to extend its sensitivity to lower-energy neutrinos. The regular in-ice array covers a volume of one cubic kilometer with 78 strings. In each string, the DOMs are 17 m apart from each other. From a top view, the detector has a hexagonal shape with strings deployed on a grid with 125 m horizontal spacing. This design allows for the detection of astrophysical neutrinos for the TeV to PeV energy range.

DeepCore, however, consists of a subset of in-ice DOMs deployed deeper than 1750 meters, with a more densely instrumented volume and correspondingly lower energy threshold. It consists of an additional seven strings with an average spacing of about 72 meters. In this region, the spacing between DOMs is comparatively closer, that is, roughly 7 meters apart. Each string is equipped with 50 DOMs. This denser configuration lowers the energy threshold to around 10 GeV, which is about an order of magnitude lower than the standard threshold for most IceCube analyses. The data obtained from DeepCore is used, among others, for the measurement of atmospheric neutrino oscillations, search for neutrinos from WIMP dark matter annihilation, Galactic supernovae, and to identify astrophysical sources of sub-TeV neutrinos.

Overall, the in-ice detector has been detecting mainly air shower muons and secondary particles that come from neutrino interactions with the ice. The small interaction cross-section of neutrinos and the extremely low fluxes require a large volume to make the probability large enough to have reliable statistics.

The interaction of a neutrino with matter produces a lepton. The PMTs of the IceCube detector can detect its emitted Cherenkov light. Figure 2.5 shows Feynman diagrams of a neutrino interaction with matter.

The type of interaction depends on their flavor. One type of interaction caused by electrons is called cascade events. Typically, these events are well contained in the detector, meaning that all of the energy of the interaction is deposited in the detector. As a result, these events have good energy resolution but poor directional resolution. Figure 2.6a shows an example of a cascade event. A second type of interaction is produced by a muon neutrino, which generates a muon that can travel a long distance before being absorbed. As a result, these events are only partially contained in the detector. However, these events have good directional resolution, as the direction of the muon can be measured accurately. Figure 2.6b shows an example of a track event. A third type of interaction is given by the tau neutrino, which can generate a unique event called "double bang". The tau lepton decays quickly, and if it decays inside the detector, the event topology that is formed can be a combination of a short cascade and a track or two cascades.

## 2.3. IceCube and Gamma-Hadron Separation

The in-ice and surface detectors of IceCube can be combined for gamma-hadron discrimination, owing to the possible detection of muons from hadronic interactions with the in-ice detector.

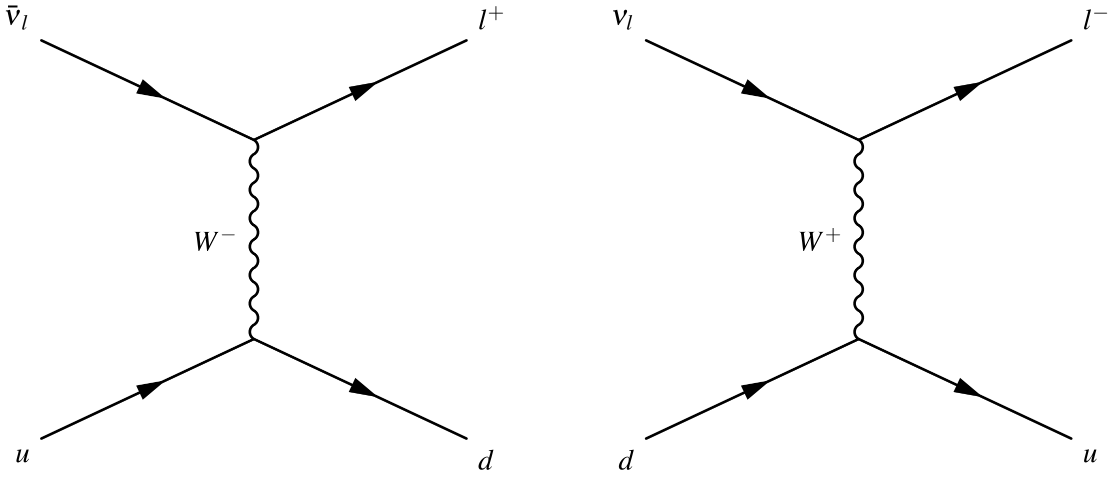

(a) $W^-$ neutrino interaction.

(b) $W^+$ neutrino interaction.

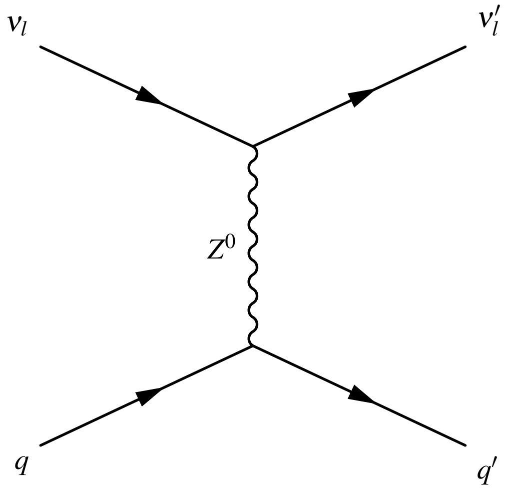

(c) $Z^0$ neutrino interaction.

Figure 2.5.: Feynman diagrams of a charged-current neutrino interaction.

Not all muons are capable of reaching the in-ice detector. Only muons with energies above 273 GeV can travel to the in-ice detector and leave a track that can be detected. In addition, from the simulations, it is clear that air showers produced by different primaries have different development. Consequently, the muon content from these showers is very different, making the classification based on the measurements.

Thus, some showers do not produce any in-ice signal even if the shower axis intersects the deep detector. In particular, at PeV energies, almost all hadronic showers feature high-energy muons, but only a few gamma-ray showers. Figure 2.7 shows two simulated events with corresponding surface and in-ice signals. The color indicates the timing of the pulses following the rainbow colors: from an early hit in red to a late event in blue.

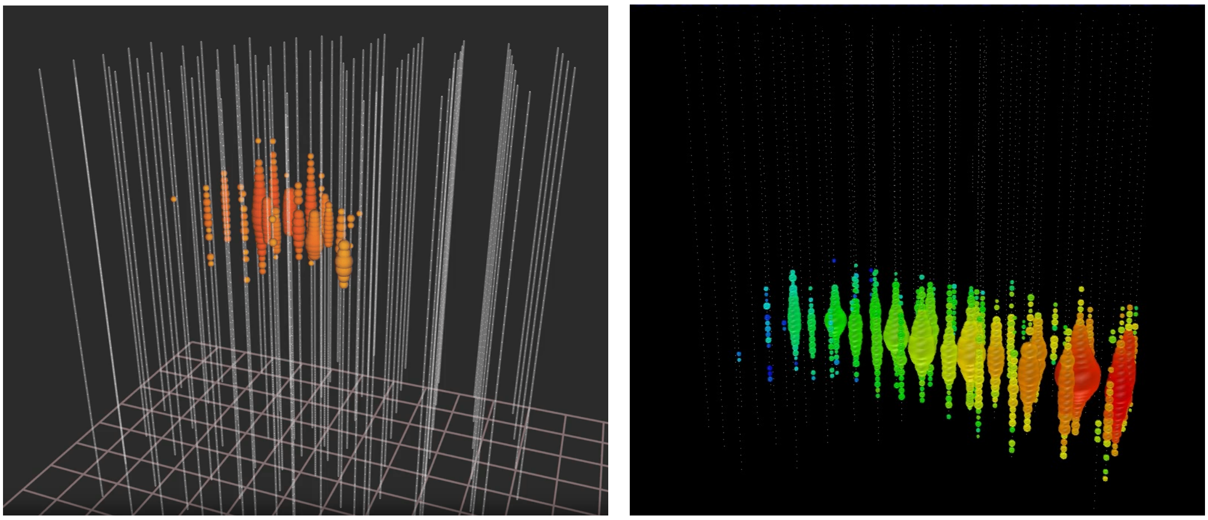
(a) Cascade event. (b) Track event.

Figure 2.6.: A cascade and track event in IceCube's in-ice array. The color indicates the time, from early (red) to late (blue).

The size corresponds to the deposited energy in the PMTs. The main difference is the in-ice signal with the gamma-ray event (Figure 2.7a) showing no track in the in-ice detector in contrast to the proton event (Figure 2.7b) showing a clear in-ice track. For events without and in-ice track, it is important to utilize quantities that can be measured using the surface detector. It is, however, not possible to reliably distinguish between electromagnetic and muonic components of the air shower using the surface detector. This is a challenge when it comes to the identification of a shower. It is possible, though, to separate hadronic and electromagnetic showers via the different types of hits. As discussed in Section 2.1, there are 2 types of hits, HLC and SLC hits. Usually, HLCs are generated by the electromagnetic component that is similar for all showers, even if generated by a different primary. SLCs are usually generated by muons at a larger distance from the shower axis. Thus, this information can be exploited for gamma-hadron discrimination studies.

In summary, the IceCube experiment can be used for gamma-hadron discrimination. In particular, the combined information from IceTop and the in-ice detectors can be instrumental in this endeavor. The in-ice array can give information about the high-energy muon component of air showers, and the surface array can be used for both the detection of the showers and eventually the SLC hits can be used for obtaining an additional background suppression factor.

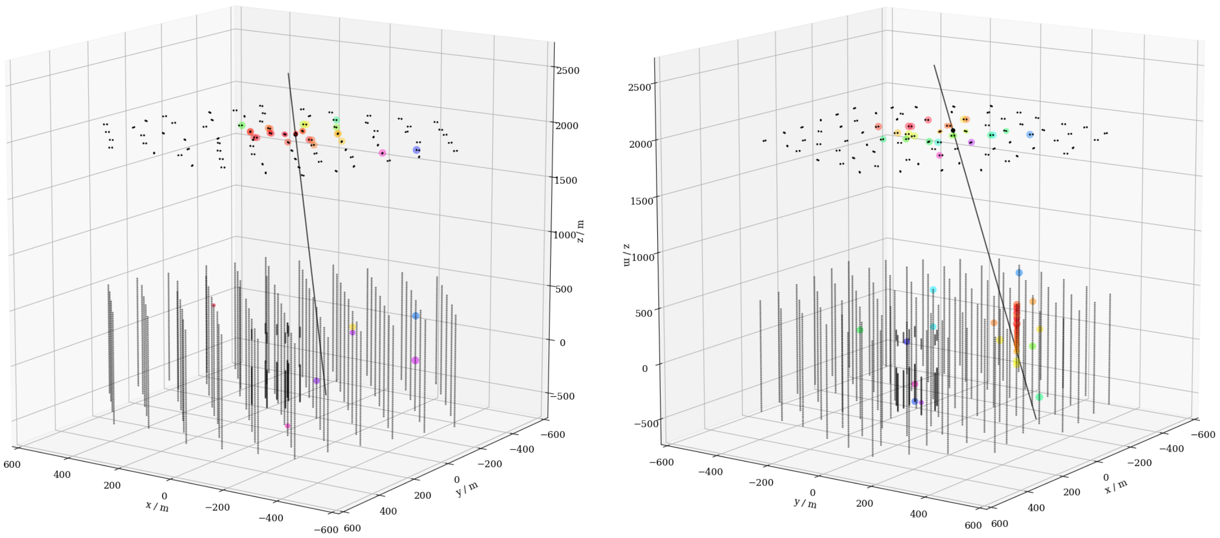

(a) Simulated gamma-ray event with energy with about 1 PeV.

(b) Simulated proton event with energy with about 1 PeV.

Figure 2.7.: Two simulated events with corresponding surface and in-ice signals. The color indicates the timing of the pulses following the rainbow colors: from an early event in red to a late event in blue. The size corresponds to the deposited energy in the PMT. The main difference is the in-ice signal: the gamma-ray event shows no track in the in-ice detector, but only a few accidental DOMs of noise, in contrast to the proton, which shows a clear in-ice track.

## 2.4. The Future of IceCube

The IceCube detector has been fully operational since 2011, continuously collecting data using the surface and in-ice detector arrays. Through its results, IceCube has shown multiple times the benefits of continuing the research at the South Pole. An upgrade and a second-generation detector called IceCube-Gen2 are necessary to increase the number of detected neutrino events and the science case.

### 2.4.1. IceCube Upgrade and Surface Enhancement

The first planned upgrade, called the IceCube Upgrade [60], involves the deployment of seven new strings into the ice in the 2025/26 polar season. These new strings will have a denser arrangement of the optical modules and introduce new calibration devices to the IceCube array. This addition will improve neutrino detection capabilities at low energies. Furthermore, they will facilitate the study of the muonic component of air showers and improve the calibration of the entire detector. This will be achieved in particular by further studying the ice properties at the South Pole. It will also act as a test bed for the next-generation array IceCube-Gen2. Figure 2.8 shows the position of the panned IceCube upgrade and the location of the strings aiming at having a denser region of PMTs in the ice.

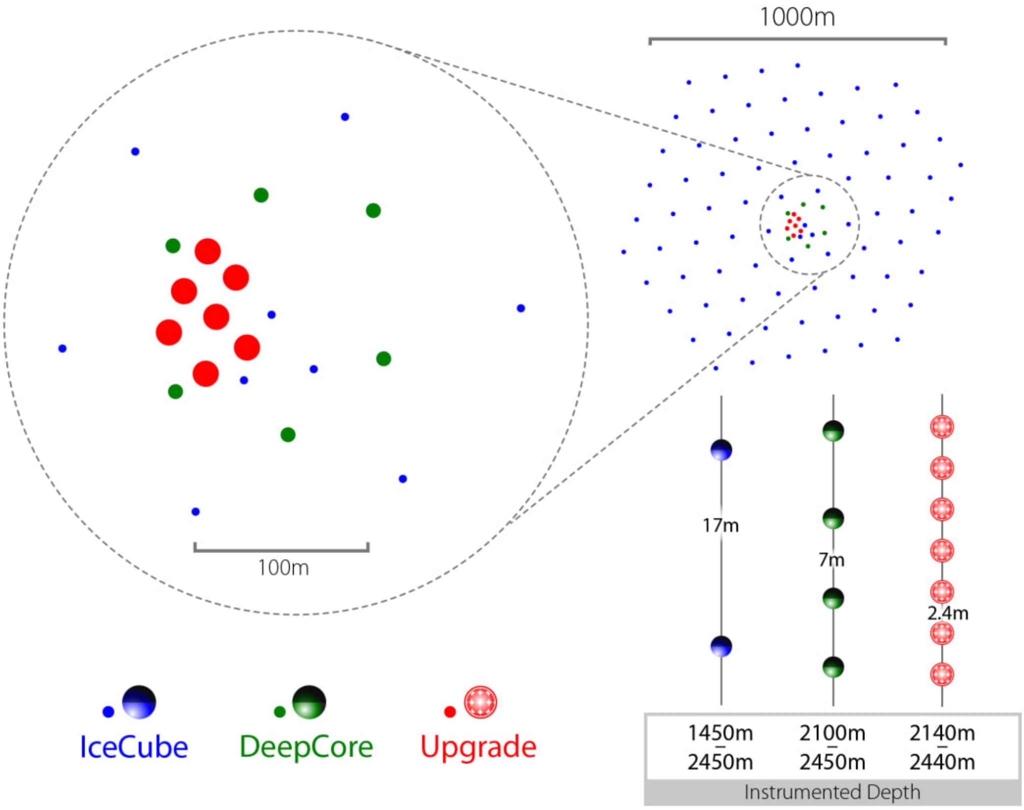

Figure 2.8.: Schematic view of the IceCube Upgrade [60].

Additionally, an enhancement of IceTop called the surface array enhancement [60] is planned. This will involve deploying a set of stations comprising elevated scintillation detectors and radio antennas along the IceTop surface area. This multi-detector surface upgrade aims to reduce the increasing threshold in energy generated by the snow on the IceTop tanks that attenuates the low-energy signals.

The surface enhancement will allow for an extended energy range, from $10^{14}$ eV up to $10^{18}$ eV, improving cosmic-ray measurements through the combined use of the three detector channels: the scintillator panels, radio antennas, and the existing IceTop tanks. This integration will enable comprehensive studies of air shower physics by analyzing the different components of air showers. The planned upgrade includes 32 stations. Figure 2.9 shows a scheme of the positions of all planned detectors, with a focus on the layout of a single station. A key advantage of the new detectors is that they can easily be raised from the surface, preventing snow buildup and simplifying maintenance, including the replacement of any malfunctioning hardware.

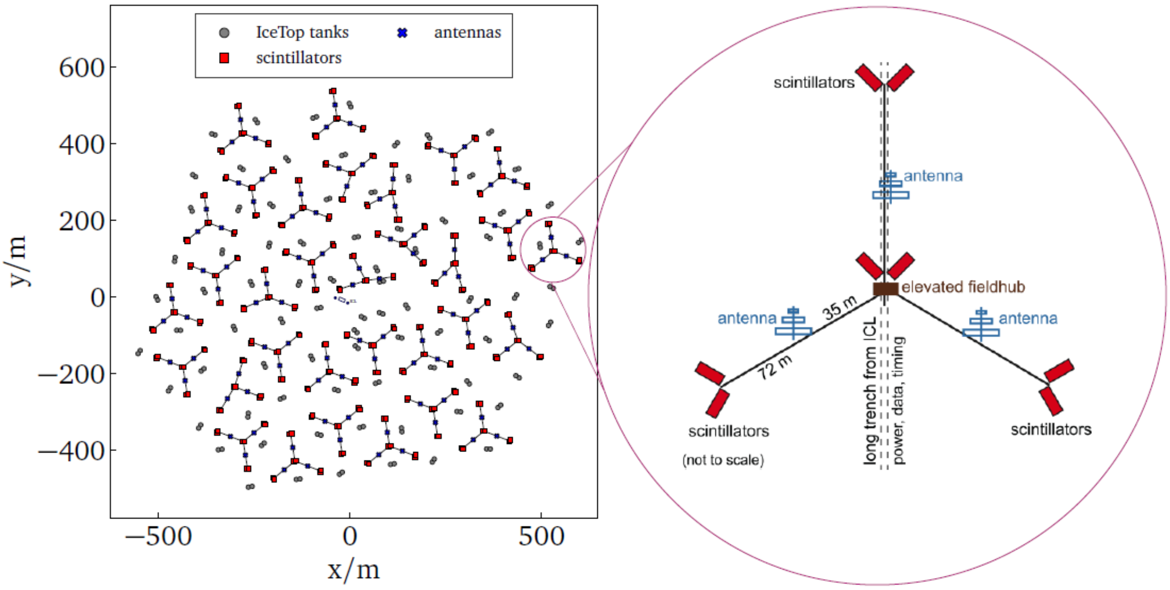

Figure 2.9.: Schematic view of the IceTop enhancement. Tanken from [61]

A prototype station of the surface enhancement was deployed in January 2020. This prototype station included three antennas and four pairs of scintillators. Figure 2.10 shows a photo taken at the South Pole of an antenna and a scintillator panel. The prototype station has been taking air shower data continuously since 2020, with a first upgrade in January of 2023 [62] involving improvements in detector hardware. In January 2025, two further stations were deployed.

### 2.4.2. IceCube-Gen2

The next generation enhancement of IceCube will be IceCube-Gen2 [64, 65], which will be built upon the current design featuring both an in-ice and a surface array. The in-ice optical array will cover a volume of approximately 8 km$^3$, with the optical modules arranged in an optimized sunflower geometry. The optical modules for Gen2 will have an improved design, with multiple PMTs in each module drawing on the experience from the IceCube Upgrade modules. This layout minimizes the gaps between the in-ice strings, enhancing muon measurements and consequently neutrino detection. The strings will be spaced about 240 m, an increased distance of about a factor of two compared to the current spacing of 125 m. Despite the larger spacing, the sensitivity to neutrinos will cover the energy range, from TeV to EeV, and the increased volume will improve the statistical sample by roughly an order of magnitude compared to the current array.

The surface array of IceCube-Gen2 will extend over an area of approximately 6 km$^2$, overlaying the in-ice array with scintillation and radio detectors. As with the current

Figure 2.10.: Photos taken at the South Pole of an antenna and a scintillator panel [63].

IceCube setup, the surface array will act as a veto for atmospheric muons originating from the southern sky. This configuration will significantly expand the aperture for the surface-deep coincident air shower measurement by a factor of about 30 compared to the current setup. The antennas will measure the electromagnetic component of air showers via the radio emission produced by the electromagnetic shower component, while the scintillators will simultaneously detect both the electromagnetic and muonic components. Furthermore, the expanded in-ice detector will facilitate the detection of high-energy muons associated with air showers. Together, these complementary detection systems will enable detailed studies of cosmic ray properties, including the mass composition of cosmic rays and gamma-hadron discrimination, providing valuable insights into high-energy astrophysical processes. Figure 2.11 shows the field of view of the current IceTop and IceCube combined and the field of view of IceCube-Gen2.

An additional component of IceCube-Gen2 will be an in-ice radio array. This array will detect radio emissions produced by secondary particles generated in neutrino interactions and detect neutrinos with energies larger than 10 PeV. This component will follow its precursor, the Radio Neutrino Observatory in Greenland (RNO-G), currently under construction. [66].

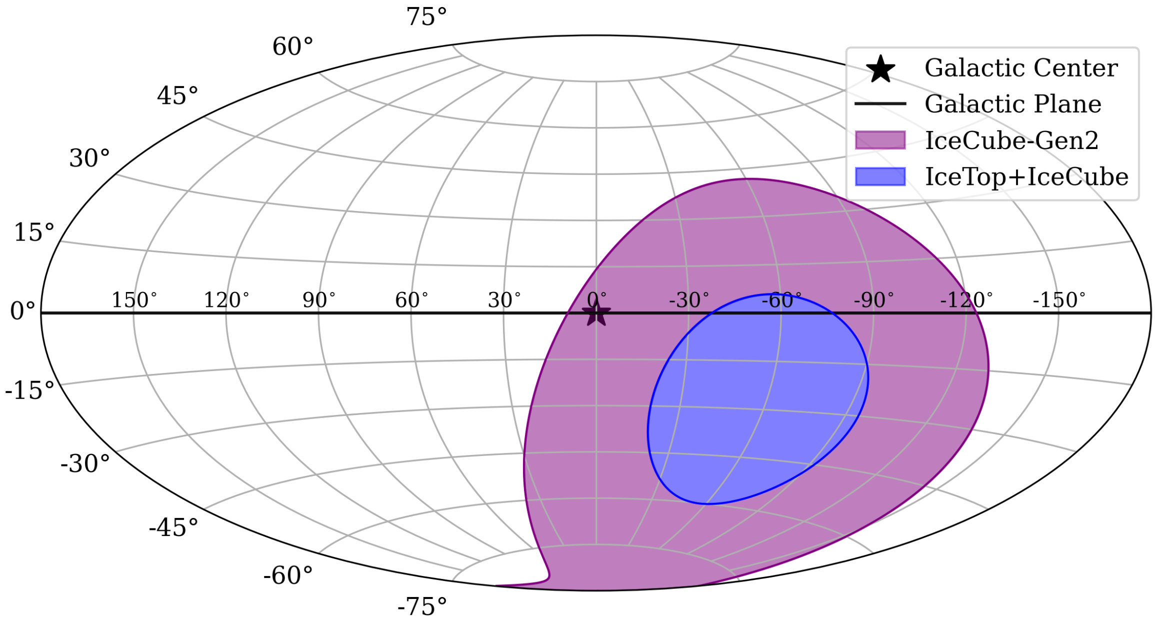

Figure 2.11.: Field of view of IceCube and IceCube-Gen2.

Figure 2.12 presents a schematic view of IceCube-Gen2. Here, the current design and the newly planned in-ice array are illustrated. The key components of the IceCube-Gen2 are highlighted in the circular insets. Notably, insets showcase the new in-ice DOM with multiple PMTs, the surface array station with antennas and scintillator panels, and the radio array designed for in-ice radio detection of neutrinos.

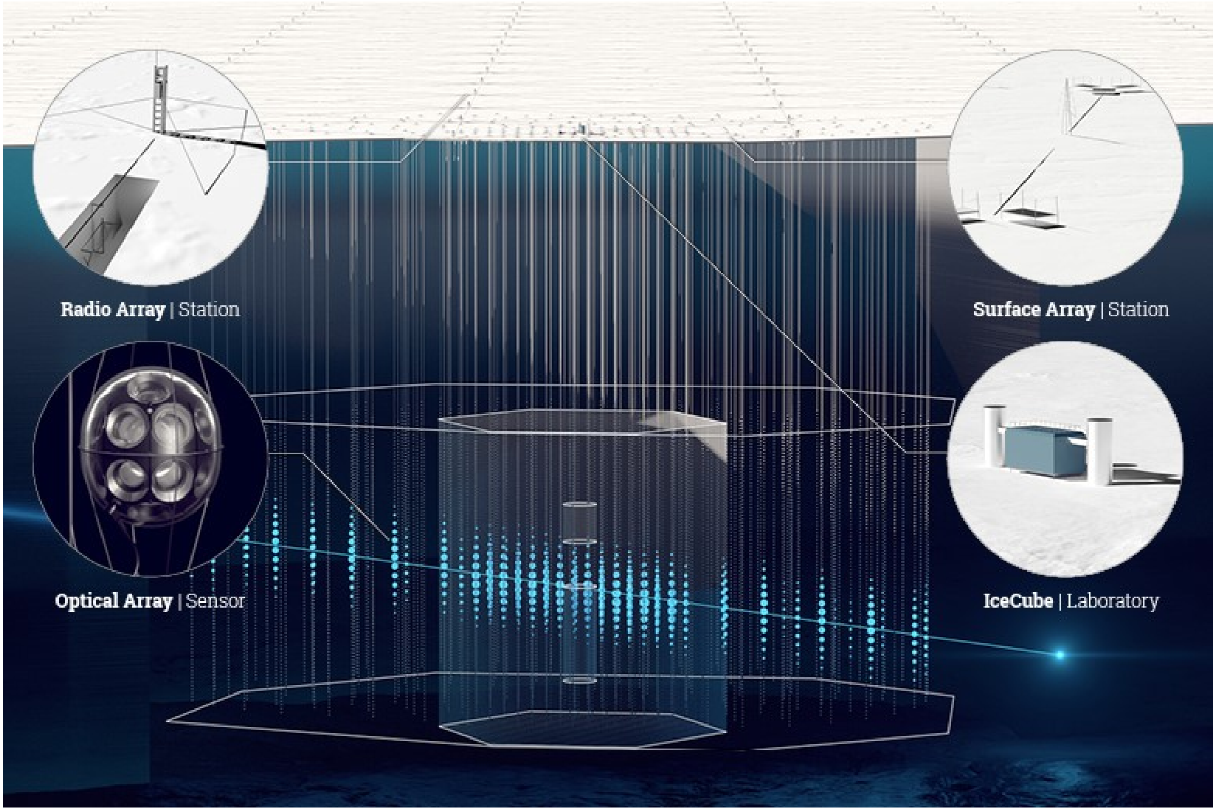

Figure 2.12.: Schematic view of IceCube-Gen2. Taken from [67].

# 3. Data Sets

This chapter presents the Monte Carlo simulations of cosmic-ray air showers used for this thesis. It outlines the main steps in generating the simulations, focusing on the air-shower simulation and the detector response. Finally, it compares the weighted simulation with the measured 2012 IceCube data to assess the reliability of the simulations.

## 3.1. Monte-Carlo Simulations

The complete simulation is performed in a two-step process. The first part is the simulation of the cosmic-ray air showers using CORSIKA (COsmic Ray SImulations for KAscade) [40], a widely used software for Monte Carlo simulations of the development of air showers from the initial cosmic-ray interaction in the atmosphere down to ground level. The second step is the detector response simulation. This is performed using GEANT4 [68], an established software for particle interaction and detector response. The particle output from the CORSIKA simulation is used as input for GEANT4 to model the interactions of the particles with the detector, specifically the IceTop surface array and the in-ice detector.

The following sections outline the main steps for the air shower simulation and the detector response.

### 3.1.1. Air-shower Simulation

CORSIKA (COsmic Ray SImulations for KAscade) is the primary software used to simulate air showers from cosmic rays and photons. It simulates the interactions between the primary particle and atmospheric nuclei, predicting the number, energy, and secondary particles, such as - electrons, muons, photons, and hadrons, which reach the surface, where the IceTop tanks are situated. It is a highly customizable simulation framework that allows the user to select different hadronic and low-energy interaction models. Beginning with the primary cosmic rays interacting in the atmosphere, the simulation tracks all secondary particles. For each secondary particle, it records its position, energy, direction, type, and arrival time at a predefined observation level relative to the first interaction. Due to the statistical nature of interactions, each shower is different, and only physical quantities of ensembles can be compared. This requires a large number of showers to be simulated. Thus, multiple showers are simulated with similar settings to compare the distributions, since it cannot be done on individual showers.

The simulations used for this thesis use the SIBYLL [69] model for hadronic interactions and FLUKA [70] for low-energy interactions (E < 80 GeV). For this analysis, two sets of simulations are used: an established set of simulations performed with SIBYLL 2.1 [71], previously utilized in cosmic-rays studies [9], while the second set is newly produced using the updated SIBYLL 2.3d [69]. The primary cosmic-ray particles simulated with the updated SIBYLL 2.3d version are gamma rays and protons. They will serve as the main primaries used for the subsequent analysis of the thesis.

### 3.1.2. Detector response

The detector response is applied in two main steps. Starting with the CORSIKA output as input for GEANT4, the first step models the IceTop detector response, and the second simulates the in-ice array. The surface detector response uses all particles that reach the surface as input, while the in-ice response uses only the particles, specifically muons, that propagate through the ice and generate a signal in the detector. Figure 3.1 presents a schematic diagram illustrating the complete simulation process.

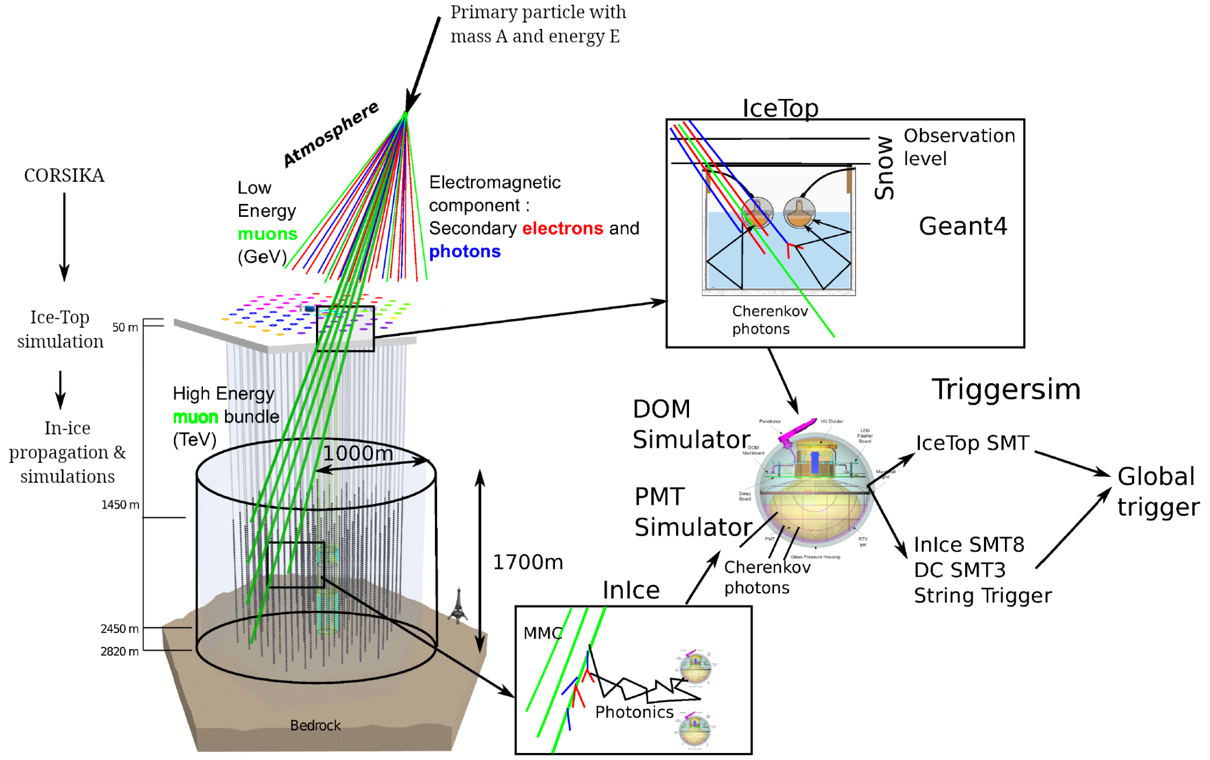

Figure 3.1.: Schematics of the simulations. Modified from [72]

Once the air-shower development is simulated, the particles that reach the ground level, along with all their relevant properties, are recorded. These are used as input for the simulation of the detector response. As previously mentioned, it is performed using GEANT4 [68], a widely used toolkit for simulating particle interactions with matter. It models the emission of Cherenkov light that the DOMs convert into electrical signals, as particles pass through the ice Cherenkov tanks. The detector simulation process has to account for real-world factors such as snow accumulation on top of tanks or air layers in them. The accuracy of modeling these effects is essential for reliable and precise simulations. The snow accumulation affects the Cherenkov light production in the tank and consequently the intensity of the signal. Furthermore, the snow level differs for each tank and changes over time. Hence, simulations are usually performed every 3 years with different snow levels. This is particularly important when analyzing data spanning multiple years.

The in-ice detector response is simulated by taking into account muons with energies above 273 GeV, as this is the minimum energy required for a muon to reach the in-ice detector and produce a detectable signal. To save computational time, lower-energy muons are not propagated, since they lack sufficient energy to traverse the ice. The more energetic muons are propagated through the ice to the detector, where the Cherenkov light they produce is simulated, followed by the response of the PMTs, which convert the light into electrical signals. Then, measured in-ice noise is added, and the surface and in-ice simulations are merged to represent a single event.

The final step in the simulation is performed, which is known as the Vertical Equivalent Muon (VEM) calibration. The "VEM" is a standard unit of charge for IceTop. It is defined as the charge deposited by a single minimum ionizing vertical muon passing through an IceTop tank. With VEM calibration, it is ensured that the simulated amount of light produced by particles in the tanks corresponds to what is observed for actual muon events. It is consistently applied to both measured and simulated data to enable meaningful comparisons.

To optimize computational efficiency, a technique called ‘resampling’ is used. In this method, each air shower is used multiple times in the detector response simulation by randomly redistributing its core position within a circular area of radius $R$ centered at the IceTop array. As simulating a single shower requires significant computational time, resampling allows the same shower to generate different detector responses depending on its impact position. This approach improves statistics while maximizing efficiency.

Once the full simulation chain is completed, an offline filtering process is applied [9]. During the three standard levels of further processing, the simulated data is processed exactly like real experimental data, ensuring consistency in subsequent analyses. During the filtering, trigger conditions are applied, and pulse cleaning, noise removal, and reconstruction are performed, mimicking the processing of measured IceCube data.

### 3.1.3. Simulation Production

The simulations were performed on the Horeka cluster at KIT [73], generating a large number of events to account for statistical fluctuations. Specifically, the energy of the primary particle was binned in $\log_{10}(\text{Energy}/\text{GeV})$ from 4.0 to 7.9, with a bin width of 0.1 on a logarithmic scale. In each bin, the energies are randomly selected by the CORSIKA software. Simulations were conducted, assuming an isotropic azimuthal distribution and a zenith angle binning, under the assumption of isotropic flux for a flat detector. The number of simulated CORSIKA air showers varied with energy to optimize statistical precision, with a larger number of air showers simulated for low energy. Specifically, for each bin of 0.1 in $\log_{10}(\text{Energy}/\text{GeV})$: 3,000 showers are simulated from 4.0 to 4.4, 2,500 from 4.5 to 4.9, 2,000 from 5.0 to 5.4, 1,500 from 5.5 to 5.9, and finally 1,000 showers for all bins above 6.0. This approach ensured sufficient statistics at lower energies, where detection rates are smaller.

To further improve statistical accuracy, each air shower was resampled 100 times in the detector response simulation. This resampling process uses the same air showers but shifts their positions randomly across the detector array, assuming an isotropic surface distribution, effectively enhancing event statistics without computational cost for additional CORSIKA simulations. The methods for reconstruction and their results will be discussed in Section 4.5. Table 3.1 summarizes the entire simulation process.

## 3.2. Measured Data

The dataset represents the measurements recorded from the IceCube 2012 run, which started at the end of April 2012 and ended at the beginning of May 2013. However, for this cross-check of the simulations, only a subset of data, known as the 'burnsample' has been used. It corresponds to approximately 10% of the total amount of data in this run. This has been done with the agreement of the IceCube cosmic-ray working group. Due to time limitations, the Sibyll 2.3d simulations for the year 2012 were performed only for the proton set and not for the three remaining mass groups required for the comparison. Hence, the Sibyll 2.1 [71] simulation set was used for the data and MC simulation comparison. This set was already used in a previous analysis [9]. The simulations are weighted using IceCube's `simweights` tool [74] following a weighting with the H4A model of cosmic-ray flux and composition [75]. This method assigns weights to four primary cosmic-ray mass groups: proton (H), helium (He), oxygen (O), and iron (Fe) nuclei, based on their expected flux at Earth.

The comparison between real data and MC simulations is referred to as data-MC agreement. This process is necessary for assessing simulation uncertainties and evaluating how well the simulations replicate actual data. One of the main challenges in the sim-

Table 3.1.: Summary of simulation setup and parameters. These settings were used for each primary particle simulated to ensure equal sets of simulations.

| **Simulation Environment** | |
|---|---|
| **Parameter** | **Details** |
| Computational Resource | Horeka Cluster [73] |
| CORSIKA version | 77420 |
| Hadronic model (E < 80 MeV) | FLUKA |
| Hadronic model (E > 80 MeV) | SIBYLL 2.3d |
| Energy Range | $\log_{10}(\mathrm{Energy}/\mathrm{GeV}) \in [4.0, 7.9]$ |
| Binning in energy | 0.1 in $\log_{10}(\mathrm{Energy}/\mathrm{GeV})$ |
| Zenith Angle Distribution | Isotropic flux assumption |
| Azimuthal Distribution | Isotropic |
| **Air Shower Simulations** | |
| **Energy Interval** $[\log_{10}(\mathrm{Energy}/\mathrm{GeV})]$ | **Number of Simulated Air Showers** |
| $[4.0, 4.4]$ | 3,000 |
| $[4.5, 4.9]$ | 2,500 |
| $[5.0, 5.4]$ | 2,000 |
| $[5.5, 5.9]$ | 1,500 |
| $[6.0, 7.9]$ | 1,000 |
| **Detector Response and Resampling** | |
| **Parameter** | **Details** |
| Resampling Factor | 100 for all energy bins |
| Detector Array | Flat detector with isotropic flux |
| **Energy Interval** $[\log_{10}(\mathrm{Energy}/\mathrm{GeV})]$ | **Radius of resampling / m** |
| $[4.0, 4.9]$ | 400 |
| $[5.0, 5.9]$ | 800 |
| $[6.0, 6.9]$ | 1,100 |
| $[7.0, 7.9]$ | 1,700 |

ulation process is modeling the hadronic interactions. The comparison of the data to simulations checks for a statistical agreement between the data and the Monte Carlo simulation, proving the latter's reliability.

The following plots illustrate the relevant quantities used in this validation analysis. Some of these plots will introduce concepts that will be explained in greater detail in subsequent chapters. The measured data and Sibyll 2.1 MC simulations have been reconstructed using Laputop3s3s (Section 4.3.2), and the comparison was done after the quality cuts (Section 4.4) have been applied. The agreement of the following quantities is expected to be a qualitative agreement and not a perfect match, especially in the sub-PeV energy range.

Figure 3.2 presents the comparison between data and Monte-Carlo simulations on the energy proxy $S_{125}$ (Section 4.5.3). The top panel shows the weighted comparison between data and MC simulations, with the y-axis representing the event rate of the reconstructed events after quality cuts and the x-axis accounting for $\log_{10}(S_{125}/\mathrm{VEM})$. The black dots correspond to the data, while the red dashed line represents the MC simulations. The bottom panel shows the relative difference between MC and data. Overall, this is a qualitative agreement with the only difference being an underestimation of measured data by a constant factor throughout the entire energy range.

The top panel also shows Sibyll 2.1 and Sibyll 2.3d proton simulations with blue and green lines, respectively. Both simulation sets are plotted using the H4A weighting. This allows the comparison of the two simulation sets and shows their importance in the total flux. The two reveal that the newer Sibyll 2.3d simulations yield higher values than the older Sibyll 2.1 set, especially where the discrepancies between the weighted MC simulation and data are larger. This likely indicates that Sibyll 2.3d provides a better description of the data. Hence, the discrepancies may decrease once the full set of Sibyll 2.3d simulations becomes available.

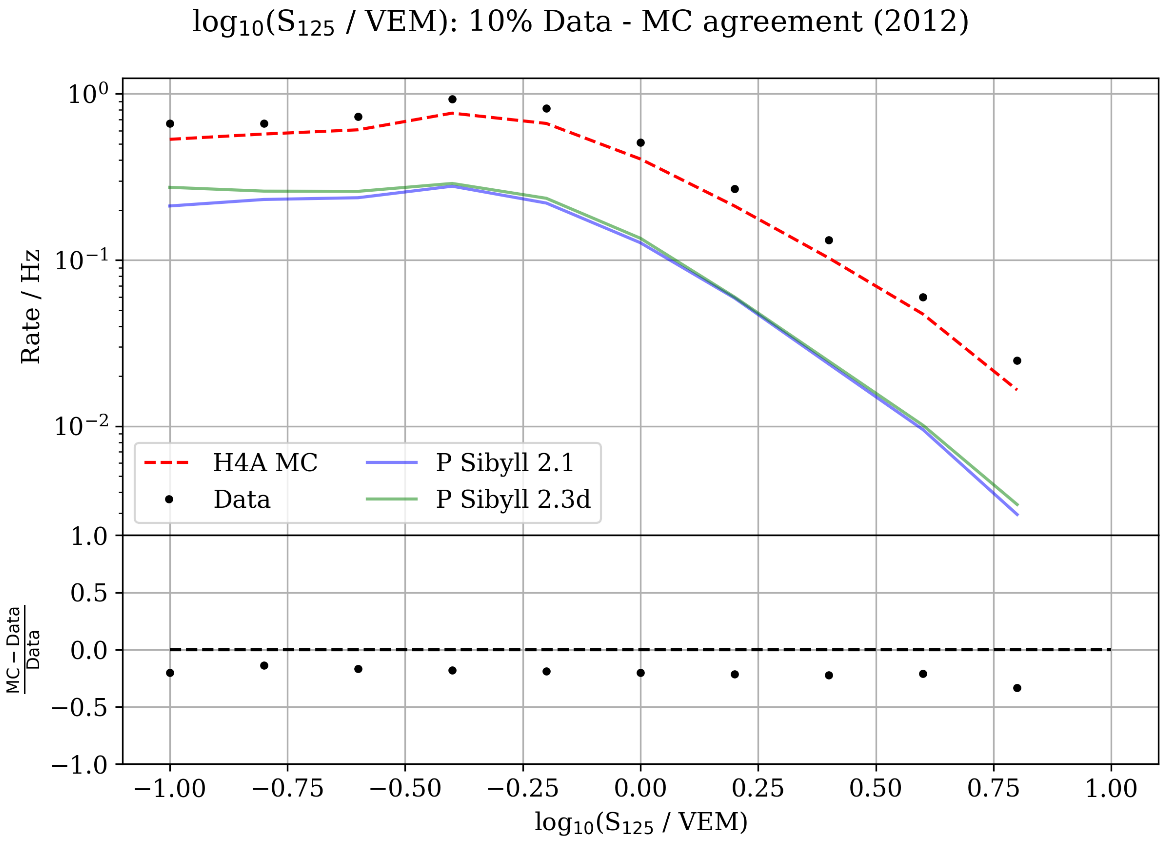

Figure 3.2.: The top plots show the comparison between experimental data and Sibyll 2.1 Monte-Carlo simulations weighted by the H4A flux model as a function of the energy proxy $\log_{10}(S_{125}/\mathrm{VEM})$. The y-axis shows the rate of the reconstructed events after quality cuts. The black dots represent the data; the red dashed line represents the MC simulations. The bottom panel shows the relative difference between MC and data. The top panel also shows Sibyll 2.1 and Sibyll 2.3d proton simulations with blue and green lines, respectively; both simulation sets are plotted using the H4A weighting.

Figure 3.3 shows the slope of the lateral distribution function $\beta$, which will be discussed in Section 4.3.1. The four panels correspond to different energy ranges, expressed via the energy proxy $S_{125}$. The data-MC agreement is worse for low energies, as shown in the top-right plot. This discrepancy is expected due to reduced reconstruction accuracy in this energy range. It will be further discussed in Section 4.5.1. Overall, the residuals indicate an underestimation of the rate for events with $\beta < 3.0$ and a better agreement between measured data and weighted MC simulations for values above $\beta > 3.0$. Each panel consists of two subplots: The top plots show the comparison between data and weighted MC simulations, with the y-axis representing the event rate of the reconstructed events after quality cuts and the x-axis showing $\log_{10}(S_{125}/\mathrm{VEM})$. The black dots represent the data; the red dashed line represents the MC simulations. The bottom panel shows the relative difference between MC and data. The main challenge remains the low energy range, where the statistics are lower and the beta values are smaller than at higher energies. For this reason, the overall agreement tends to improve for higher $\beta$ values where the detection efficiency is higher and, consequently, the event statistics, as discussed later in Section 4.2.

As previously discussed, the comparison of Sibyll 2.1 and Sibyll 2.3d proton simulations (blue and green lines, respectively), weighted with the H4A model, shows that the newer Sibyll 2.3d simulations yield higher values than the older Sibyll 2.1 set, especially where the discrepancies between the weighted MC simulation and data are larger.

Figure 3.4 presents the comparison of the Charge-Distance quantity, which will be discussed in detail in Section 6.2.2. The four panels show different energy ranges expressed using the energy proxy $S_{125}$. The data and MC simulation agree for smaller values of the Charge-Distance. However, a mismatch is noted for larger values. This is probably caused by the lower statistics in simulations compared to the data. Despite this, the larger residuals are at larger values of the Charge-Distance, which will not be so relevant for the analysis as discussed in Section 6.2.2. In each panel, the top plots show the comparison between data and weighted MC simulations, with the y-axis representing the event rate and the x-axis the energy proxy $\log_{10}(S_{125}/\mathrm{VEM})$. The black dots represent the data; the red dashed line represents the MC simulations. The bottom panel shows the relative difference between MC and data.

Once again, the comparison of Sibyll 2.1 and Sibyll 2.3d proton simulations (blue and green lines, respectively), weighted with the H4A model, shows that the newer Sibyll 2.3d simulations yield higher values than the older Sibyll 2.1 set, especially where the discrepancies between the weighted MC simulation and data are larger.

Figure 3.5 shows the sum of the in-ice charge, a quantity used for the gamma-hadron discrimination, which will be discussed in Section 6.2.1. The four panels account for different energy ranges expressed using the energy proxy $S_{125}$. However, large in-ice charge values are not reproduced in simulations. Consequently, this caused lower statis-

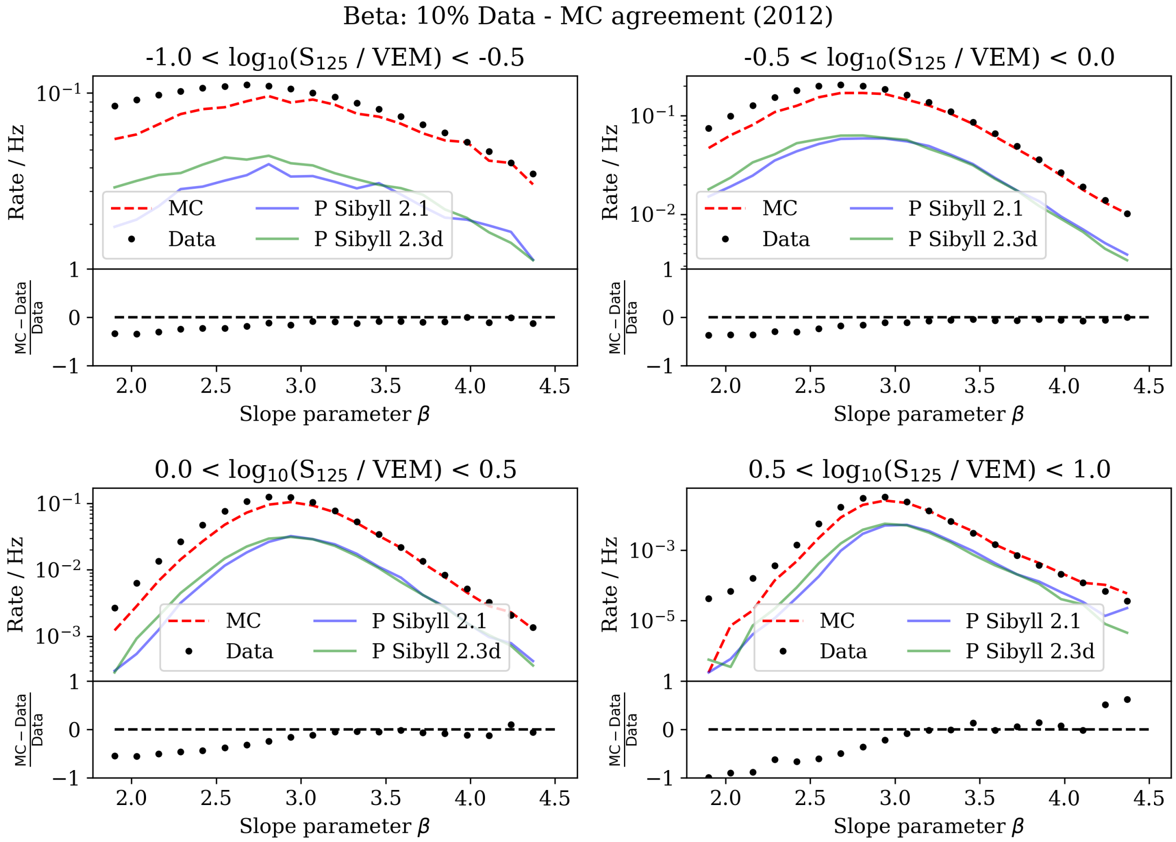

Figure 3.3.: Comparison of data and Sibyll 2.1 Monte-Carlo simulations weighted by the H4A flux model for the slope of the lateral distribution function $\beta$ (discussed in Section 4.3.1). The four panels show different energy ranges expressed via the energy proxy $S_{125}$. In each panel, the top plots show the comparison between the data and the weighted Monte-Carlo simulations. The y-axis shows the rate of the reconstructed events after quality cuts. The black dots represent the data; the red dashed line represents the MC simulations. The bottom panel shows the relative difference between MC and data. The top panel also shows Sibyll 2.1 and Sibyll 2.3d proton simulations with blue and green lines, respectively; both simulation sets are plotted using the H4A weighting.

tics in simulations compared to the data. This is relevant, especially at low energies, where the statistic is lower. Also, the sub-unit in-ice charge values are mainly due to noise, thus, the residuals show a not-perfect agreement between the measured data and the MC simulation. In each panel, the top plots show the comparison between data and weighted Monte-Carlo simulations, with the y-axis representing the event rate and the x-axis showing $\log_{10}(S_{125}/\mathrm{VEM})$. The black dots represent the data, and the red dashed line is the MC simulations. The bottom panel shows the relative difference between MC and data.

Finally, the comparison of Sibyll 2.1 and Sibyll 2.3d proton simulations (blue and green lines, respectively), weighted with the H4A model, shows that the newer Sibyll 2.3d

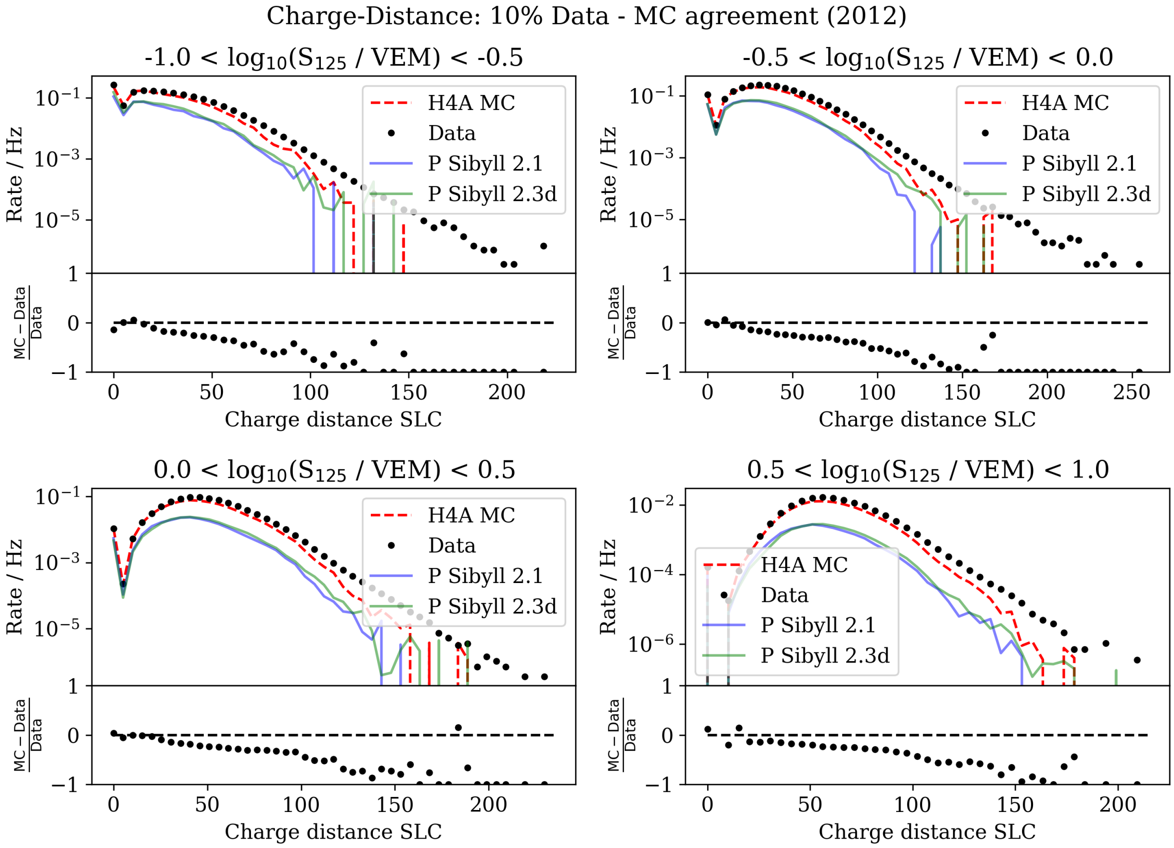

Figure 3.4.: Comparison of IceTop data and Sibyll 2.1 Monte-Carlo simulations weighted by the H4A flux model for the Charge-Distance (discussed in Section 6.2.2). The four panels show different energy ranges expressed via the energy proxy $S_{125}$. In each panel, the top plots show the comparison between the data and the weighted Monte-Carlo simulations. The y-axis shows the rate of the reconstructed events after quality cuts. The black dots represent the data; the red dashed line represents the MC simulations. The bottom panel shows the relative difference between MC and data. The top panel also shows Sibyll 2.1 and Sibyll 2.3d proton simulations with blue and green lines, respectively; both simulation sets are plotted using the H4A weighting.

simulations yield higher values than the older Sibyll 2.1 set, especially where the discrepancies between the weighted MC simulation and data are larger.

In conclusion, the energy proxy, the slope parameter, the Charge-Distance, and the in-ice charge demonstrate a qualitative agreement between the measured data and the simulations. However, discrepancies remain between the data and the Sibyll 2.1 MC simulations weighted with H4A. Generally, the low-energy simulations underestimate the measured data rate, while the agreement improves at higher energies. The low-energy discrepancy could primarily be attributed to lower statistics, where fewer events may experience larger fluctuations after weighting. This issue may be resolved once the Sibyll 2.3d simulation dataset is completed. It will include about 50% more CORSIKA

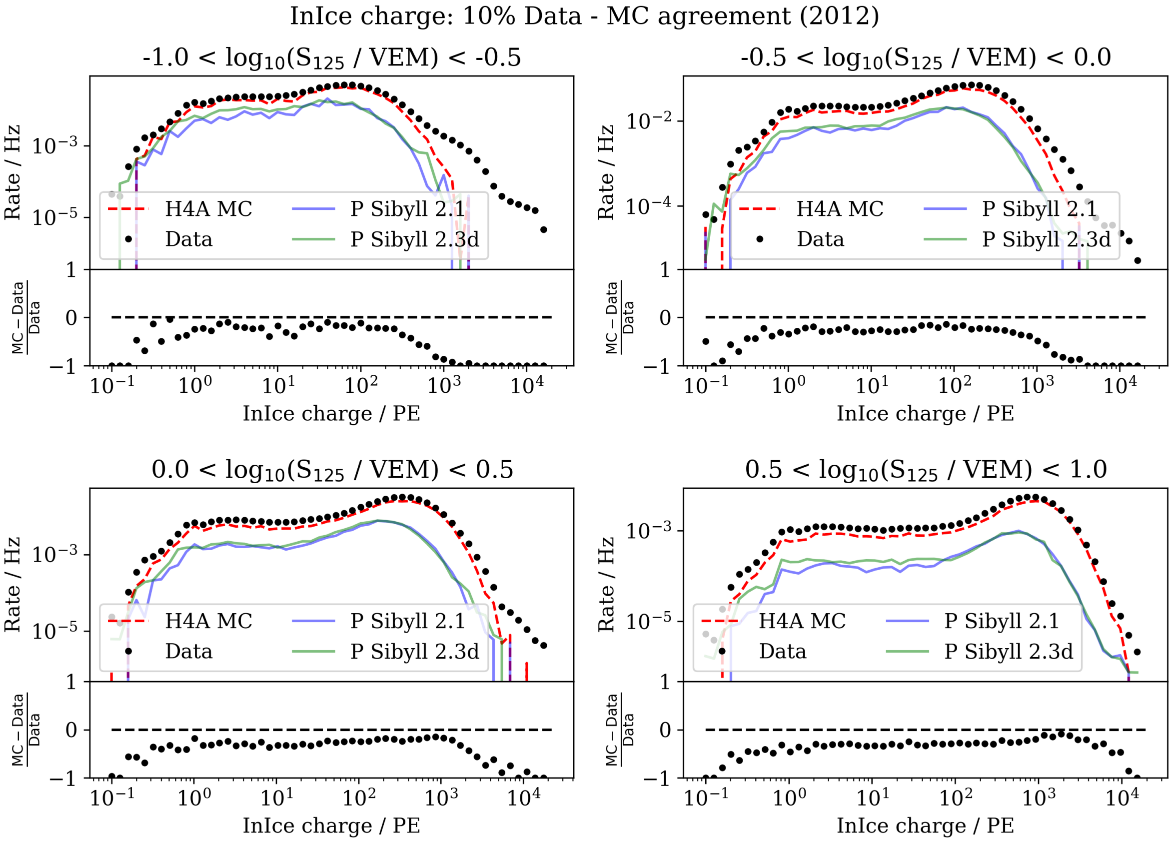

Figure 3.5.: Comparison of data and Sibyll 2.1 Monte-Carlo simulations weighted by the H4A flux model for the sum of the in-ice charge (discussed in Section 6.2.1). The four panels show different energy ranges expressed via the energy proxy $S_{125}$. In each panel, the top plots show the comparison between the data and the weighted Monte-Carlo simulations. The y-axis shows the rate of the reconstructed events after quality cuts. The black dots represent the data; the red dashed line represents the MC simulations. The bottom panel shows the relative difference between MC and data. The top panel also shows Sibyll 2.1 and Sibyll 2.3d proton simulations with blue and green lines, respectively; both simulation sets are plotted using the H4A weighting.

simulations, compared to Sibyll 2.1, thereby enhancing the statistical accuracy of the plots. Furthermore, the comparison of Sibyll 2.1 and Sibyll 2.3d proton simulations, weighted with the H4A model, has shown that the newer Sibyll 2.3d simulations yield higher values than the older Sibyll 2.1 set, especially where the discrepancies between the weighted MC simulation and data are larger. This likely indicates that Sibyll 2.3d provides a better description of the data. Hence, the discrepancies may decrease once the full set of Sibyll 2.3d simulations becomes available.

However, for this analysis, achieving a perfect match between the measured data and the charged nuclei simulations is not crucial, since the focus is on the gamma-hadron separation, rather than composition studies. Consequently, gamma-ray simulations are of greater interest. Furthermore, a subset of the 2012 dataset is used for setting the final selection criteria. This simplifies the analysis by not requiring weighting or composition models. This is discussed in more detail in Chapter 6.

# 4. Event detection and reconstruction

This chapter focuses on the detection and reconstruction of events within the IceTop array. The energy dependence of the trigger and reconstruction efficiencies are discussed, followed by an introduction to a new reconstruction method for low energies that is compared to the established one. Additionally, the selection criteria (quality cuts) for the new reconstruction method are defined, and validation plots are presented.

## 4.1. Event detection with IceTop

The most relevant trigger condition in IceTop for this analysis is the "3-station trigger". For this trigger to activate, at least 6 Hard Local Coincidence (HLC) DOMs must be hit within a 6 µs time window, i.e., 3 pairs of IceTop tanks, hence "3-station trigger". DOMs are classified as HLC if both tanks in a station are triggered within a 1 µs window. Another trigger condition used for the air-shower detection is the "5-station trigger". It requires 10 HLC DOMs hit to be activated, i.e. 5 pairs of IceTop detectors.

## 4.2. The 3-station trigger efficiency

Not all air showers satisfy the criteria for the trigger condition, particularly in the sub-PeV energy range. Understanding the fraction of events that can generate a trigger is crucial for studying the behavior of the IceTop array. For this purpose, gamma-ray and proton simulations are used to estimate the trigger efficiency. Section 3.1 provides more details on the simulation methodology. Events are selected by applying two primary cuts: a maximum distance from the center of $r < 500$ m to the center of IceTop and a zenith angle $\theta < 38°$.

Given an energy range from $E_0$ to $E_1$, the trigger efficiency $\eta$ is defined as the ratio of simulated events that pass the final filtering stage (called Level 3) and within that radius and zenith angle range to the total number of simulated events at the initial simulation stage within the same radius and zenith angle range:

$$\eta[\mathrm{E}_0 < \mathrm{E} < \mathrm{E}_1] = \frac{\text{Number of Level 3 events}}{\text{Number of simulated events}} \tag{4.1}$$

The simulations that do not generate any trigger are not saved during the filtering process. The reason is simply due to the limited storage capacity. However, it is possible to estimate the fraction of events that generate a 3-station trigger (at least 3 stations record an HLC hit) by comparing the number of simulations in the first simulation step and the number of simulations at the last level of filtering. Figure 4.1 shows this ratio (trigger efficiency) as a function of energy. The energy dependence of the trigger efficiency is observed to decrease rapidly in the sub-PeV energy range. Furthermore, the efficiency differs for the two primary particle types. Gamma-ray air showers trigger more frequently than proton-generated showers at the same sub-PeV energy. This is because HLC DOMs are hit mostly due to the electromagnetic component of the air showers. Gamma-ray air showers are predominantly electromagnetic, while hadronic showers involve muons, which carry away part of the total energy. Consequently, the electromagnetic component of proton showers is smaller, thus, the HLC DOMs require a higher-energy hadron shower to achieve the same electromagnetic energy deposit as a gamma-ray shower.

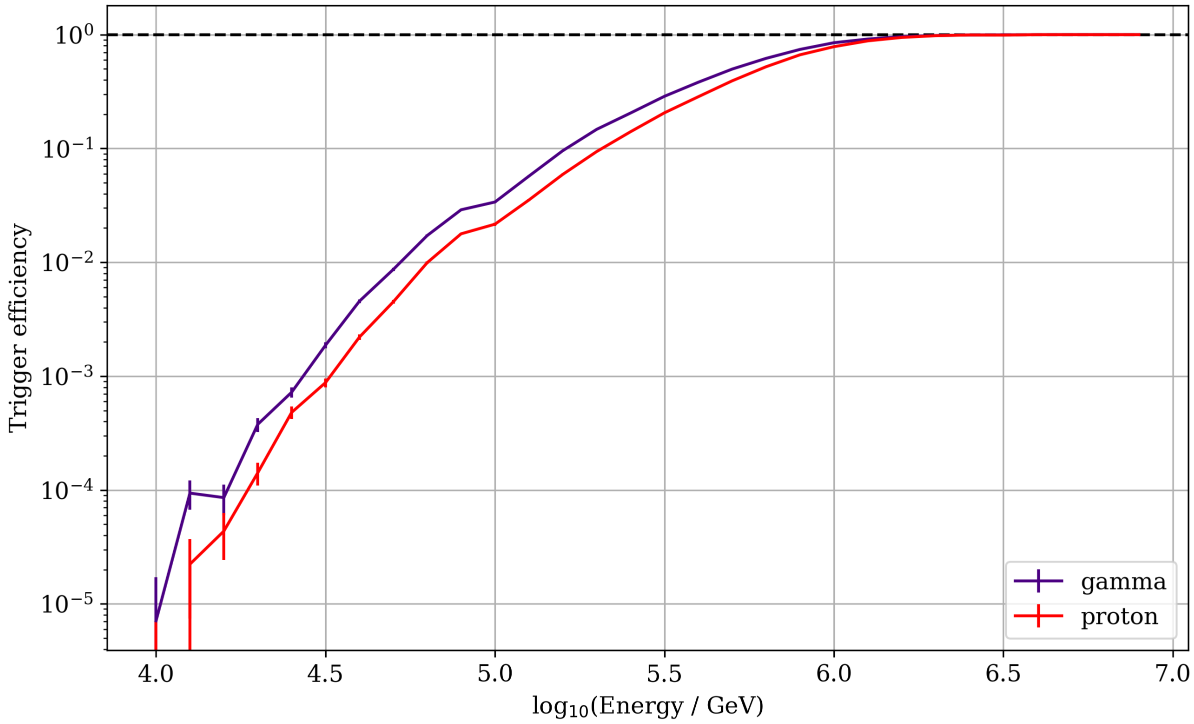

Figure 4.1.: Trigger efficiency $\eta$ as a function of energy. The energy binning is 0.1 on a logarithmic scale.

## 4.3. Reconstruction Methods for IceTop events

All IceCube events that meet at least one of the trigger conditions are recorded, including IceTop hits. For this analysis, the trigger condition required is the 3-station trigger. After triggering, the recording starts, and the events follow a filter stage after which they can be reconstructed. The standard reconstruction method used for air-shower reconstruction is called "Laputop". This reconstruction method requires the 5-station trigger, which makes it less suited for gamma-ray studies at low energies. As explained earlier, the 5-station trigger results in the loss of too many events, necessitating a reconstruction method that works with the 3-station trigger to preserve more events. Such a reconstruction method named "Laputop3s3s" was developed explicitly for the scope of this analysis.

In the following sections, the two methods are analyzed and compared.

### 4.3.1. Laputop

The primary reconstruction method used for IceTop data is called Laputop. This method finds the best fit for following showers parameters: core position, direction ($\theta$, $\phi$), slope ($\beta$) of the lateral distribution function (LDF), and the energy proxy ($\mathrm{S}_{125}$), which represents the signal strength at a reference distance to the shower axis of 125 m. The minimization process uses two main functions: the signal-strength lateral distribution function (LDF) and the time-distribution function. The LDF estimates the core position, the lateral-distribution slope $\beta$, and the signal strength at 125 m from the shower axis $\mathrm{S}_{125}$. The function that describes the LDF is a double logarithmic parabola:

$$S(r) = \mathrm{S}_{125} \cdot \left(\frac{r}{125\mathrm{m}}\right)^{-\beta-\kappa\cdot\log_{10}(r/125\mathrm{m})}, \tag{4.2}$$

where $r$ is the distance from the shower axis and $\kappa$ is a constant with a value of 0.303, representing the curvature of the parabola.

Figure 4.2 shows the signal strength as a function of the distance from the shower axis of a high-energy measured event with reconstructed energy $\mathrm{E} > 10$ PeV. The color of the circles shows the time of the pulses following the rainbow coloring: early in red, late in blue. The solid line shows the LDF Laputop fit to the data, with the one sigma uncertainty band shown with the gray band. Finally, the x-marker shows the signal strength at the reference position 125 m.

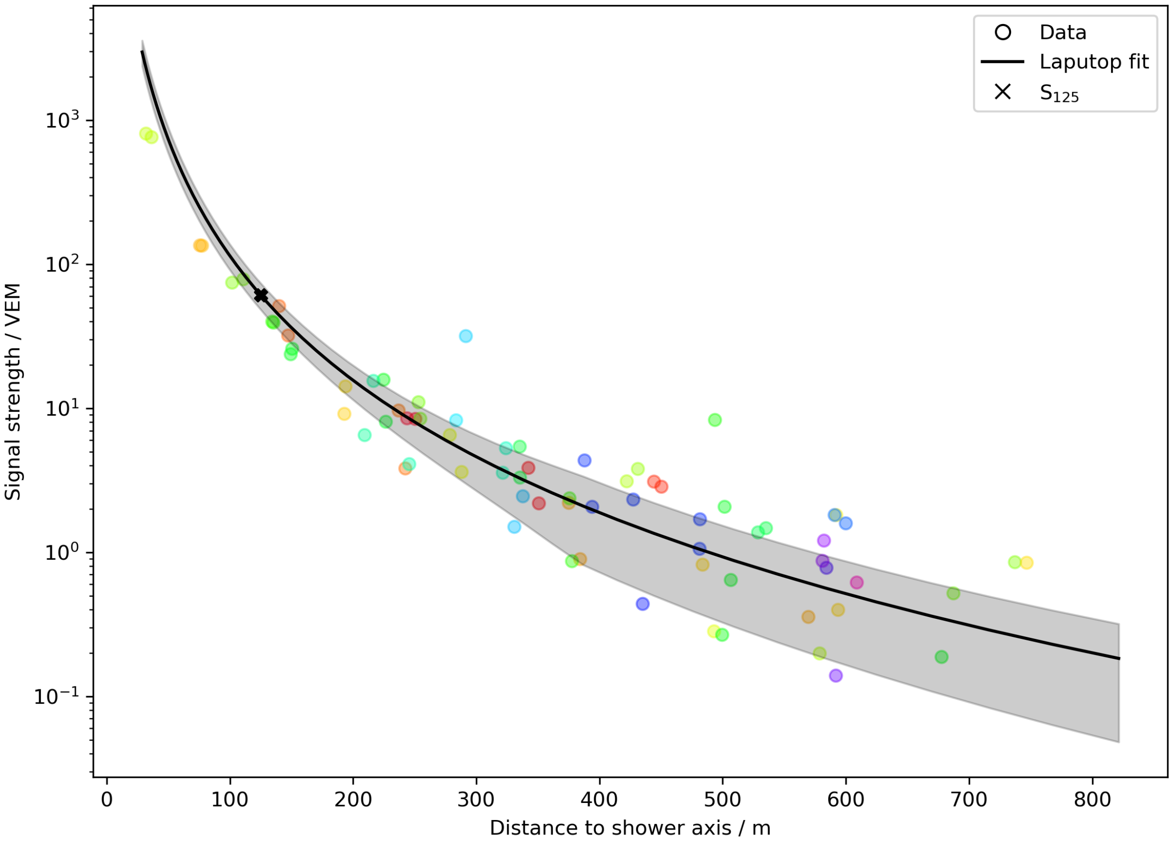

Figure 4.2.: Signal strength as a function of the distance from the shower axis of a high-energy measured event with reconstructed energy E > 10 PeV. The color of circles shows the time of the pulses following the rainbow coloring: early in red, late in blue.

The directional reconstruction is based on the time of the hits in the DOMs. The corresponding time distribution function is a parabola with a Gaussian "nose":

$$\frac{t(r)}{\text{ns}} = N\left(\exp\left(\frac{-r^2}{D^2}\right) - 1\right) - Ar^2, \tag{4.3}$$

where the first term defines the "Gaussian nose" and the second term is the parabola. This timing likelihood is typically used to fit the track direction ($\theta$ and $\phi$) and core time ($t_{\text{core}}$), used as free parameters in the minimization, since the shower direction is most strongly related to the timing of the hits [63].

Figure 4.3 shows the pulse time relative to the shower plane as a function of the distance from the shower axis of the same high-energy event of Figure 4.2. The color of the circles again shows the time relative to the shower plane of the pulses following the rainbow coloring. The solid line shows the time distribution fit to the data done via Laputop, with the one sigma uncertainty band shown with the gray band. It is worth noticing that the early pulses (red and orange circles) and the late pulses (purple and blue circles) are further away from the shower axis. This is an expected behavior because of the development of the air shower.

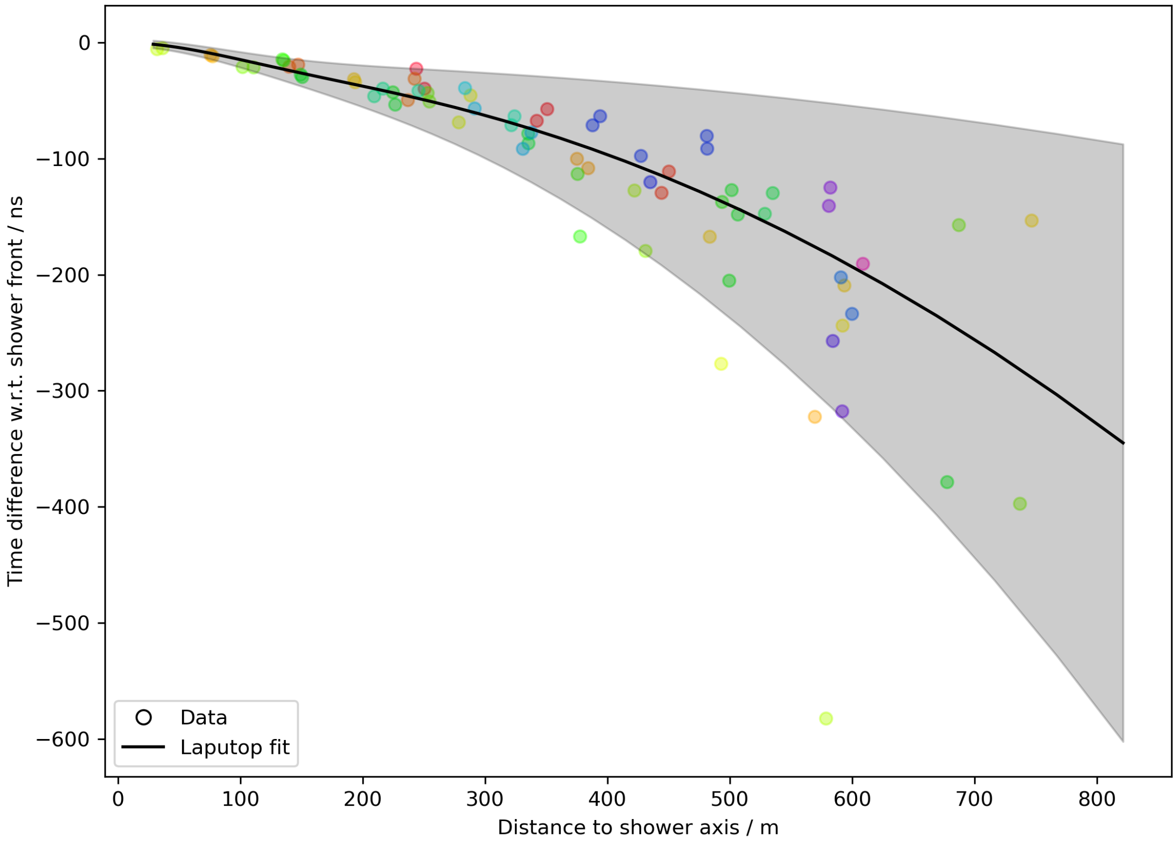

Figure 4.3.: Pulse time as a function of the distance from the shower axis of the same high-energy event of Figure 4.2. The color of the circles again shows the time of the pulses following the rainbow coloring.

As already discussed in Section 2.4, one of the major problems for the IceTop detector is the accumulation of snow. The snow accumulation on top of the tanks decreases the strength of the electromagnetic signal. To overcome this problem, the previous IceTop analysis [9] corrected the LDF fit via a constant factor that assumed a uniform distribution of the snow. In this analysis, the snow attenuation is corrected with a newer tool called RADE3 [63]. The advantage of this new method is that it considers the varied snow accumulation on individual tanks rather than assuming uniform snow coverage.

### 4.3.2. Laputop3s3s

Laputop3s3s stands for Laputop 3 Stations 3 Steps. As the name suggests, it performs the reconstruction in a 3-step fit and requires a minimum of 6 HLC hits (so 3 pairs of IceTop tanks, as provided by the 3-station trigger) to perform the reconstruction.

There are two main differences between Laputop and Laputop3s3s. The first is the requirement of stations for the minimization to be performed. Laputop requires the 5-station trigger, while Laputop3s3 requires the 3-station trigger. The second lies in the minimization process, as later explained in this section.

For both reconstruction methods, the same input pulses are used; they are called "IceTopHLCSeedRTPulses" and are a set of processed HLC (Hard Local Coincidence) pulses provided by the Icetray software of the collaboration that went through a cleaning process involving the search for space and time pulse-clusters.

The pulse charge and time, as well as the position of the tanks that measured pulses, are used as input for the minimization process. The minimization procedure is carried out in three distinct steps. Table 4.1 and 4.2 show respectively the Laputop and Laputop3s3s steps and the fixed and free parameters of the minimization process. In the minimization process, a fixed parameter is not fitted during the minimization step, in contrast to the free parameter that is floating within a predefined range for finding the best minima in the minimization process. It is important to note the difference in Step 2. For Laputop, both the LDF and the time function are minimized simultaneously, whereas for Laputop3s3s only the time function is minimized. This difference makes Laputop require fitting 7 free parameters simultaneously, which is the primary reason for the 5-station trigger requirement.

Table 4.1.: Steps in the **Laputop** minimization process.

| Step | Fixed parameters | Free parameters |
|---|---|---|
| 1. LDF | $\theta, \phi, t_{\text{core}}$ | $x, y, \mathrm{S}_{125}, \beta$ |
| 2. LDF, time | - | $x, y, \mathrm{S}_{125}, \beta, \theta, \phi, t_{\text{core}}$ |
| 3. LDF | $\theta, \phi, t_{\text{core}}$ | $x, y, \mathrm{S}_{125}, \beta$ |

Table 4.2.: Steps in the **Laputop3s3s** minimization process.

| Step | Fixed parameters | Free parameters |
|---|---|---|
| 1. LDF | $\theta, \phi, t_{\text{core}}$ | $x, y, \mathrm{S}_{125}, \beta$ |
| 2. Time | $x, y, \mathrm{S}_{125}, \beta$ | $\theta, \phi, t_{\text{core}}$ |
| 3. LDF | $\theta, \phi, t_{\text{core}}$ | $x, y, \mathrm{S}_{125}, \beta$ |

Laputop and Laputop3s3s have been used to study the event reconstruction for the energy range $4.0 < \log_{10}(\mathrm{E_{MC}}/\mathrm{GeV}) < 7.0$. Their performances have been compared, and Laputop3s3s has shown similar results to Laputop at higher energies. Furthermore, Laputop3s3s successfully reconstructed a larger number of events at lower energies, which is advantageous for this study, as discussed in the following sections.

## 4.4. Quality Cuts

The reconstruction is successful if the minimizer finds a minimum in the parameter space. However, even if the minimum is found, some reconstructed events are not suitable for analysis, as they may be poorly reconstructed. The identification of such events is crucial for improving the accuracy of the analysis. The criteria that select the "good" events are commonly called "quality cuts". Generally, there are no universal quality cuts; rather, each analysis applies specific cuts depending on its objectives. For the gamma-ray search, the quality cuts are tuned based on two key quantities that need to be accurately reconstructed: the arrival direction and energy.

The method for both quantities is determined using Monte Carlo (MC) simulations of gamma-ray air showers, Section 3.1. The angular resolution is defined as the 68% quantile of the angle between the simulated and reconstructed directions. The energy resolution is based on an energy proxy, $S_{125}$, which represents the signal strength at 125 m from the shower axis. In particular, the linear correlation between $S_{125}$ and energy is seen on a double logarithmic scale.

For this analysis, the reconstruction method used is Laputop3s3s, and all the parameters are optimized to satisfy specific quality conditions. The simulations used are the ones described in Chapter 3. The number of CORSIKA simulations (Section 3.1.1) and the resampling radius (Section 3.1.2) differ for different energies. Hence, a weighting has to be applied to account for these effects. The weighting process is performed with `simweight` [74], which corrects the different number of simulations generated with a normalization based on the number of events. Similarly, it accounts for the different resampling radii with a surface normalization. Finally, `simweight` also allows for a flux assumption with a specific spectral index. In this way, the events can follow a more realistic spectrum than the one used in simulation. In this section, $\gamma = 3$ is the spectral index chosen.

The first requirement for tuning the quality cuts is a successful reconstruction, meaning that the minimizer has to have found a minimum during the minimization process. Figure 4.4 shows the angular resolution as a function of zenith angle and the simulated energy as a function of the energy proxy $S_{125}$. Both plots show two-dimensional histograms of gamma-ray simulations, weighted with a spectral index $\gamma = 3$. In the left-hand plot, the points represent the 68% percentile of the angular resolution, while in the right-hand plot, the black dots and segments indicate the means and one standard deviation from a Gaussian fit for each bin. Notably, the left plot uses uniform solid angle binning, while the right plot is linear in logarithmic scale.

From Figure 4.4, it is evident that a cut on $S_{125}$ is necessary. Specifically, events with $\log_{10} S_{125} < -1$, corresponding to about 100 TeV, are not well-fitted and should be excluded. Additionally, a cut on the zenith angle ($\theta$) can be applied, as this analysis focuses

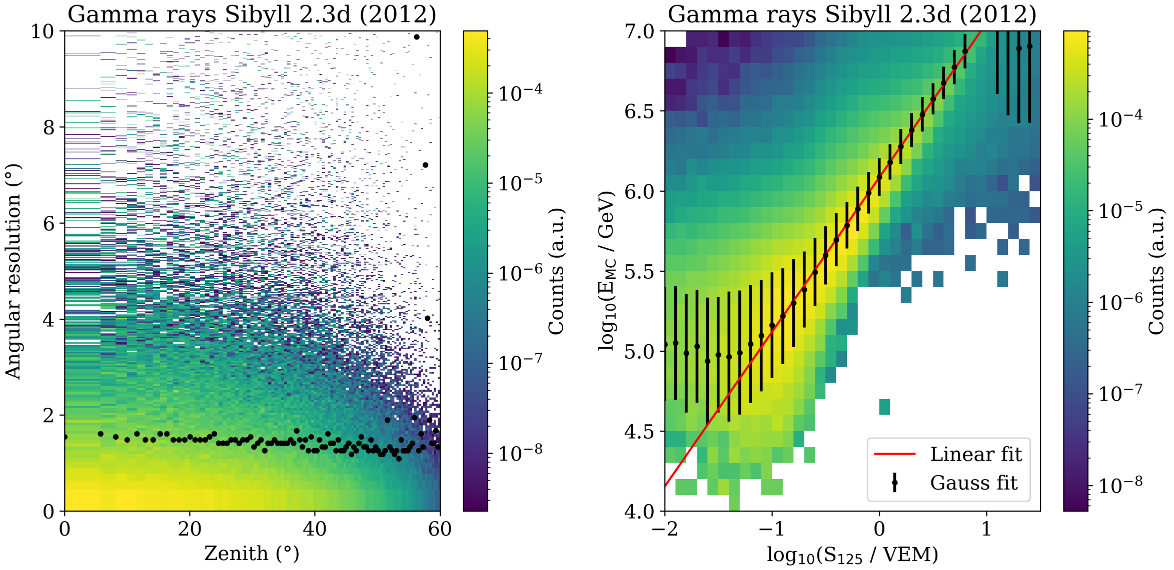

Figure 4.4.: Angular resolution as a function of zenith angle (left) and simulated energy as a function of $S_{125}$ (right). Both plots require a successful Laputop3s3s reconstruction and no further quality cuts. In the left-hand plot, the points represent the 68% percentile of the angular resolution, while in the right-hand plot, the black dots and segments indicate the means and one standard deviation from a Gaussian fit for each bin. The slope and intercept for the linear fit are 0.965(0.009) and 6.084(0.005), respectively.

on nearly vertical events. The chosen cut is $\theta < 38°$, about 5° larger than the one used for the final analysis, as will be explained later in Section 6.2.1.

Once the $S_{125}$ and the $\theta$ cuts are applied, one more quantity that must be analyzed is the reconstructed core position as a function of the distance from the center of the detector (radius), as shown in Figure 4.5. Based on this plot, a cut on the reconstructed core position is applied, with a maximum distance r < 500 m from the center of IceTop chosen. Beyond 500 m, the reconstruction quality deteriorates, and events are not fully contained within the detector.

The final quality cut is applied to the parameter $\beta$, which represents the slope of the lateral distribution function (LDF), as described in Eq. 4.2. This cut is mass-dependent, as the lateral particle distribution changes based on the primary particle that initiated the air shower. The cut to determine the optimal value was extensively discussed within the IceCube cosmic-ray working group. Figure 4.6 shows $\beta$ as a function of the simulated energy, after applying the $S_{125}$, $\theta$, and radius cuts. The black points and lines represent the mean and one standard deviation of the Gaussian fit for each bin. A window of $1.9 < \beta < 4.5$ is selected, as values outside this range are considered physically unrealistic, especially at higher energies where the events are mostly contained in this range. Thus, this window is chosen as a quality cut also at lower energies.

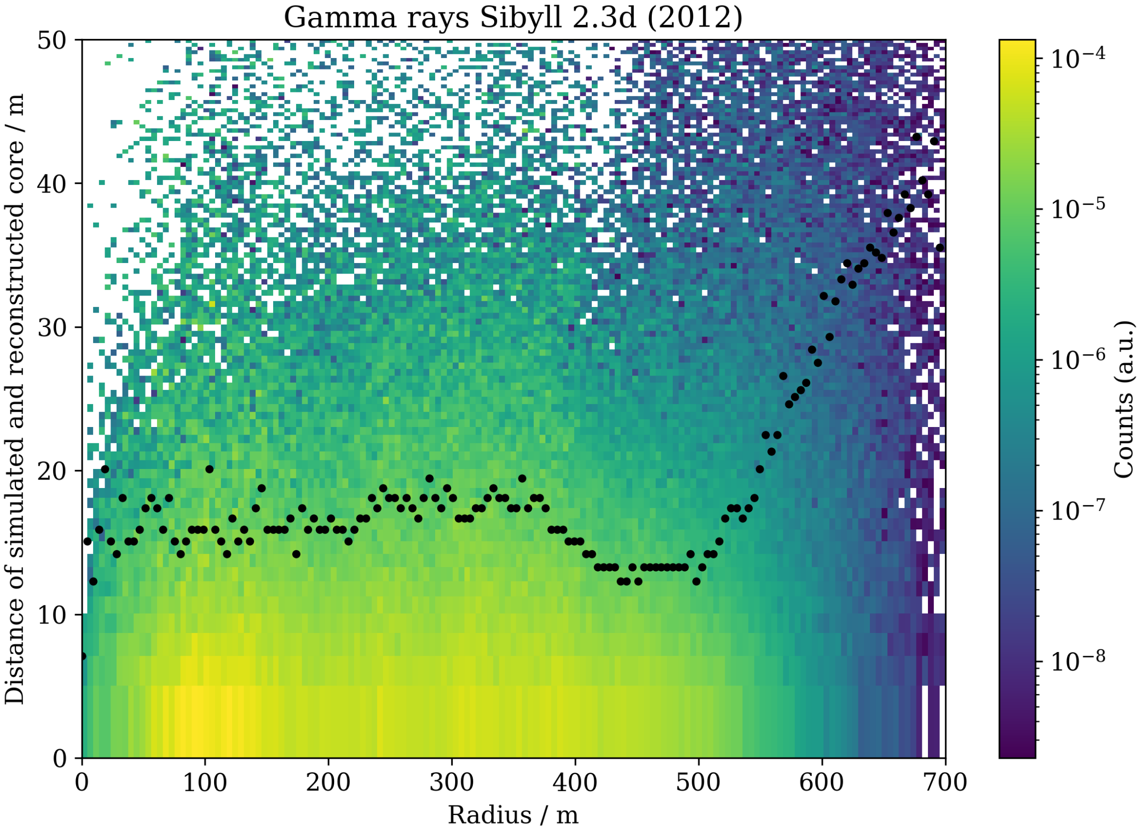

Figure 4.5.: Distance between the true and reconstructed core as a function of radius, i.e., distance $r$ from the center of the IceTop array. Applied quality cuts include a successful Laputop3s3s reconstruction, $\log_{10} S_{125} < -1$, and $\theta < 38°$. The black dots indicate the 68% quantile.

In summary, four main criteria are applied to select events based on the quality of the minimization fit, reconstructed position, zenith angle, and the slope of the LDF ($\beta$):

- Successful minimization of the fit
- Maximum distance from the center of the detector $r < 500$ m
- Zenith angle $\theta < 38°$
- Slope of the LDF parameter $1.9 < \beta < 4.5$

Figure 4.4 can now be compared to Figure 4.7, where all quality cuts are applied. Both figures use the same axis ranges for straightforward comparison. Notice the improvement in angular resolution and the enhanced correlation between energy and $S_{125}$. Before proceeding, it is essential to evaluate the reconstruction efficiency: the fraction of events that are properly reconstructed, i.e., pass all quality cuts, out of the total number of triggered events.

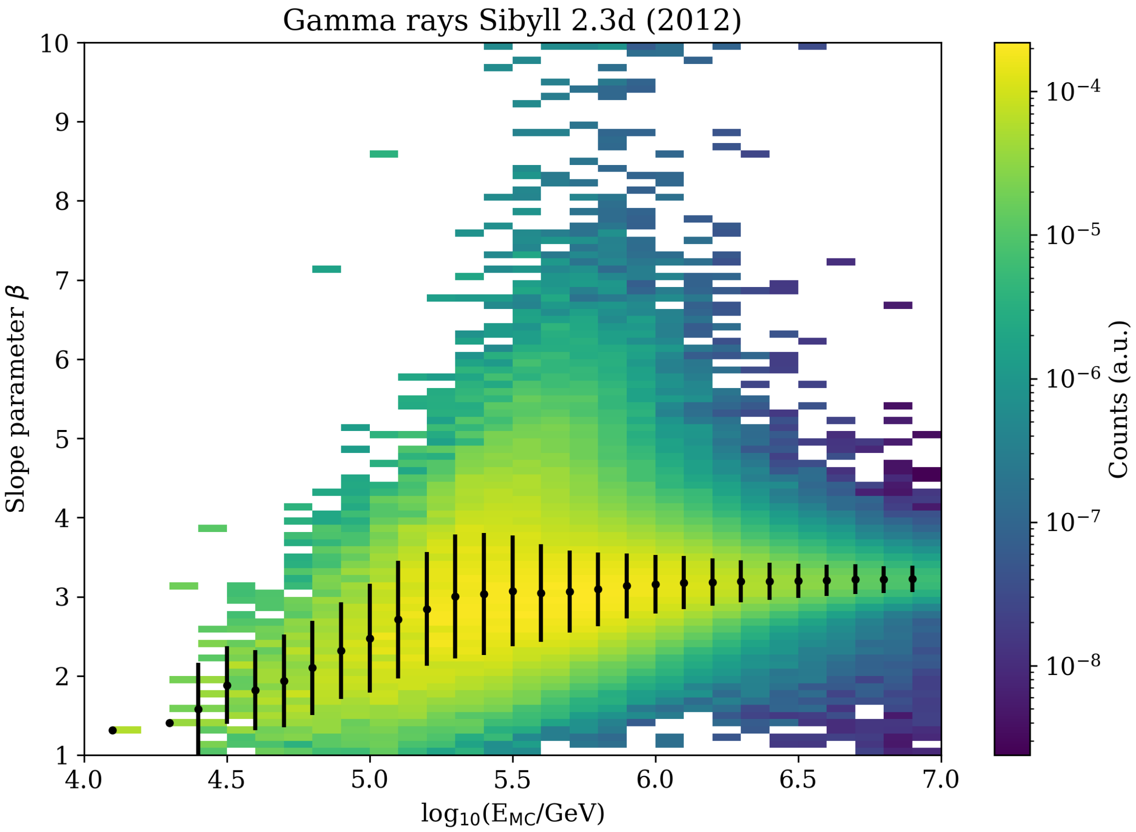

Figure 4.6.: Slope parameter $\beta$ as a function of the simulated energy. Applied quality cuts include successful Laputop3s3s reconstruction, $\log_{10} S_{125} < -1$, $\theta < 38°$, and $r < 500$ m. The back dots indicate the mean of the Gaussian fit, and the segment is the corresponding $1\sigma$.

## 4.5. Laputop3s3s validation

This section focuses on the validation of Laputop3s3s as a reconstruction method, as discussed in Section 4.3.2. The reconstruction of key parameters is compared between two primaries: gamma rays and protons. These primaries are used for the gamma-hadron separation study in Section 6.3. For all of the plots of this section, the following quality cuts are applied:

- Successful minimization of the fit

- $r < 500$ m

- $\theta < 38°$

- $1.9 < \beta < 4.5$

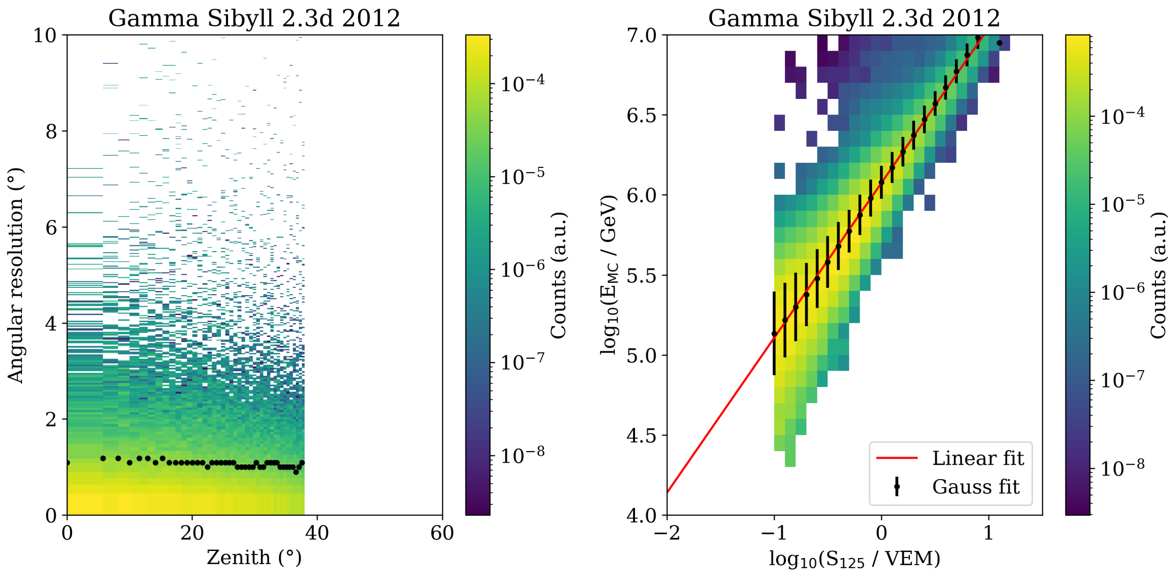

Figure 4.7.: Angular resolution as a function of zenith angle (left) and simulated energy as a function of $S_{125}$ (right), with all quality cuts applied. The x- and y-ranges are kept unchanged for a fair comparison with Figure 4.4. The slope and intercept for the linear fit are 0.968(0.008) and 6.074(0.004), respectively.

## 4.5.1. Reconstruction Efficiency

Reconstruction efficiency is defined as the fraction of successfully reconstructed events over the total number of events that generate a 3-station trigger. The events are selected within a simulated radius of $r < 500$ m and zenith angle $\theta < 38^\circ$. Figure 4.8 shows the reconstruction efficiency for Laputop3s3s (solid line) and Laputop (dashed line) for gamma rays (indigo) and protons (red). Both reconstruction methods achieve maximum efficiency $\eta > 98\%$ around $\sim$2 PeV. At lower energies, Laputop3s3s outperforms Laputop, with a reconstruction efficiency between 60% and 70%. However, in the lowest energy range, $\log_{10}(\mathrm{E}/\mathrm{GeV}) < 5.0$, low statistics lead to larger fluctuations in the determination of the reconstruction efficiency.

In conclusion, the ratio of reconstructed events with respect to the total events can be estimated from the combination of Figure 4.1 and 4.8. Figure 4.9 shows this quantity as a function of the energy. As expected, the number of events at low energies is higher for Laputop3s3s compared to Laputop. However, both methods reach full efficiency for energies $\mathrm{E} > 2$ PeV.

## 4.5.2. Angular Resolution

Angular resolution is crucial for identifying sources in a gamma-ray point-source search. Poor angular resolution increases contamination by the cosmic-ray background. The an-

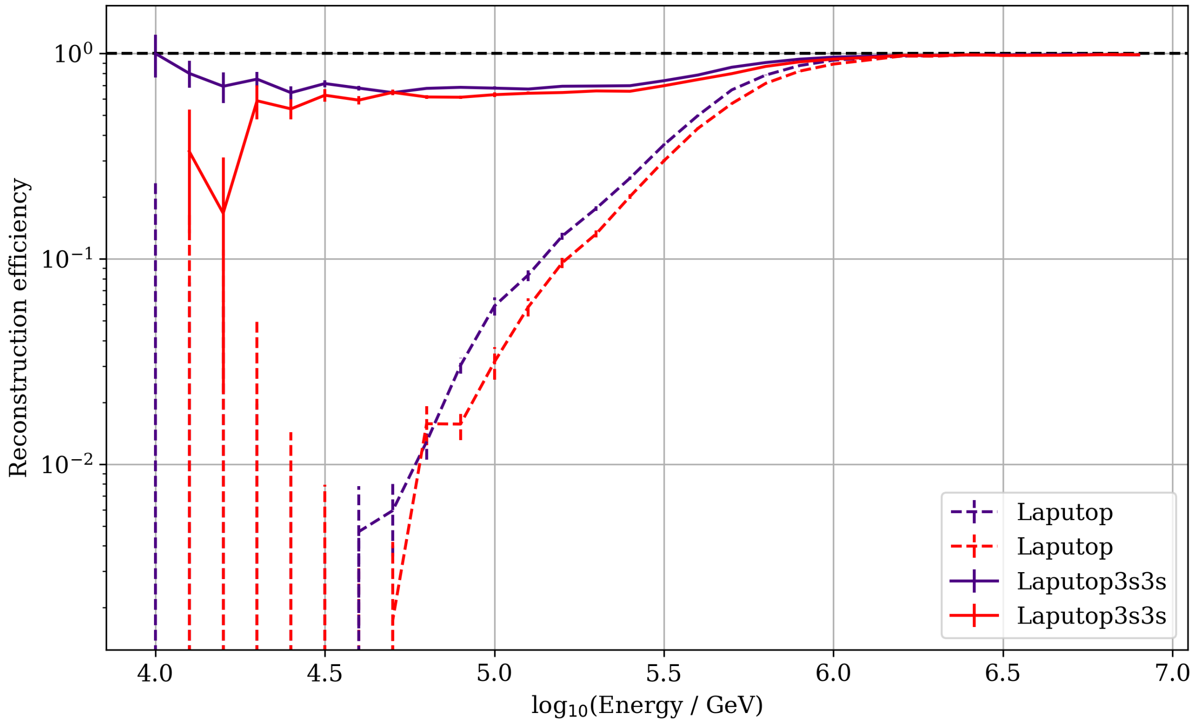

Figure 4.8.: Reconstruction efficiency of Laputop3s3s (solid line) and Laputop (dashed line) for gamma rays (indigo) and protons (red). The CORSIKA simulations are made with Sibyll 2.3d, and the detector response accounts for the 2012 snow level.

gular resolution of the IceTop array is energy-dependent. Figure 4.10 shows the angular resolution as a function of simulated energy for gamma-ray and proton air showers. The weighting used for the histogram plot corresponds to a spectral index assumption of $\gamma = 3$. The black dots indicate the 68% percentile. Due to the limited number of events for $\log_{10}(\mathrm{E}/\mathrm{GeV}) < 4.5$, the estimation of the angular resolution may fluctuate. For higher energies, the 68% percentile is less than 2 degrees, reaching sub-degree level above 1 PeV.

### 4.5.3. Energy Reconstruction

There is an approximately linear relationship between $\log_{10}(\mathrm{E}/\mathrm{GeV})$ and $\log_{10}(\mathrm{S}_{125}/\mathrm{VEM})$. Figure 4.11 presents the 2D histogram weighted by a spectral index $\gamma = 3$. The black dots and segments represent the mean and one standard deviation of the Gaussian fit in each bin. The red line shows the linear fit to the means, weighted by their standard deviations. The slope and intercept for the gamma-ray simulations fit are 0.960(0.008) and 6.075(0.005), respectively, whereas for the proton simulations 0.926(0.010) and 6.076(0.005).

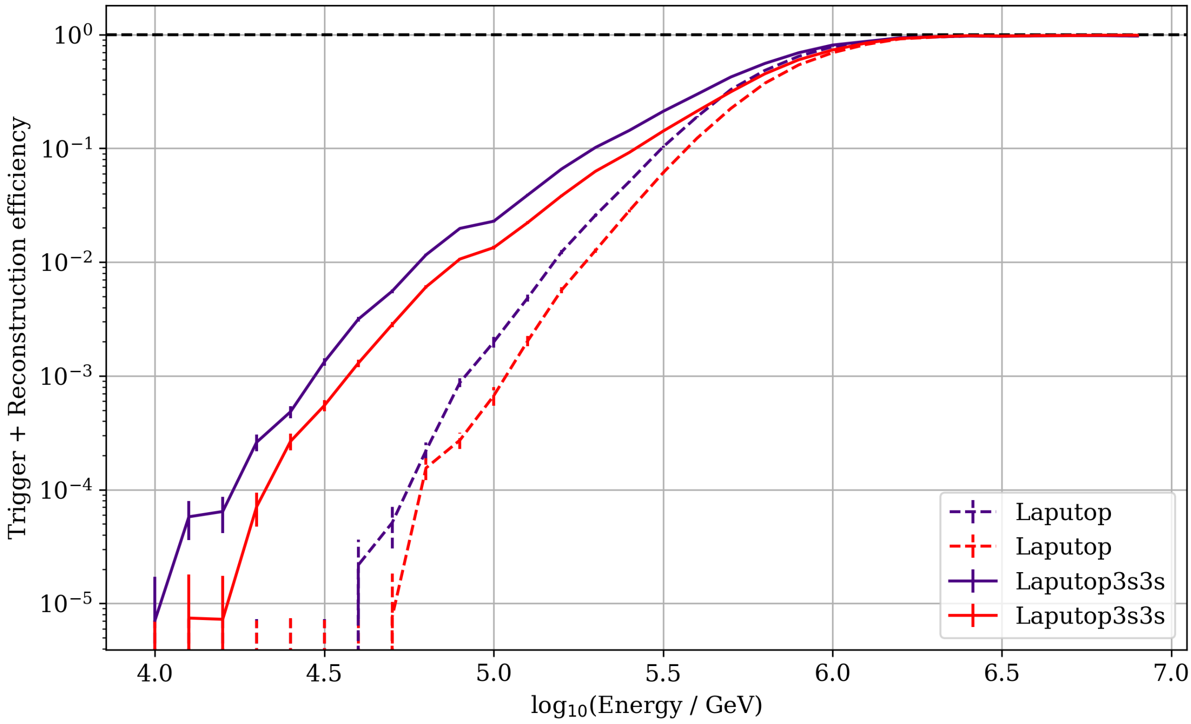

Figure 4.9.: The trigger and reconstruction efficiency combined for Laputop3s3s (solid line) and Laputop (dashed line) for gamma rays (indigo) and protons (red). The CORSIKA simulations are made with Sibyll 2.3d, and the detector response accounts for the 2012 snow level.

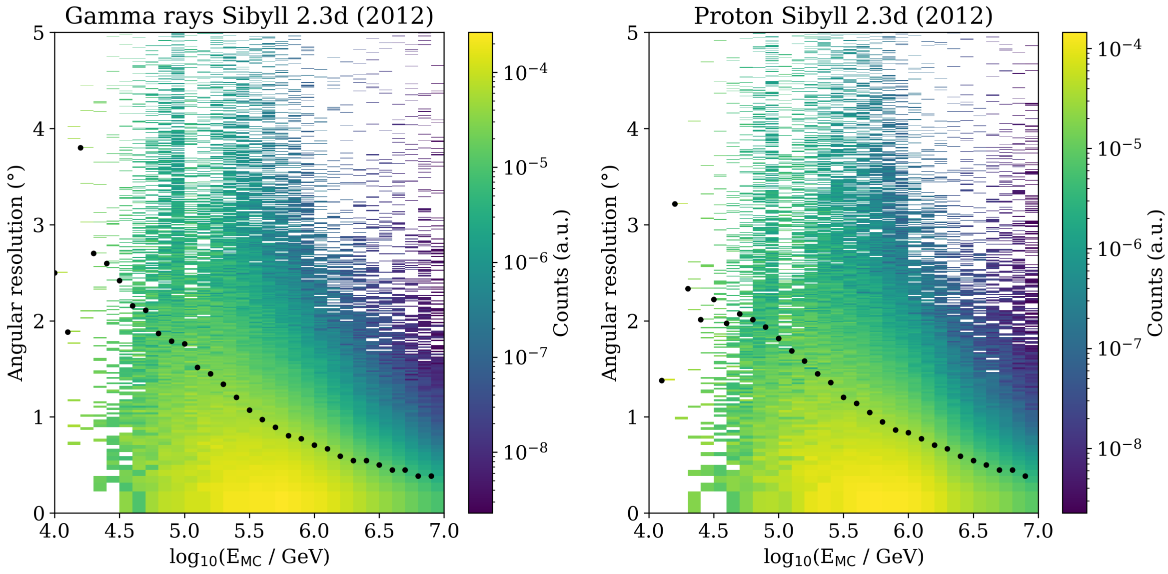

Figure 4.10.: Angular resolution as a function of simulated energy for gamma-ray and proton simulations, weighted by a spectral index $\gamma = 3$. The black dots represent the integrated 68% percentile.

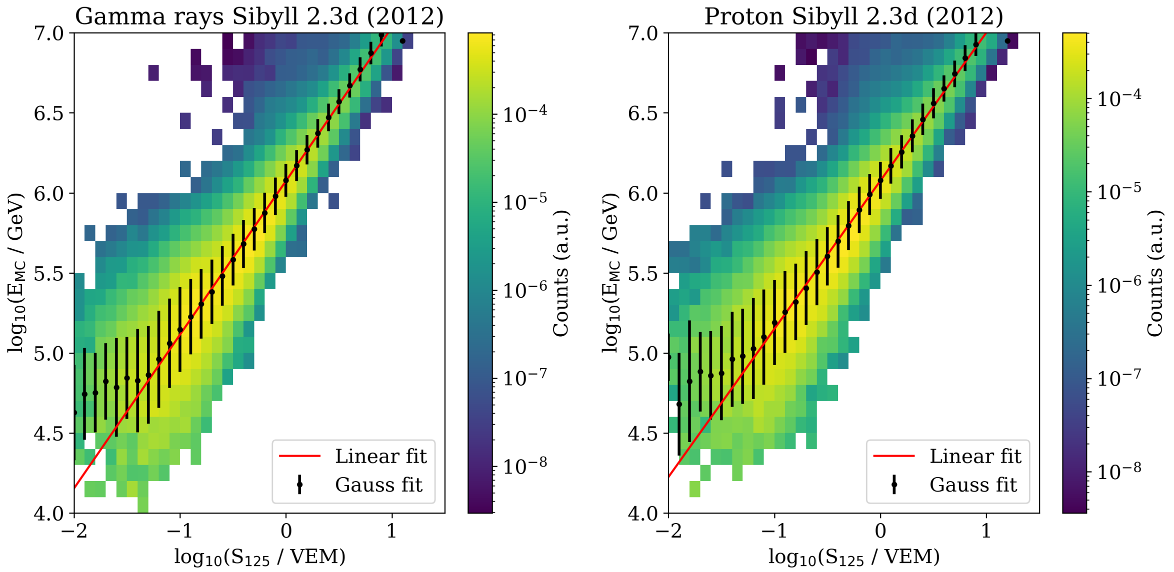

Figure 4.11.: 2D histogram weighted by a spectral index $\gamma = 3$. Black dots and segments represent the mean and $1\sigma$ standard deviation of the Gaussian fit for each bin. The red line shows the linear fit to the means, weighted by the standard deviation. The slope and intercept for the gamma-ray simulations fit are 0.960(0.008) and 6.075(0.005) respectively, whereas, for the proton simulations 0.926(0.010) and 6.076(0.005)

### 4.5.4. Core Position

Figure 4.12 shows the core resolution as a function of simulated energy for gamma-ray and proton air showers. The plot is a 2D histogram of simulations weighted by a spectral index $\gamma = 3$. The black dots indicate the 68% containment, which is the measure for the core resolution. As with angular resolution, low statistics for $\log_{10}(\mathrm{E}/\mathrm{GeV}) < 4.5$ lead to fluctuations. At higher energies, the 68% containment is less than 20 m, reaching below 10 m for E > 1 PeV.

### 4.5.5. Outlook on reconstruction

Laputop3s3s has been demonstrated to be a valid reconstruction method and has shown improvements over Laputop, the standard reconstruction method, at sub-PeV energies. Due to the 3-station requirement, Laputop3s3s is capable of successfully reconstructing a larger number of sub-PeV events compared to Laputop, making it a more suitable method for gamma-hadron separation studies in this energy range.

Furthermore, Laputop3s3s has demonstrated comparable performance to Laputop in the PeV energy range and can successfully reconstruct both gamma-ray and proton air showers.

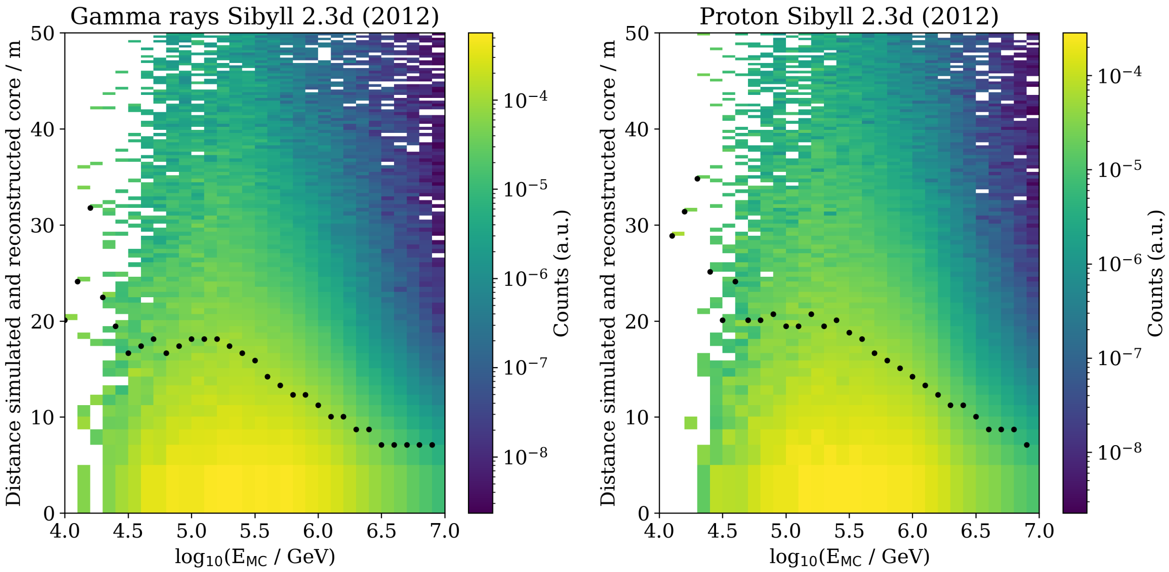

Figure 4.12.: Core resolution as a function of simulated energy for gamma-ray and proton air showers. The plot is a 2D histogram weighted by a spectral index $\gamma = 3$. Black dots indicate the integrated 68%.

Following the development and approval of the Laputop3s3s reconstruction method by the IceCube collaboration, an important contribution was made by Vergara Carrasco, Sebastian, in his Master's thesis [76]. In that work, Laputop3s3s was implemented in a newer reconstruction framework for IceCube called Rockbottom [77]. Additionally, various reconstruction methods have been tested, leveraging the flexibility of the new framework. For example, the reconstruction was performed by allowing $\kappa$ in Equation 4.2 to be a free parameter or by including SLC hits in the LDF fit [78]. This can further enhance the reconstruction quantity for future studies.

# 5. Single tank hits calibration

The muon component of air showers generally triggers SLC hits (deposited signal in only one of the two tanks of an IceTop station, as described in Section 2.1). Hence, they play a central role in the gamma-hadron separation, as described in Section 6.2.2.
This chapter focuses on the calibration process of SLC hits. It starts with a general description of the calibration, presents the motivation and primary challenges, and outlines the approach to calibrating SLC hits. The linear correlation between the HLC (signal coming from the two tanks of a station, Section 2.1) and SLC hits is studied, and the determination of the crossover points of the three Analog-to-Waveform Digitizers (AWDs) in each DOM is explained. In conclusion, a general discussion on the crossover points and their future calibration is presented.

## 5.1. Pulse Calibration

All pulses recorded by IceCube undergo a process of calibration. For IceTop pulses, this involves a time and a charge calibration. The latter converts the photomultiplier signal recorded by a DOM into units of vertical equivalent muons (VEM).

### 5.1.1. Time Calibration

Time calibration ensures that all events are synchronized to a common time standard. This is achieved via a master clock, a device located at the IceCube Lab that uses a GPS-based time. The master clock converts each timestamp recorded into Coordinated Universal Time (UTC). This process compares the local oscillator time of each DOM to the precise time signal of the master clock. The timing accuracy is generally constant throughout all the DOMs and at the level of a few nanoseconds [58].

### 5.1.2. Charge Calibration

Charge calibration is a more complex process. It involves a multi-step procedure that starts with measuring the deposited charge in ADC counts and completes once all three Analog Transient Waveform Digitizers (ATWDs) in each PMT are correctly calibrated. Part of this process is done already at the South Pole, while the final steps are instead done in the North. Figure 5.1 shows a schematic view of the charge calibration process.

This Section will briefly explain Steps 1-4. A complete and detailed description can be found in [58]. Afterward, the focus will be on the "New calibration". This is specifically relevant for IceTop SLC hits recorded by the 3-station trigger.

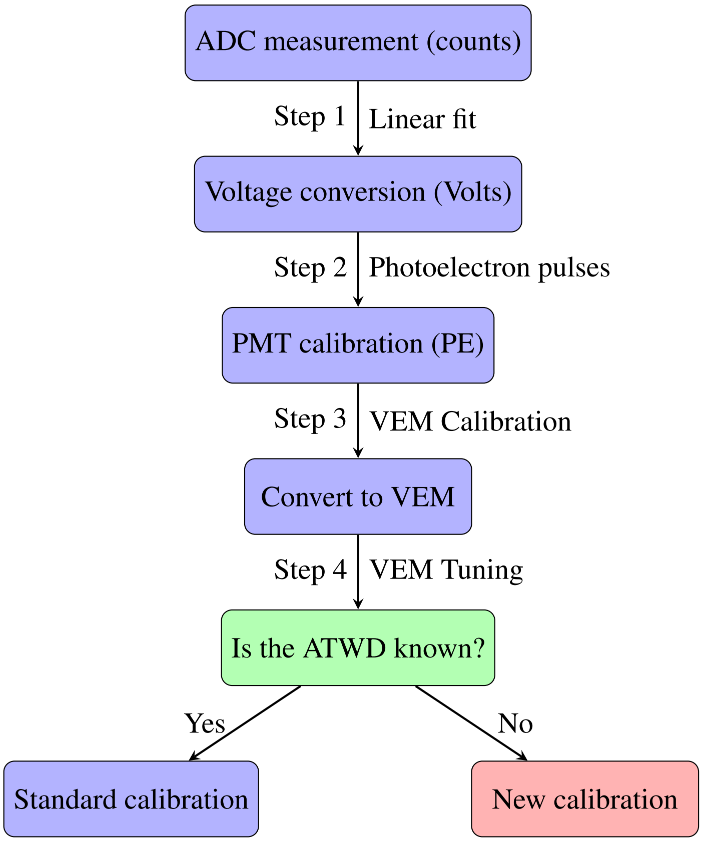

Figure 5.1.: Scheme of the pulses calibration process.

The Analog Transient Waveform Digitizer (ATWD) performs the readout of the PMTs in the DOMs. The first step in the charge calibration is carried out by converting the ADC counts of the ATWD to voltages. This is done using a linear fit to the ADC counts obtained by applying reference voltages of varying intensity. Following this, the ATWD gains are calibrated using single photoelectron pulses. This process converts Volts into Photoelectron (PE) units [58].

The final conversion is done in the North and converts PE to “Vertical Equivalent Muon” VEM units. This calibration is based on the average signal generated by one vertical muon traversing the tank. The average muon energy at IceTop is approximately 2–2.5 GeV, with minimum ionizing muons depositing a predictable amount of energy as they pass through the ice in the tanks, which is about 165 MeV. The 1 VEM reference unit is defined by measuring the muon peak position determined through a well-defined fitting procedure [58].

The last step in the calibration is the VEM tuning on the ATWD level. This final conversion allows a calibration on the multi-DOM level that is independent of the specific properties of each tank. This final tuning can be performed only if the ATWD channel information, stored in the waveforms, is known. For HLC hits, waveforms are recorded and always saved for each event. However, waveforms are only saved for SLC hits if the event has a 5-station trigger, thus, at least 10 HLC hits in addition to any number of SLC hits. Consequently, the SLC-hit calibration cannot be performed via the standard method for events with fewer than ten HLC hits.

## 5.2. A new approach for the SLC calibration

In contrast to SLC hits, the ATWD information is always available for HLC hits. Thus, the fine-tuning calibration of SLC hits with the unknown ATWD channel can be performed using the known ATWD channels for HLC hits [79].

The HLC hits are de-calibrated back to the Voltage values. The uncalibrated hits are now duplicated into two sets and PE calibrated. In particular, one set is calibrated following the HLC hit process and one the SLC one. In this way is possible to correlate each HLC-calibrated hit to its corresponding SLC-calibrated hit. The correlation between HLC and SLC hits can now be studied.

### 5.2.1. The HLC and SLC hits correlation

To investigate the procedure mentioned above, the data from run number 120160 of 2012 are used. This run corresponds to about 8 hours of data taking and is used for all plots of this section.

Figure 5.2 illustrates the correlation between the HLC-calibrated charge ($q_{\mathrm{HLC}}$) and the corresponding SLC-calibrated charge ($q_{\mathrm{SLC}}$), both expressed in PE units. For this plot, the charges from the DOM identified by the dom key "OMKey(56,61,0)" are used as an example. The de-calibration is performed by going back to the measured voltage. This charge is now converted twice into PE units: once under the assumption that it was an HLC hit ($q_{\mathrm{HLC}}$) and once that it was a SLC hit $q_{\mathrm{SLC}}$.

The relationship between $q_{\mathrm{HLC}}$ and $q_{\mathrm{SLC}}$ can be modeled with a linear function:

$$q_{\mathrm{HLC}} = p_0 + p_1 \cdot q_{\mathrm{SLC}}, \tag{5.1}$$

where the slope ($p_1$) and intercept ($p_0$) are treated as free parameters. It is important to note that the parameters $p_0$ and $p_1$ are neither universal across all DOMs nor constant over time. In particular, each DOM has two chips (0 and 1) and three ATWDs (0, 1, and 2), resulting in six possible combinations per DOM. Consequently, each DOM requires six separate slopes and intercepts. Furthermore, these parameters vary over time. Thus, periodic recalibration is necessary. In IceCube, this calibration process is

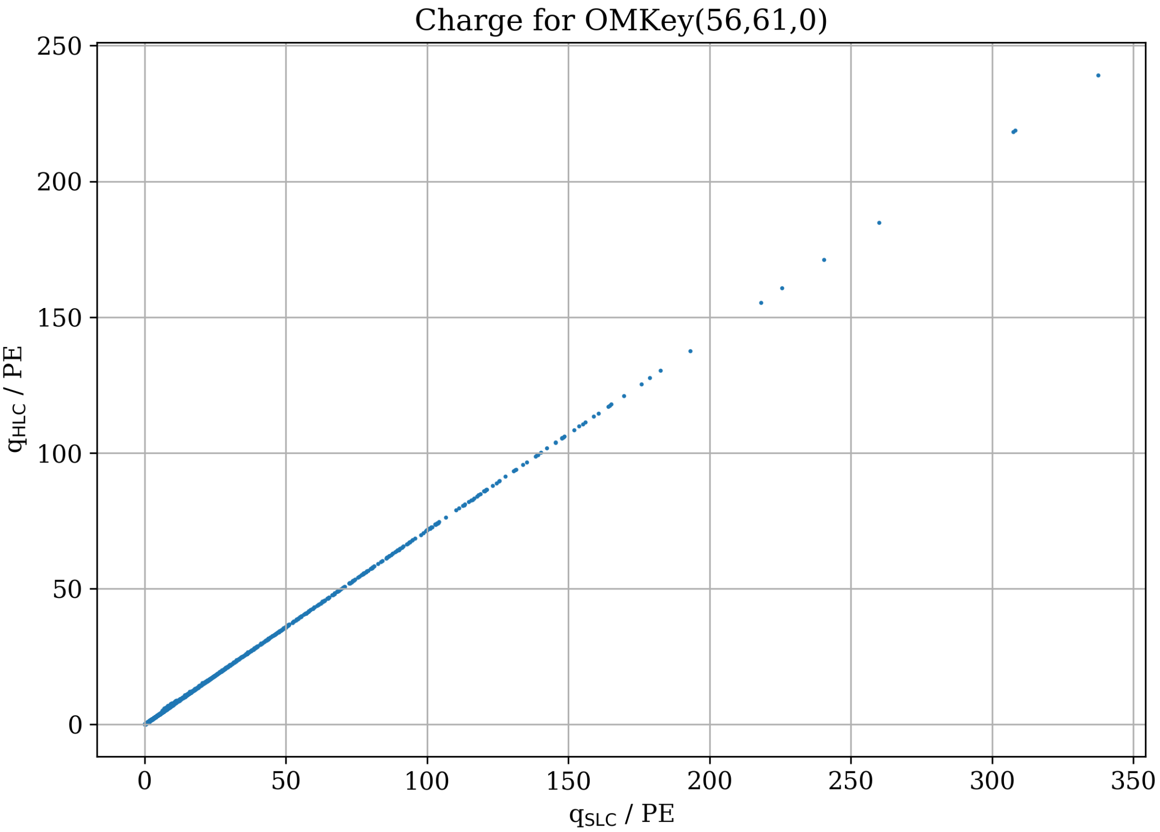

Figure 5.2.: Llinear correlation between the de-calibrated HLC charge ($q_{\mathrm{HLC}}$) in PE units and the corresponding (assumed to be) SLC charge ($q_{\mathrm{SLC}}$) also in PE units.

typically performed every two weeks. In this time frame, all runs are aggregated, and the slopes and intercepts are recalculated for this calibration period.

The mathematical framework for the linear regression and its associated errors goes as follows [79]. Given $N$ data points with index $i$ $(x_i, y_i)$, the following aggregated sums are defined:

$$S_x = \sum_i x_i, \quad S_{xx} = \sum_i x_i^2, \quad S_y = \sum_i y_i, \quad S_{yy} = \sum_i y_i^2, \quad S_{xy} = \sum_i x_i y_i \tag{5.2}$$

From these, the intercept $a = p_0$ and slope $b = p_1$ are calculated via a $\chi^2$ minimization:

$$\chi^2 = \sum_i (y_i - (a + bx_i))^2. \tag{5.3}$$

Their corresponding errors are computed as follows:

$$\Delta = NS_{xx} - (S_x)^2 \tag{5.4}$$

$$a = \frac{S_{xx}S_y - S_x S_{xy}}{\Delta}, \quad \sigma_a = \sqrt{\frac{S_{xx}}{\Delta}} \tag{5.5}$$

$$b = \frac{NS_{xy} - S_x S_y}{\Delta}, \quad \sigma_b = \sqrt{\frac{N}{\Delta}} \tag{5.6}$$

Expressing Equation 5.3 using the definitions of *a* and *b* from Equations 5.5 and 5.6, respectively, obtaining:

$$\chi^2 = S_{yy} - 2aS_y - 2bS_{xy} + a^2N + 2abS_x + b^2S_{xx} \tag{5.7}$$

Since the errors on *a* and *b* are unknown, it is assumed that each data point has a variance of 1. Consequently, the errors on the intercept (*a*) and slope (*b*) must be divided by an additional factor, resulting in the expressions:

$$\Delta a = \frac{\sigma_a}{\sqrt{\chi^2/(N-2)}}, \quad \Delta b = \frac{\sigma_b}{\sqrt{\chi^2/(N-2)}}. \tag{5.8}$$

In conclusion, only the sums defined in Equation 5.2 need to be calculated to determine the slope and intercept within a two-week time frame. This calculation must be repeated for all combinations, amounting to 162 DOMs × 2 PMTs × 2 Chips × 3 ATWD, resulting in a total of 1944 pairs of values for the IceTop array that are stored.

### 5.2.2. The Analog-to-Waveform Digitizer determination

Once the linear relation between HLC and SLC is established and all slope-intercept pairs are stored, the ATWD channel estimation based on the PE charge can be investigated. Figure 5.3 shows the histogram of all SLC charges and the different colors represent the different ATWD channels. The histogram shows a reasonable separation between each ATWD channel.

To correctly estimate the ATWD channel based on the PE charge, two charge values have to be determined. These charge values, at which transitions between ATWDs occur, are referred to as crossover points (COPs). Reliably identifying these COPs is essential to ensure accurate calibration of the measured charges. For this purpose, Kernel Density Estimation (KDE) is used to determine the COP values. KDE generates a smooth probability density function, providing an analytical representation of the charge distribution and offering a precise determination of COPs.

In Figure 5.3, the histograms for each ATWD are fitted with Gaussian KDEs using the Scipy Python library [80], as previously described. The fits are shown as solid lines, with each color corresponding to its specific ATWD channel. The COPs are then calculated

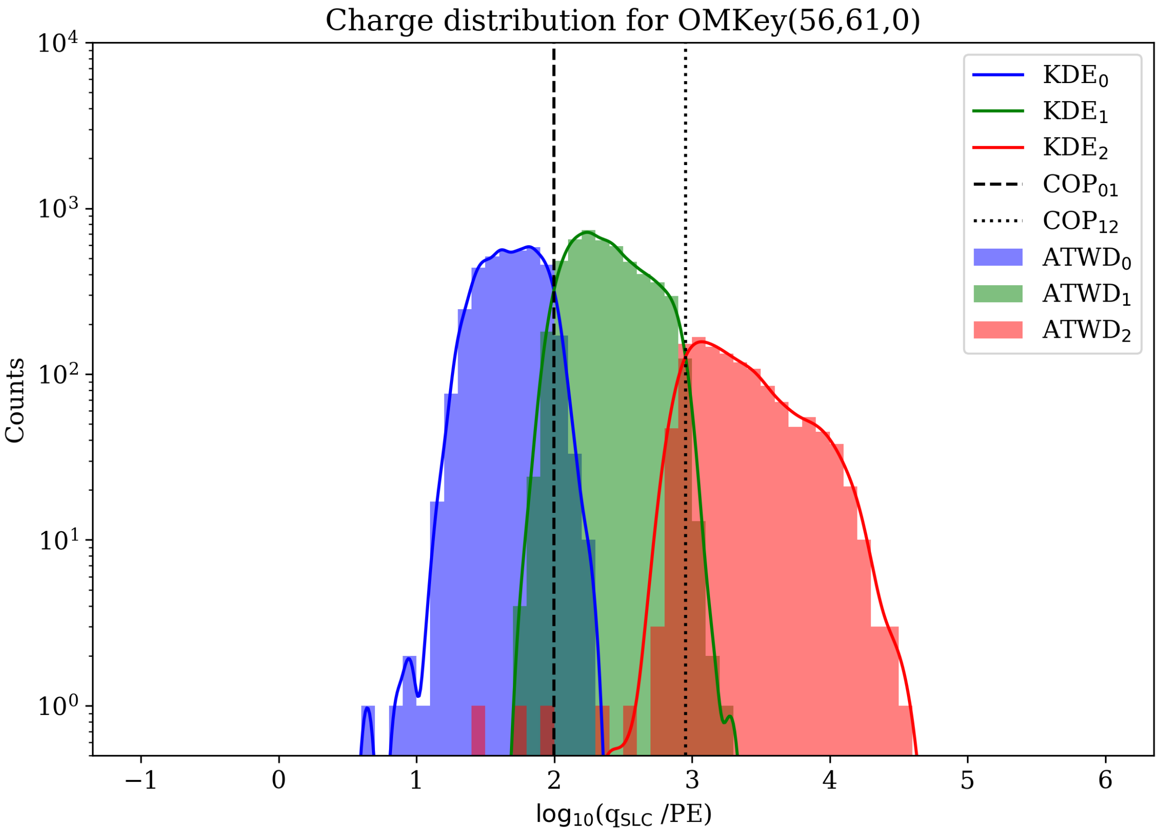

Figure 5.3.: Histogram of all SLC charges. Different colors represent a different ATWD, with KDEs shown as solid lines. COP$_{01}$ is the crossing point of the KDE 0 and 1 and analogously COP$_{12}$ is the crossing point of KDE 1 and 2.

by identifying the intersection points of the KDE fits, using the `scipy` library's `brentq` method [80]. Specifically:

- COP$_{01}$ is determined by finding the intersection of KDE 0 and KDE 1.
- COP$_{12}$ is analogously determined by the intersection of KDE 1 and KDE 2.

### 5.2.3. The crossover points (COPs)

Once all COPs are determined for every ATWD of each DOM, their distributions can be analyzed. Figure 5.4 depicts the distributions of both COPs in all DOMs for both high-gain (HG) and low-gain (LG) PMT, as each DOM has two PMTs, one with HG and the other with LG. In the figure, the solid color represents HG PMTs, while the translucent color corresponds to LG PMTs. Each PMT has two COPs, indicating the transitions between ATWDs: from ATWD0 to ATWD1 (COP$_{01}$) and from ATWD1 to ATWD2 (COP$_{12}$)

The COP values span several orders of magnitude, depending on the gain type and the specific ATWD transition. In particular, a significant variation is observed also for the same type and gain of COPs. This means that the calibration the determination of COP have to be done for all PMTs individually.

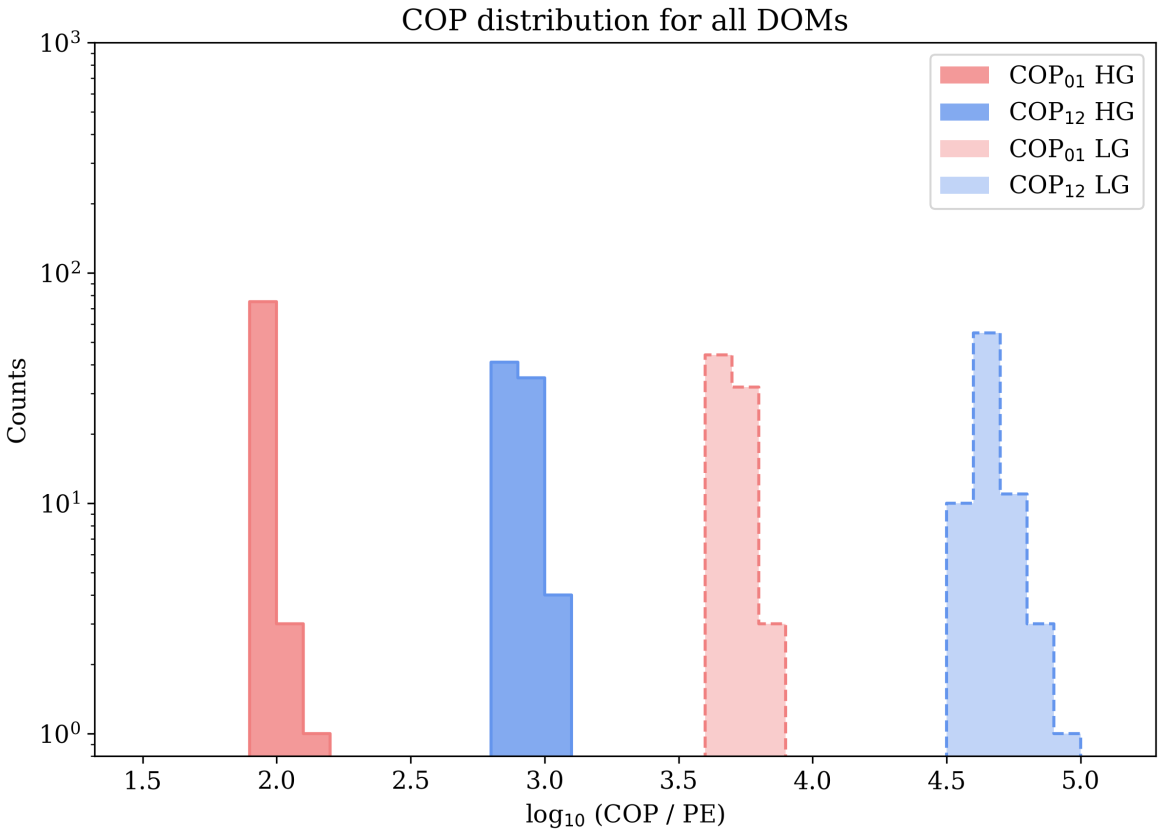

Figure 5.4.: Distributions of both COPs across all DOMs for high- and low-gain PMTs. The color indicates the type of COP, and the color translucence is the type of gain. Each PMT has two COPs, indicating the transitions between ATWDs: from ATWD0 to ATWD1 ($COP_{01}$) and from ATWD1 to ATWD2 ($COP_{12}$)

### 5.2.4. The COP validation

Figure 5.5 shows two validation plots for the quality of the ATWD estimation and calibration. Figure 5.5a compares the uncalibrated SLC charges to the once calibrated with the new method and the standard calibration method used for calibrating the 5-station trigger events. The comparison shows how this new calibration method improves the tail of the distribution, giving a better agreement with the standard calibration method.
Figure 5.5b shows the confusion matrix for the calibration. The DOM (56, 61, 0) is used again as an example. The majority of events are correctly associated with the corresponding ATWD. Generally, less than 10% of events are classified incorrectly. This

results in a mostly correct estimation of the ATWD channel and, consequently, a correct calibration of the SLC hit.

In conclusion, the calibration of SLC on an ATWD base is now also possible for events for which the ATWD channel is unknown, in particular, for events with less than 10 HLC hits.

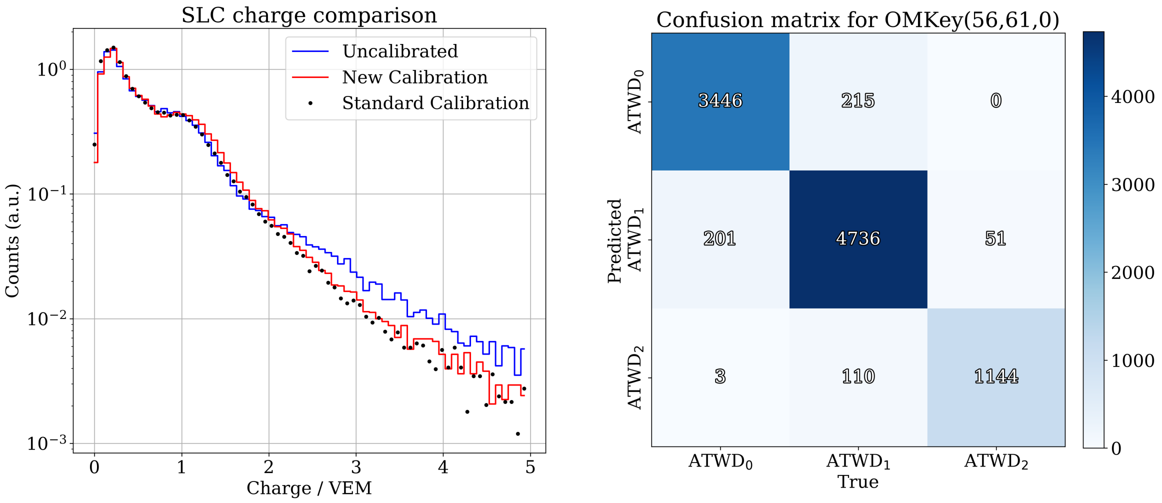

(a) SLC charges plotted before and after the calibration on the ATWD base. The 5 station events (Standard Calibration) are used as a reference; for them, the waveforms are stored, and the standard approach is used.

(b) Confusion matrix for the DOM (56, 61, 0): most events lie on the diagonal which means a correct estimation of the ATWD.

Figure 5.5.: Results of the new calibration approach.

## 5.3. Towards a standardized SLC calibration

The calibration scripts are hosted on GitHub [81]. They were designed with flexibility to enable the calculation of all necessary calibration values directly at the South Pole. The calculated values can afterward be transmitted to the north via a compact JSON file, typically only a few kilobytes in size. This simplifies the overall data transmission process. Once the COPs and calibration parameters $p_0$ and $p_1$ are determined, they are stored as calibration values with the other values from Equation 5.2. The code supporting this functionality has also been implemented and saved in the same GitHub repository.

The ultimate objective of the SLC calibration is to have a standard analysis pipeline, where all the calibration values are stored in the "GCD" file, which contains the Geometry, Calibration, and Detector information. This simplifies the process and avoids reliance on separate files. The scripts developed for this calibration laid the groundwork for this final step, which was completed [82]. Furthermore, the final aim for the SLC

calibration is to fully automate the process, eliminating the need to recalculate COPs and repeat the linear calibration for each run. This would optimize the computational request and minimize the time requirements.
To address these challenges, the detector geometry information has been leveraged for SLC calibration. This subsequent work [82] demonstrated a correlation between COPs obtained using the original method and those derived from the GCD file. The latter streamlines the calibration process, facilitates automation, and improves efficiency.

# 6. Gamma-Hadron Separation

This chapter focuses on gamma-hadron separation and how it can be performed for the IceCube Neutrino Observatory. Multiple approaches for the gamma-hadron separation have been investigated and presented at conferences [83, 84, 85]. Here, the method that proved to be most successful is presented. In light of the recent LHAASO discoveries of PeV photons in the Northern Hemisphere, an estimation of event rates is calculated based on LHAASO-like mock sources [47], assuming that one such source would be within the IceCube's field of view. Furthermore, the significance is calculated using the Li & Ma [86] method and is employed to tune the selection cuts by maximizing the discovery potential of such sources. The parameters used for selecting gamma-ray candidate events, namely the in-ice signal and Charge-Distance at IceTop, are introduced and discussed. Finally, an upper limit on the fluxes is calculated.

## 6.1. Significance and Sources

This section focuses on mock sources as possible gamma-ray candidates in the IceCube Field of View (FOV). The term "mock source" in this section refers to a hypothetical source that could be in the IceCube FOV with the same flux as a specific LHAASO source. It is important to note that *none* of the LHAASO sources are visible in the IceCube FOV. Therefore, such mock sources are assumed to be observed within a zenith angle of $5^\circ < \theta < 10^\circ$.

The number of gamma-ray events of such a mock source is obtained by integrating the flux of the source over a fixed period of 365 days and a surface area of approximately 0.785 $\text{km}^2$, corresponding to a circular region with a radius of 500 m.

The background is calculated using 10% of the airshower events measured by IceCube in 2012. The zenith range between 5 and 10 degrees is taken, and the density of events per solid angle is determined.

Using the number of signal and background events obtained after quality cuts and gamma-ray selection cuts, it is possible to estimate the statistical significance of each mock source, assuming that a similar source is located at that zenith position.

### 6.1.1. The Li & Ma significance

In gamma-ray astronomy, a widely used statistical method for estimating the significance of an observation is given by the Li & Ma significance [86], also known as the $\mathrm{N_{on}}$-$\mathrm{N_{off}}$ method. The estimation of the significance via this method is done by measuring the number of events on a source, the number of events off the source, and the observation times. The advantage of this method is the reliability and accuracy in calculating the significance per source, considering different observation times. In the special case of IceCube, the observation time is the same for both on- and off-source regions. Because of the unique location of IceCube, it always observes the same portion of the sky.
The Li & Ma significance $S$ is given by:

$$S = \sqrt{2}\left[N_{\mathrm{on}} \ln\left(\frac{1+\alpha}{\alpha}\frac{N_{\mathrm{on}}}{N_{\mathrm{on}}+N_{\mathrm{off}}}\right) + N_{\mathrm{off}} \ln\left((1+\alpha)\frac{N_{\mathrm{off}}}{N_{\mathrm{on}}+N_{\mathrm{off}}}\right)\right]^{1/2} \tag{6.1}$$

Where $N_{\mathrm{on}}$ is the number of events observed in the *on-source* region (signal + background), $N_{\mathrm{off}}$ is the number of events observed in the *off-source* region (background only) and $\alpha$ is the ratio of the exposure (or observation time) of the on-source region to the off-source region: $\alpha = \frac{\text{Exposure on-source}}{\text{Exposure off-source}} = 1$ for IceCube, if the size of on- and off-source regions is the same.

### 6.1.2. LHAASO-like mock sources and background estimation

To use the Li & Ma significance (Equation 6.1), the number of signal and background events must be known. This section explains how these values are estimated.
The number of background events is estimated from 10% of the measured IceCube events under the realistic assumption that the number of gamma-ray events in the sample is much smaller than the cosmic-ray background. The zenith range $5^\circ < \theta < 10^\circ$ is used for calculating the total number of events. Hence, the density per solid angle can be calculated, and as a result, the background flux per steradian is known:

$$\frac{dn(E)}{d\Omega ds} = \frac{N_{5^\circ<\theta<10^\circ}(E)}{2\pi \cdot (\cos(5^\circ) - \cos(10^\circ)) \cdot t}. \tag{6.2}$$

Equation 6.2 mathematically shows how the number of events per steradian is calculated. Here, $N_{5^\circ<\theta<10^\circ}(E)$ indicates the measured number of events in the zenith range $5^\circ < \theta < 10^\circ$ and in a specific time interval $t$, which in the case of burnsample corresponds to about 32 days, 15 hours, 24 minutes, and 25 seconds. Finally, the density of events per solid angle and time is calculated by dividing the total time and solid angle of the zenith range $\Omega_{5^\circ<\theta<10^\circ} = 2\pi \cdot (\cos(5^\circ) - \cos(10^\circ))$. The number of background events from a certain region of the sky depends on the opening angle; the larger the opening angle, the larger the number of background events. Assuming a point source, the opening angle depends on the uncertainty of the direction reconstruction of the shower axis. Thus, the number of background events can be calculated using the opening angle values shown in Figure 4.10. Hence, the the number of background events as a function of energy $N_{bg}(E)$ is estimated:

$$N_{bg}(E) = \frac{dn(E)}{d\Omega ds} \cdot \Delta\Psi(E) \cdot \Delta t, \tag{6.3}$$

where $\Delta\Psi(E)$ is the solid angle given by the angular resolution as a function of energy and $\Delta t$ the time interval.

To estimate the Li & Ma significance, the number of background events is combined with the number of signal events. Thus, the number of expected gamma-ray events has to be calculated. For this purpose, the LHAASO-like mock sources are considered. As previously mentioned, *none* of the LHAASO sources are visible in IceCube's FOV. However, their flux can be used to estimate events if a LHAASO-like mock source were visible. The differential fluxes from the LHAASO catalog of gamma-ray sources [47] are in the form of:

$$\frac{dN}{dE\,dA\,ds} = N_0 \left(\frac{E}{E_0}\right)^{-\gamma} \tag{6.4}$$

where $E_0 = 50$ TeV, $N_0$ with units of $10^{-16}$ TeV$^{-1}$ cm$^{-2}$ s$^{-1}$ and $\gamma$ depend on the source.

Figure 6.1a shows the total number of events that reach a circular surface with radius $r = 500$ m in a year. This total number of events is obtained by integrating each energy step of 0.1 in $\log_{10}(E/\text{GeV})$ as a function of the energy for a few selected sources. The number of events follows a power law and decreases rapidly with energy. However, this is not yet the number of events that IceTop could detect. For this, it is necessary to account for the trigger efficiency (Section 4.1) and the reconstruction efficiency (Section 4.4). Figure 6.1b shows the expected number of events with the applied efficiencies. In addition, the expected number of background events $N_{bg}(E)$ is shown with a dashed line. The background is calculated via the measured data as previously described, and accounts for the angular resolution $\Delta\Psi(E)$, as explained in Equation 6.3.

Figure 6.1b shows that the number of expected gamma-ray events is orders of magnitude smaller than the expected background events. Consequently, the observation of possible gamma-ray sources with IceTop is possible only if the gamma-hadron separation provides sufficient background suppression, and a sufficient number of gamma-ray events is retained.

The following section shows how the method for the gamma-hadron separation for the 2012 dataset was developed and optimized.

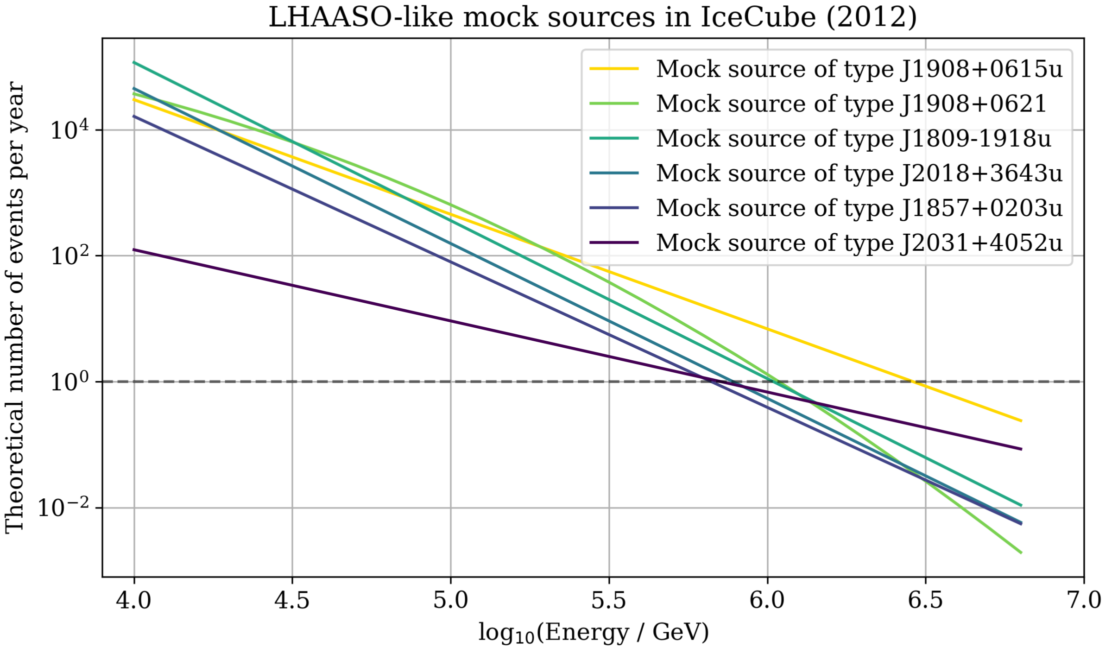

(a) Rate of photons hitting the area of IceTop.

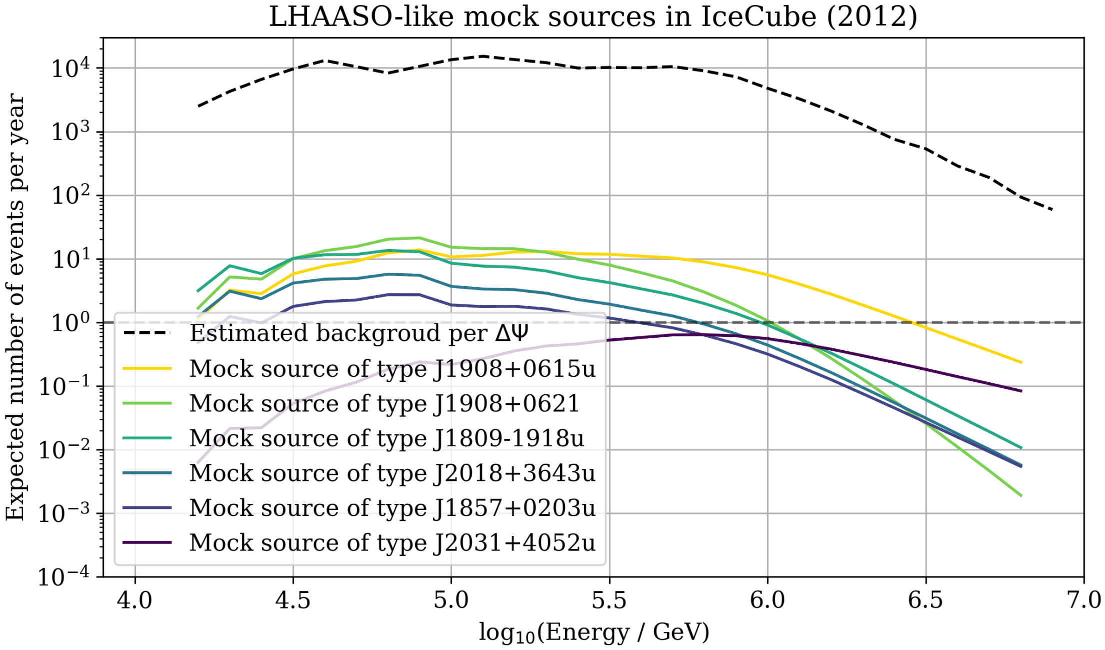

(b) Expected number of detected IceTop events as a function of energy, with trigger and reconstruction efficiency applied. The expected cosmic-ray background in $1\sigma$ angular resolution $\Delta\Psi(E)$ is calculated via the measured data.

Figure 6.1.: Theoretical and expected number of gamma-ray events from different LHAASO-like mock sources for a circular surface with radius $r = 500$ m in a year. The number of events is obtained by integrating over each energy bin of 0.1 in $\log_{10}(E/\text{GeV})$.

## 6.2. Selection criteria for the identification of gamma rays

As explained in Section 1.5, the major differences between gamma-ray and hadron-initiated air showers are in the muon content and compactness of the footprint of the showers. To exploit these features, two methods have been developed for the separation of gamma-ray and hadronic showers detected by IceCube. In particular, the in-ice detector is used to estimate the high-energy muon component of the shower, and the IceTop to measure the Charge-Distance for the compactness of the footprint caused by the muons generating a signal away from the core.

Figure 6.2 qualitatively shows the importance of the in-ice detector for measuring the high-energy muon component of air showers. Here, the ratio of simulated air showers without any muon with an $\mathrm{E} > 273\mathrm{GeV}$, for a zenith angle range $\theta < 38°$, is plotted as a function of energy. In particular, all the proton simulated air showers, with a simulated energy ($\mathrm{E_{MC}}$) $\log_{10}(\mathrm{E_{MC}}/\mathrm{GeV}) > 5.5$, had at least one muon with energy above the threshold. This confirms that using the in-ice detector for measuring high-energy muons is crucial for a successful gamma-hadron separation. The number of simulated air showers per energy bin can be found in Table 3.1.

### 6.2.1. Selection of in-ice events

The in-ice detector is used to classify showers with a high-energy muon content as background events. The in-ice signal is correlated to the energy deposited by the muons in the detector. Hence, the signal must be isolated from the environmental and electronic noise via a signal-cleaning procedure. This is achieved by a multi-step process.

The first requirement is that the air-shower axis must be contained in the in-ice volume. Otherwise, the in-ice signal cannot be correlated to the air shower. The in-ice containment $C_{\text{in-ice}}$ is defined via the ratio of the distance from the center of the in-ice detector to the shower axis $r$ and the distance between the center and the edge of the detector along the same direction $R$: $C_{\text{in-ice}} = r/R$. Figure 6.3 shows a schematic view of the detector with the two distances $r$ and $R$. For this analysis, a $C_{\text{in-ice}} < 0.9$ has been chosen.

Due to the containment, the in-ice selection criteria will restrict the zenith range to a maximum of about 32° and result in a zenith-dependent event selection. Figure 6.4 shows the result of the selection for three different datasets. Namely, measured data, gamma-ray simulations, and proton simulations, respectively, from left to right. The energy range is $-1.0 < \log_{10}(\mathrm{S_{125}}/\mathrm{VEM}) < 1.0$, equivalent to about $5.0 < \log_{10}(\mathrm{E}/\mathrm{GeV}) < 7.0$. In each plot, the "good" events that survive the quality cuts discussed in Section 4.4 are used as the reference dataset. The solid line represents the reference value of 1, representing the good events. The dashed line is the ratio of the number of good events contained in the in-ice detector with respect to the total number of good events. Finally,

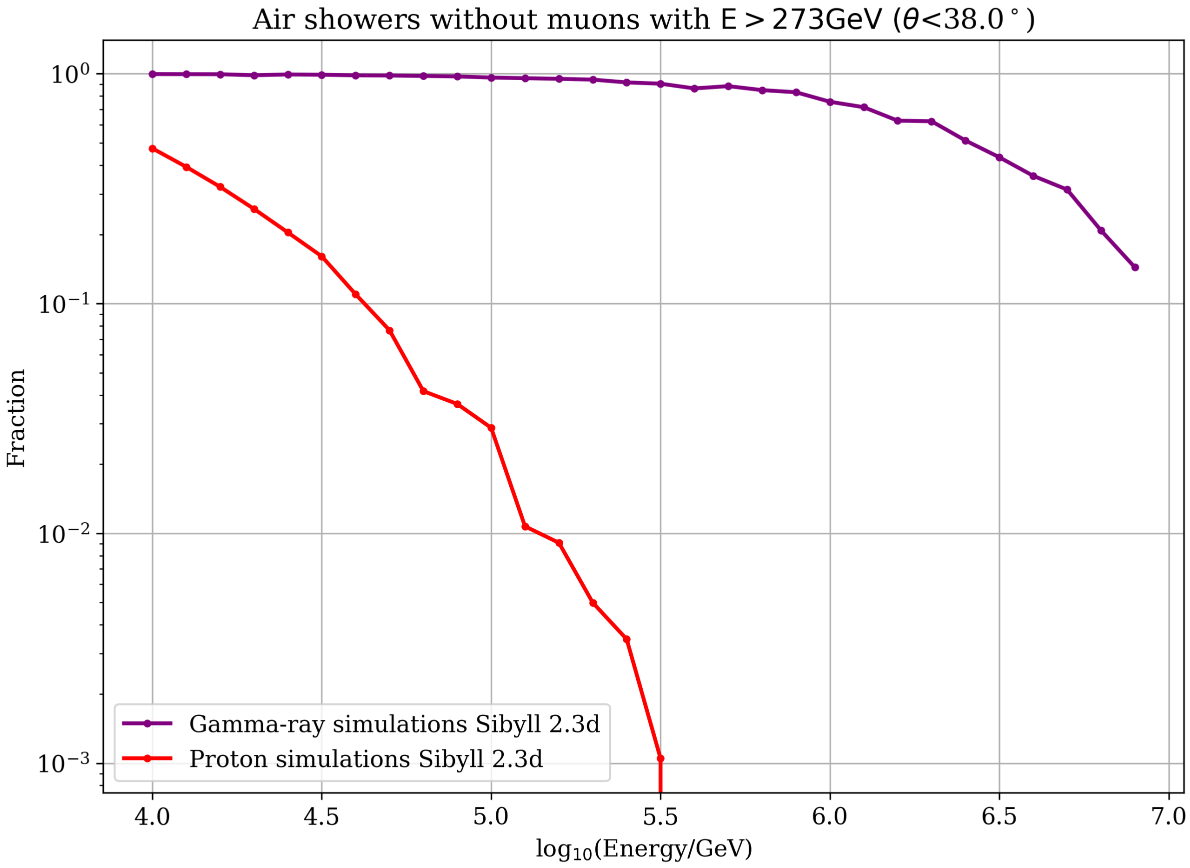

Figure 6.2.: Ratio of simulated air showers without a muon with an $E > 273\text{GeV}$, for a zenith angle $\theta < 38°$. For proton air showers with $\log_{10}(E_{MC}/\text{GeV}) > 5.5$, all the simulated air showers had at least one muon with an energy above the threshold. The number of simulated air showers per energy bin can be found in Table 3.1.

the dotted line is the ratio of gamma-ray candidate events to the number of good events. The criteria for the selection of gamma rays are discussed in the following sections. However, some observations can already be made. First, the number of events that are contained is rapidly declining as a function of zenith, which is simply due to geometrical reasons. Second, the majority of gamma-ray simulations survive the selection criteria of the gamma-hadron separation method, but this is not the case for proton simulations and measured data. Finally, the amount of measured data that remains is smaller than that for proton simulations. This is expected because the measured data contain a mixed composition with heavier elements, which generally have a larger high-energy muon content compared to proton air showers.

## The in-ice pulses cleaning

Events contained in the in-ice detector must undergo a cleaning procedure before being used reliably for analysis. This process aims at isolating the signal by removing the

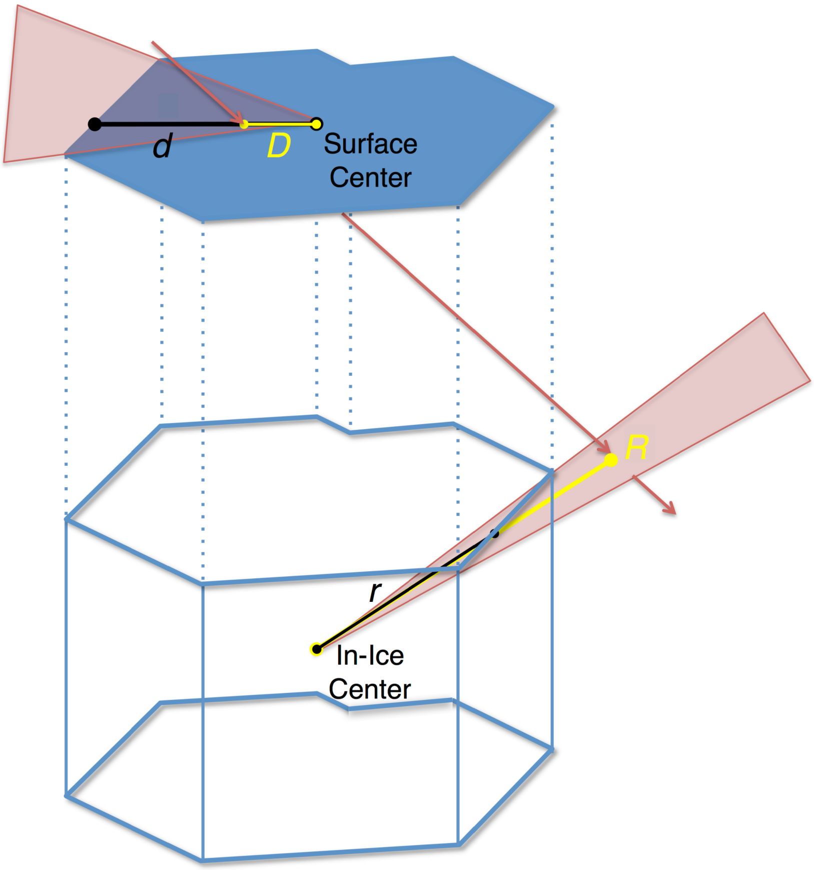

Figure 6.3.: In-ice containment is defined as $C_{\text{in-ice}} = r/R$. Taken from [42]

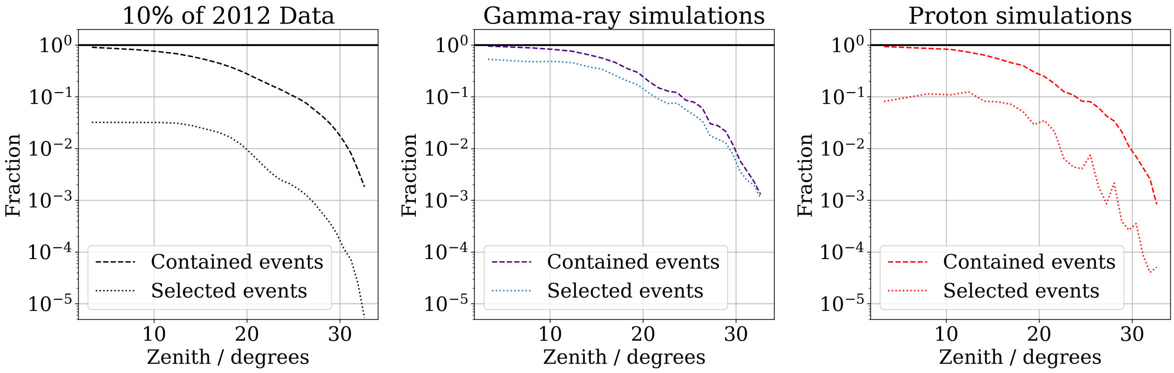

Figure 6.4.: Distribution of the events as a function of the zenith angle for three different datasets. The solid line is the reference value of 1, representing the "good events" surviving the quality cuts. The dashed line is the ratio of the number of good events contained in the in-ice detector with respect to the total number of good events. The dotted line is the gamma-ray candidates selected events. The energy range considered is $5.0 < \log_{10}(\mathrm{E/GeV}) < 7.0$.

environmental and electronic noise background on an event basis. The cleaning consists of an event selection based on a time window. Only in-ice pulses with a timestamp that

starts 400 ns after the reconstructed time are kept. In this case, the reconstructed time is used as a reference and indicates when the shower axis crosses the IceTop detector.
The time-window cleaning generally removes the majority of the noise; however, noise in coincidence with the air shower can still be present. For this reason, another selection criterion is used for background suppression. It consists of selecting a predefined number of superficial layers of the in-ice detector to understand the origin of the signal recorded. For this purpose, only a subset of the in-ice layers closest to the surface is taken into account. The assumption is that if the first $n$-layers do not record any signal, all the remaining pulses in the in-ice detector can be classified as background pulses, but a signal in these first $n$-layers may indicate a high-energy muon present in the air shower.
Figure 6.5 shows the in-ice signal after cleaning the time window for an air shower simulated with a gamma ray (Figure 6.5a) and a proton (Figure 6.5b). The main difference is in the detection of an in-ice signal. The proton air shower has a clear in-ice signal generated by the high-energy muon component of the air shower. In contrast, the gamma-ray air shower shows no signal, except for some minimal environmental noise. This proves the importance of the in-ice detector for gamma-hadron separation.

### The in-ice significance estimation

The estimation of the best number "$n$" of layers is performed via the maximization of the Li & Ma significance [86] as already discussed in Section 6.1.1. For the correct calculation of the significance, the number of signal events and background events is required. The signal is calculated for the LHAASO-like mock source from Figure 6.1b with the selection of $n$-layers applied. If an event has any signal in the first $n$-layers of the deep IceCube detector, the event is classified as a background event; otherwise, it is selected as a possible gamma-ray candidate. For this selection, in-ice pulses after cleaning the time-window are used, as previously discussed. It is now possible to vary the number of layers and calculate the Li & Ma significance each time. Figure 6.6 shows the result of this process. On the y-axis, the maximum value of the reachable significance is plotted as a function of the first "$n$"-layers of the in-ice detector. Here, three sources are chosen as an example. For both, it can be noticed that the maximum significance is usually reached with the first 5 layers.

## 6.2.2. The Charge-Distance selection

Section 6.2.1 has shown how the non-detection of high-energy muons of air showers in the in-ice detector can be used for gamma-hadron separation. However, exclusively relying on the in-ice array does not provide an optimal suppression of hadronic showers. For this reason, the surface detector is also used. The idea is to create a metric that uses

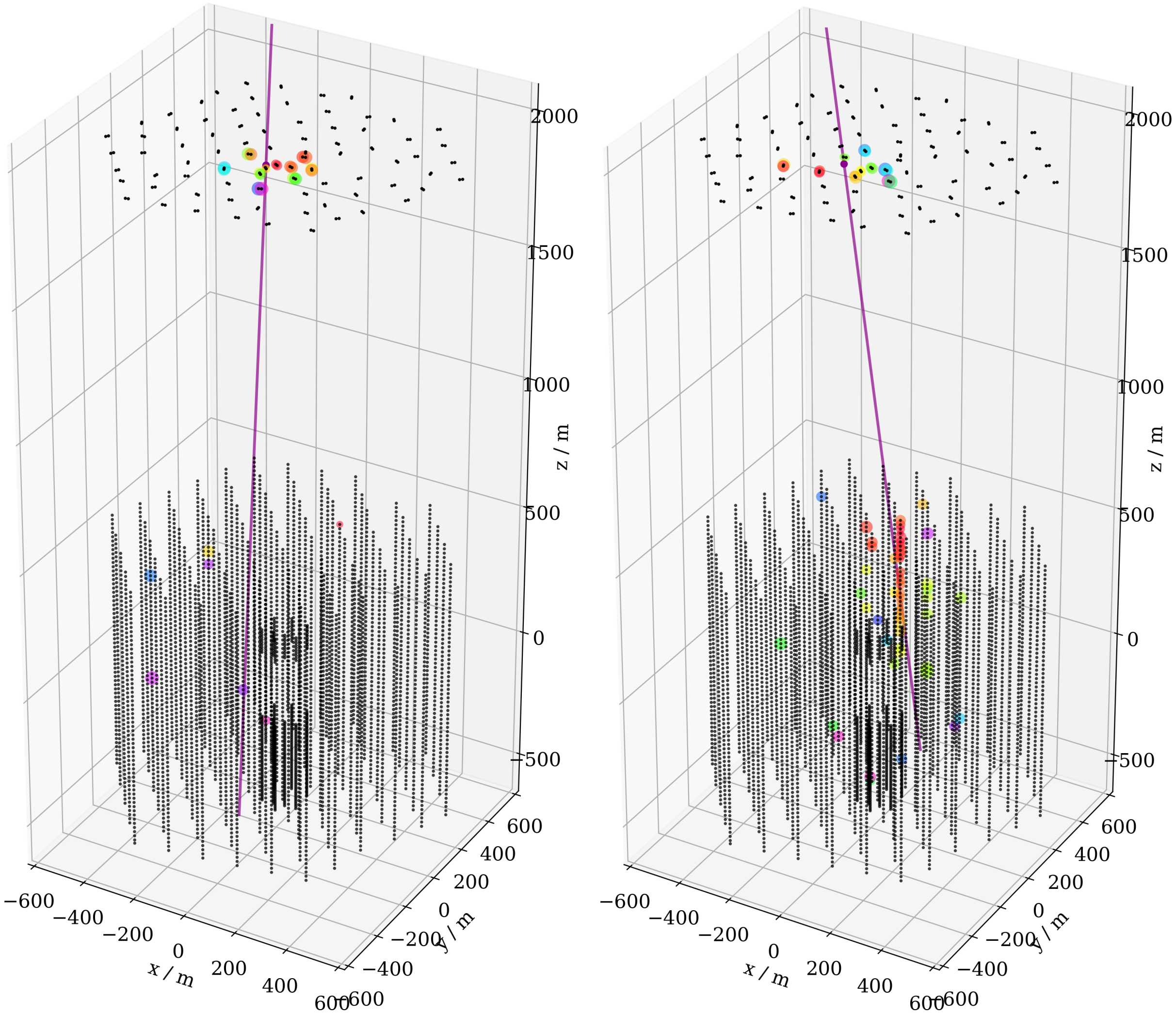

(a) The in-ice cleaned signal of 1 PeV gamma-ray air shower.

(b) The in-ice cleaned signal of 1 PeV proton air shower.

Figure 6.5.: In-ice signal for a gamma-ray and a proton simulated air-shower. The color indicates the time following the rainbow scheme, early (red) and late (blue). Plot made with the Event viewer, Appendix A.

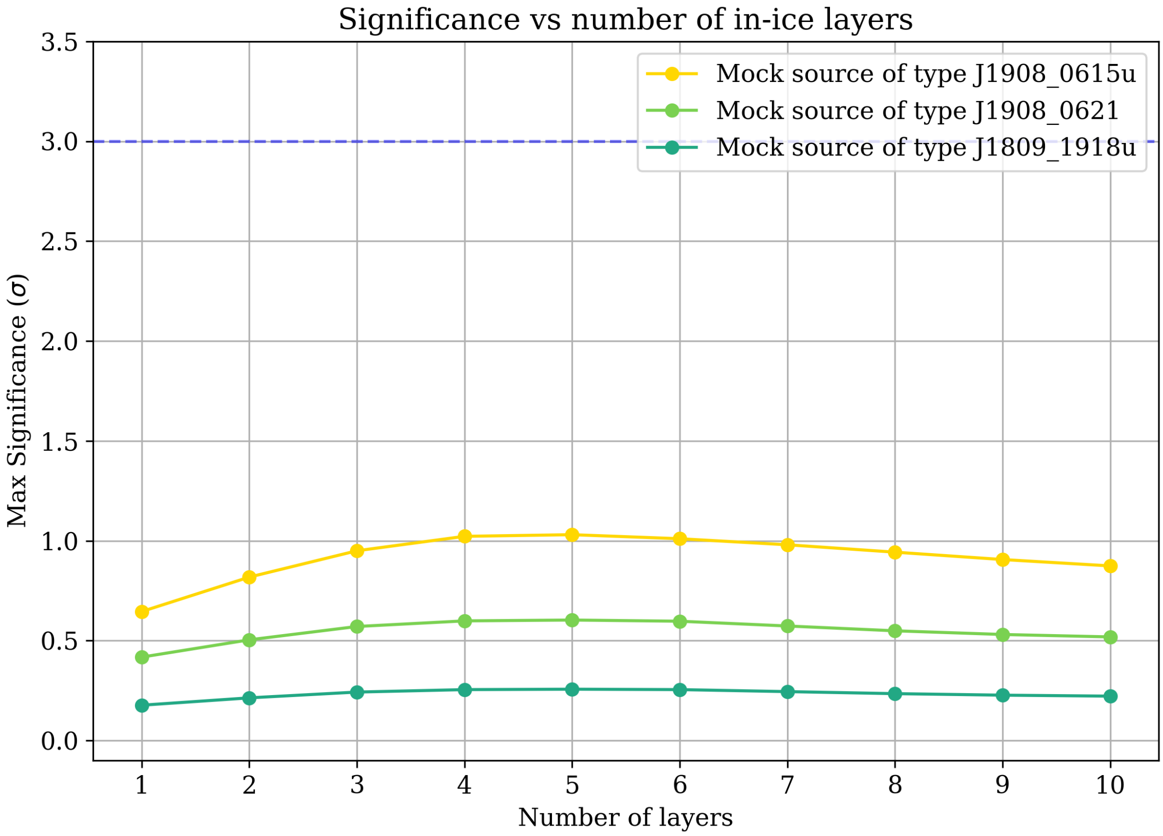

Figure 6.6.: Li & Ma significance for 1 year of IceCube data (2012) as a function of different numbers of the in-ice layers used to suppress hadronic air-showers. The maximum significance is reached for both mock sources when considering the first 5 in-ice layers, when only the in-ice selection is applied. The energy range considered is $5.0 < \log_{10}(\mathrm{E/GeV}) < 7.0$.

the lateral distribution of the surface detected pulse charges to exploit the compactness of the footprint caused by the muons of the air shower. A new heuristic empirical quantity called Charge-Distance (CD) has been developed for this purpose. It is defined as follows:

$$\mathrm{CD} = \log_{10}\left(\sum_i \left(\frac{q_i}{0.1\mathrm{VEM}}\right)^{\frac{\sqrt{(x_i - x_{\mathrm{core}})^2 + (y_i - y_{\mathrm{core}})^2}}{10\mathrm{m}}}\right) \tag{6.5}$$

where $q_i$ are the charges measured in the individual IceTop tanks, and the distances from the reconstructed core position are $r_i = \sqrt{(x_i - x_{\mathrm{core}})^2 + (y_i - y_{\mathrm{core}})^2}$ with $i = 1 \ldots n$, where $n$ is the total number of pulses. The Charge-Distance is a versatile quantity that can be calculated for both HLC and SLC hits (Section 2.1). However, the main differences between hadron and gamma-ray air showers lie in the muon content and how they affect the footprint. Figure 6.7b shows the HLC (Figure 6.7a) and SLC (Figure 6.7b) hits for a measured air-shower event. The HLC hits have a more compact distri-

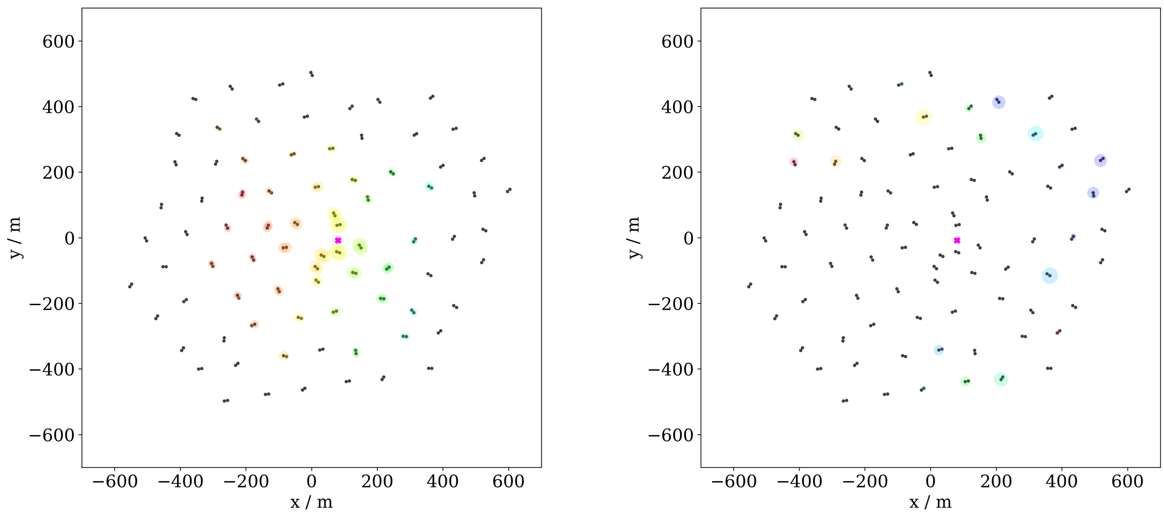

(a) The HLC hits for a measured air-shower event.

(b) The SLC hits for the same measured air-shower event.

Figure 6.7.: Surface signal for a measured air-shower event showing the two types of pulses: HLC and SLC. The black dots indicate the position of the DOMs. The magenta cross indicates the position of the reconstructed core, and the colored circles indicate the pulses. The time follows the rainbow colors from early (red) to late (blue). Plot made with the Event viewer, Appendix A.

bution around the reconstructed core (magenta cross), whereas the SLC hits show a less compact distribution. Hence, SLC hits are best for this purpose as they often indicate single muons. However, SLC hits must undergo a cleaning process, similar to the in-ice pulses, before being used for this analysis. For this purpose, the Laputop3s3s reconstruction method, described in Section 4.3.2, is used for the selection of good pulses. Specifically, the selection process of the SLC hits is performed via two cleaning processes. The first one is done via a time-window selection from 0 to 600 ns after the Laputop3s3s core reconstructed time. This time window is found to be adequate for this analysis since it excludes the majority of the early pulses and does not include the later ones, which include unwanted background noise. The second cleaning is based on the charge: $q_i > 0.5$ VEM. Since SLC hits are expected to be generated primarily by muons, applying a charge threshold effectively acts as a muon selection criterion. This threshold filters out pulses that are unlikely to originate from muons, ensuring a more accurate selection.

Figure 6.8 shows normalized histograms of the Charge-Distance for different datasets in the energy range from 5.0 to 7.0 in $\log_{10}(\mathrm{E/GeV})$. Gamma-ray simulations (indigo) peak at a value smaller than proton simulations (red) or measured IceTop data (black). The different distributions between the gamma-ray simulation dataset and the other datasets prove that this quantity can be used to further improve the gamma-hadron separation. In the Appendix B.1, Figure B.1 also shows the CD values for Sibyll 2.1 proton and iron simulations, which are similar to Sibyll 2.3d results.

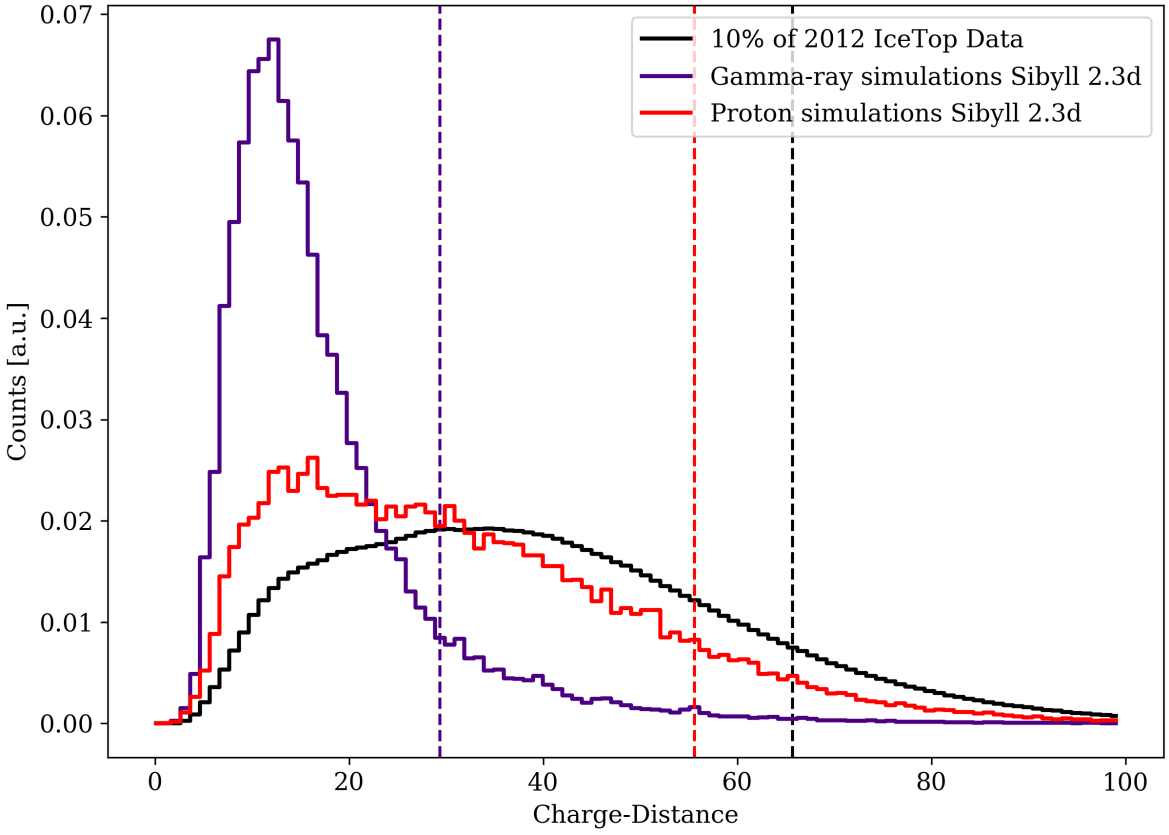

Figure 6.8.: Icetop Charge-Distance for different datasets in the energy range from 5.0 to 7.0 in $\log_{10}(\mathrm{E/GeV})$. The vertical lines indicate the position of the 85th percentile of the histogram.

Figure 6.9 shows the Charge-Distance values calculated for gamma-ray simulations for 4 different $\log_{10}(\mathrm{S}_{125}/\mathrm{VEM})$ ranges. This shows that the Charge-Distance values are energy dependent, meaning that the general shape of the distributions and the positions of the peaks shift towards larger values, the higher the energy. For this reason, a cut value for the separation based on this quantity must also be a function of energy.

To set a cut on the CD for suppression of hadronic showers, a similar procedure as performed in Section 6.2.1 for the in-ice pulses is used. The Li & Ma significance is utilized again for finding the optimal value. The cut has been chosen with two main goals in mind: minimizing the background and maximizing the Li & Ma significance.

The events used at this stage are the ones that pass the quality cuts of Section 4.4, and in-ice selection cut of Section 6.2.1, i.e., that do not have a high-energy muon detected. These events are now further selected based on their Charge-Distance value. Different cut values were sampled based on the passing fraction of gamma rays. Figure 6.10 shows

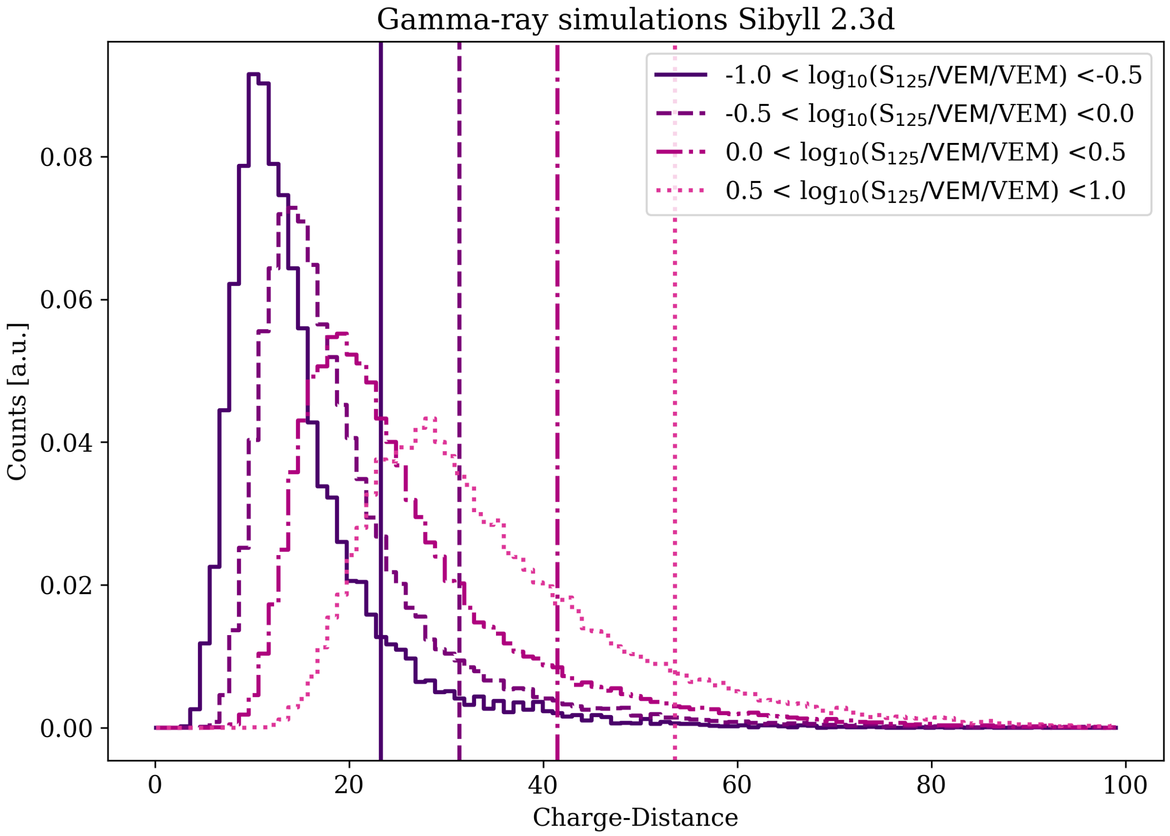

Figure 6.9.: IceTop Charge-Distance values calculated for gamma-ray simulations for 4 different $\log_{10}(S_{125}/\text{VEM})$ ranges. The Charge-Distance values are energy-dependent. The general shape of the distributions and the positions of the peak shift towards larger values, the higher the energy. The vertical lines indicate the position of the 85th percentile of each histogram.

the results of this analysis for three different LHAASO-like mock sources. The x-axis shows the fraction of gamma-ray simulations that are retained via the CD cut, and the y-axis shows the maximum significance that can be reached via the cut. The significance is increasing with the percentage of passing gamma-ray events and has a broader maximum around 85%. Hence, this value is chosen, implying that a larger fraction of gamma-ray events pass the cut.

As already discussed and shown in Figure 6.9, the CD values are not constant over energy. Consequently, the 85% CD cut value changes as a function of energy. Figure 6.11 shows the corresponding CD-cut values for each bin with blue dots. Since these values show a linear correlation, they can be fitted with a linear function, which is used for the gamma-ray selection. The red line in the plots shows the result of the fit. The

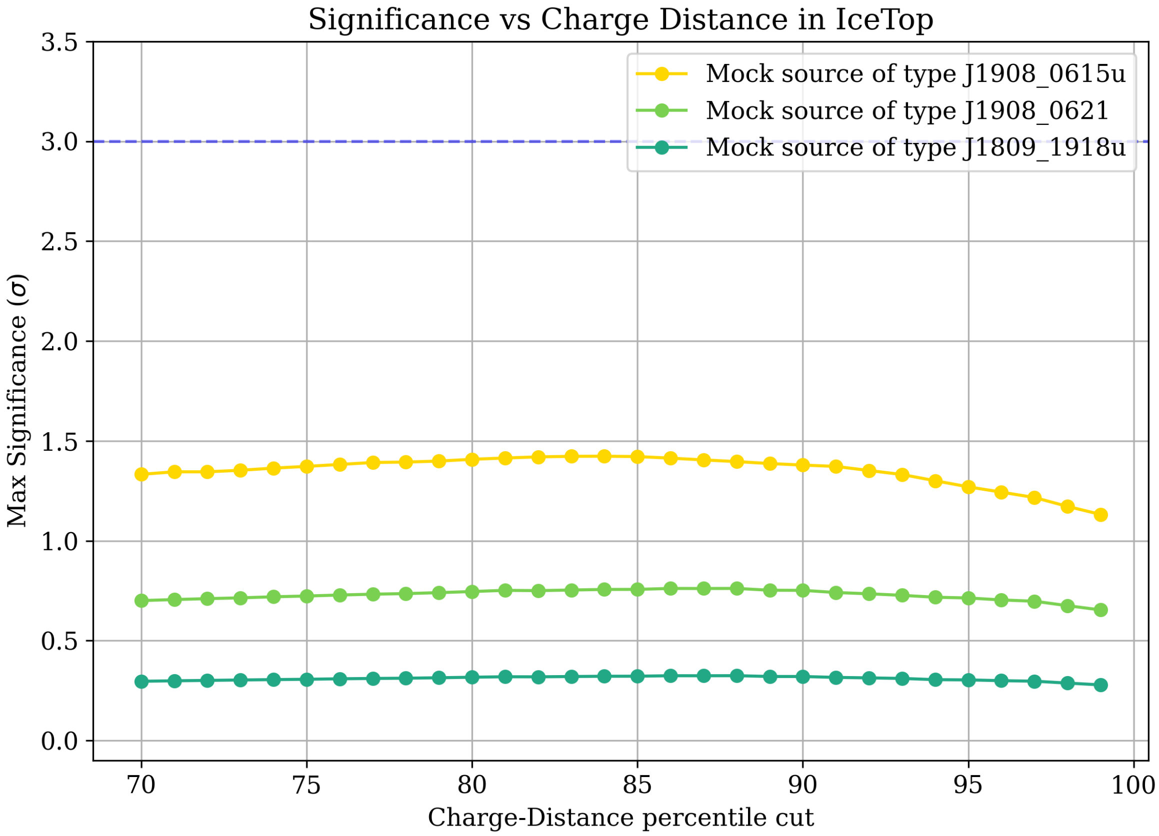

Figure 6.10.: The Li& Ma significance achievable with one year of IceCube data as a function of different Charge-Distance cut values for two different LHAASO-like mock sources. The x-axis shows the fraction of gamma-ray simulations that are retained (percentile) via the CD cut, and the y-axis shows the maximum significance that can be reached via the cut. The energy range considered is $5.0 < \log_{10}(\mathrm{E/GeV}) < 7.0$.

advantage of this fit is that it allows for an analytic gamma-ray selection based on the CD-cut values as a function of $\log_{10}(\mathrm{S}_{125}/\mathrm{VEM})$:

$$\mathrm{CD}_{\mathrm{cut}} = 21.7(1.1) \cdot \log_{10}(\mathrm{S}_{125}/\mathrm{VEM}) + 35.1(0.6) \tag{6.6}$$

The final gamma-hadron separation will combine the in-ice selection and the CD-cut as explained in the following section. The background suppression achievable only using the CD is shown in Figure B.2 in Appendix B.2. The maximum separation achievable with the CD-cut alone is about 70% at 1 PeV.

## 6.3. Gamma-Hadron Separation

Combining the in-ice selection (Section 6.2.1) and the surface selection (Section 6.2.2), the total gamma-hadron separation can be quantified. Figure 6.12 presents the passing

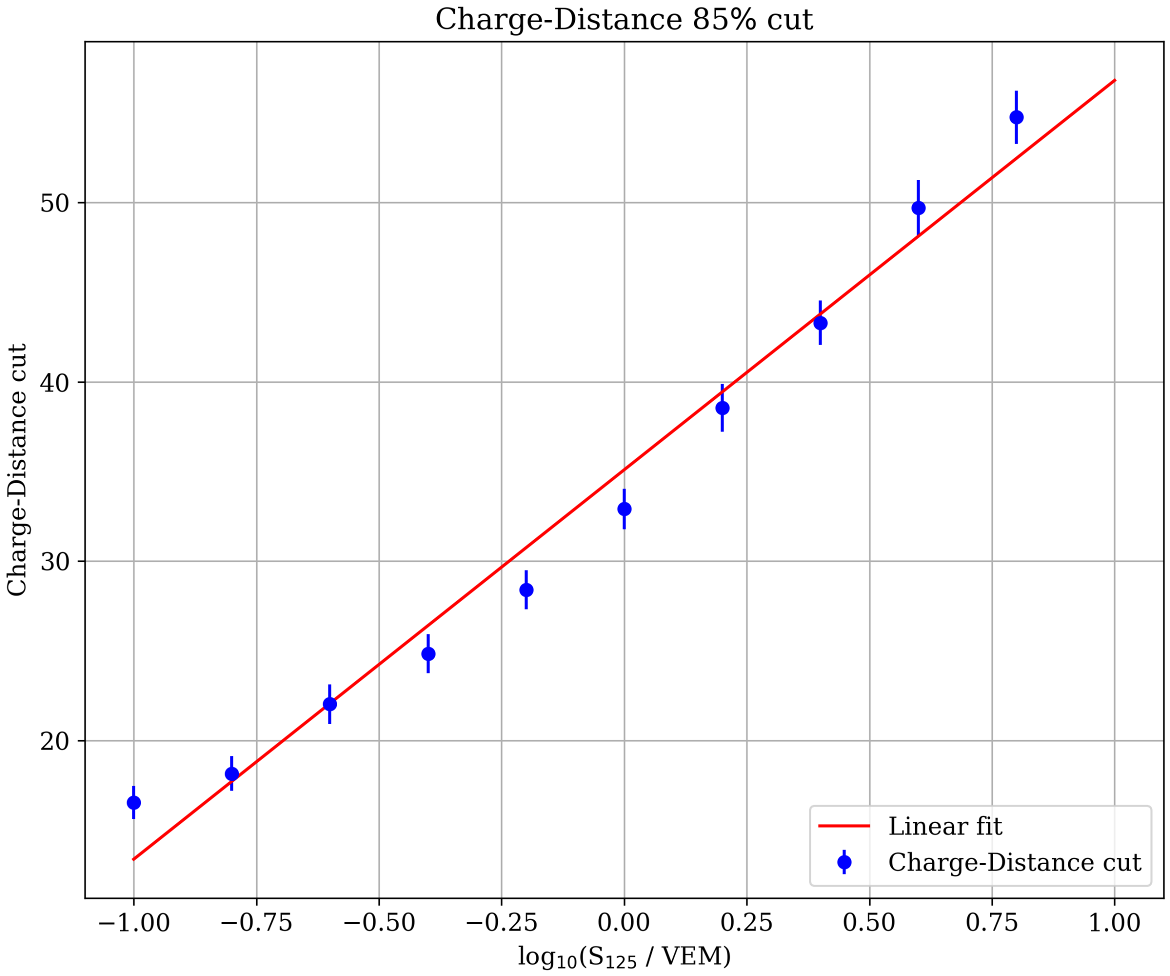

Figure 6.11.: The 85% Charge-Distance cut parametrization as a function of $\log_{10}(S_{125}/\mathrm{VEM})$. The red line shows the result of the linear fit of the 85% cut values, with slope $m = 21.7(1.1)$ and intercept $q = 35.1(0.6)$.

fraction of surviving events as a function of energy. This fraction is defined as the ratio of events identified as gamma candidates to the total number of events that satisfy the quality cuts and are contained in the in-ice detector. The solid line represents the results of this analysis, while the dashed line corresponds to the previous search for gamma rays with IceCube [42]. The gamma-ray fraction is shown in magenta, and the data fraction is shown in black. The earlier analysis covered an energy range of $5.7 < \log_{10}(\mathrm{E\,/\,GeV}) < 8.0$, whereas this study can extend the range to lower energies of $5.0 < \log_{10}(\mathrm{E\,/\,GeV}) < 7.0$. Within the overlap region, a clear improvement in gamma-hadron separation is observed, with the performance steadily improving as the energy increases. Performing better than $10^{-3}$ background suppression at energies above 1 PeV.

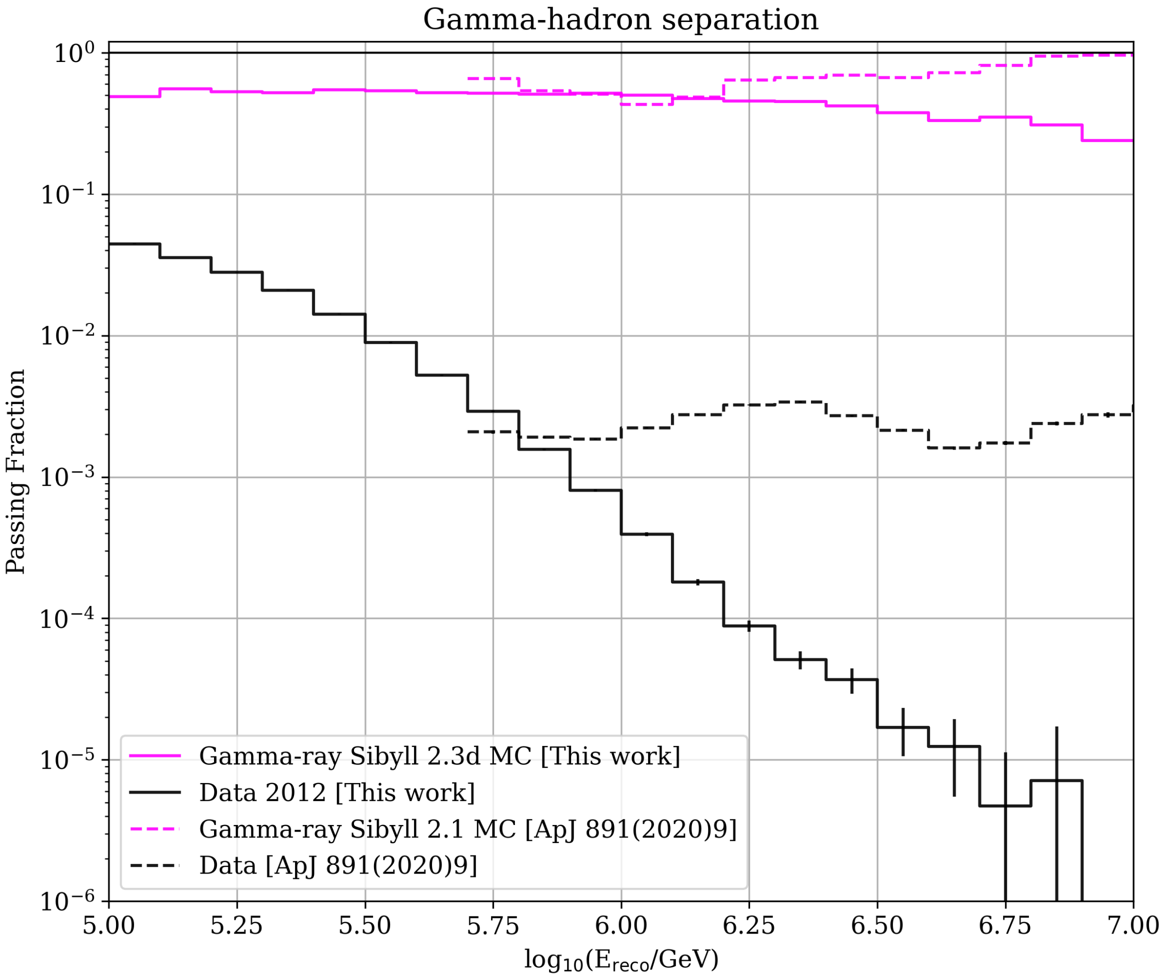

Figure 6.12.: Passing fraction of gamma-ray candidate events as a function of energy. The solid line represents the results of this work, while the dashed line corresponds to a previous IceCube analysis [42]. A clear improvement in gamma-hadron separation is observed in the overlap region, with performance increasing towards higher energies.

### 6.3.1. Optimization of energy range for gamma-ray search

Once the gamma-ray selection criteria are fixed, it is necessary to define the optimal energy range for the search of gamma-ray sources.

For this purpose, the Li & Ma significance is used once again. The number of signal events and the number of background events are calculated for different energy intervals with a 0.1 step on the $\log_{10}(\mathrm{E/GeV})$ scale. The number of signal events is obtained by adding all events in each energy bin from $\mathrm{E_{min}}$ to $\mathrm{E_{max}} = \infty$:

$$\mathrm{N} = \sum_{E_{\mathrm{min}}}^{E_{\mathrm{max}}=\infty} N(E) \tag{6.7}$$

where $N(E)$ represents the number of events after selection cuts. The same approach as explained in Section 6.1.2 is followed, the only difference being that the number of signal events is now given for an interval $E > E_{\text{min}}$ and not for a single energy bin. The background events and the number of signal events are now estimated after the gamma-ray selection via Equation 6.7. Figure 6.13a shows the result of this operation. It is worth noticing that the separation has now drastically diminished the number of background events, especially at higher energies. The expected number of detectable gamma-ray events passing the selection cuts exceeds the number of background events at energies above 0.4 to 1 PeV, depending on the mock source. This may enable the observation of potential gamma-ray sources.

The significance of each source for all energy ranges can now be estimated to quantify the discovery potential of possible gamma-ray sources. Thus, the number of signal and background events from Figure 6.13a are taken and the Li & Ma significance is calculated with $\mathrm{N_{on}} = \mathrm{N_{sig}} + \mathrm{N_{bg}}$ and $\mathrm{N_{off}} = \mathrm{N_{bg}}$. Figure 6.13b shows the significance for all energy bins, where the starting energy is shown on the x-axis and the end energy is assumed to be infinity. The maximum significance differs for each source. The most intense source reaches the maximum significance of $2.8\sigma$ for a starting energy of about 500 TeV.

### 6.3.2. Impacts of the selection cuts on air-shower reconstruction

Sections 4.5.2 and 4.5.3 explained how the angular resolution and the energy estimation have been calculated, applying exclusively the quality cuts (Section 4.4). However, for a future sky search for gamma-ray sources, both the quality cuts (Section 4.4) and the selection cuts (Section 6.2) should be applied. Here, the effects of the selection cuts on the angular resolution and energy reconstruction are analyzed.

Figure 6.14 shows the angular resolution as a function of the simulated energy (left-hand side) and the energy proxy (right-hand side). Both plots show 2-D histograms of simulated air showers weighted with a spectral index of $\gamma = 3$. The gray "x" indicates the 68% quantile before the gamma-ray selection, and the black dots the 68% quantile after the selection. No major changes are seen in the 68% quintile for the angular resolution since most of the gamma-ray events are kept by the selection cuts.

In Figure 6.15, the left-hand side plot shows the true energy of the simulation as a function of the energy proxy in a 2-D histogram weighted with a spectral index of $\gamma = 3$. For each bin in $\log_{10}(\mathrm{S_{125}}/\mathrm{VEM})$, a Gaussian is fitted with the mean $\pm 1\sigma$ shown. These are fitted with a linear function in the range $-1.0 < \log_{10}(\mathrm{S_{125}}/\mathrm{VEM}) < 1.0$ and the fit is plotted as a red line. The fit results in a slope $m = 1.005(0.006)$ and offset $q = 6.034(0.003)$. The linear function is used for the reconstructed energy calculation.

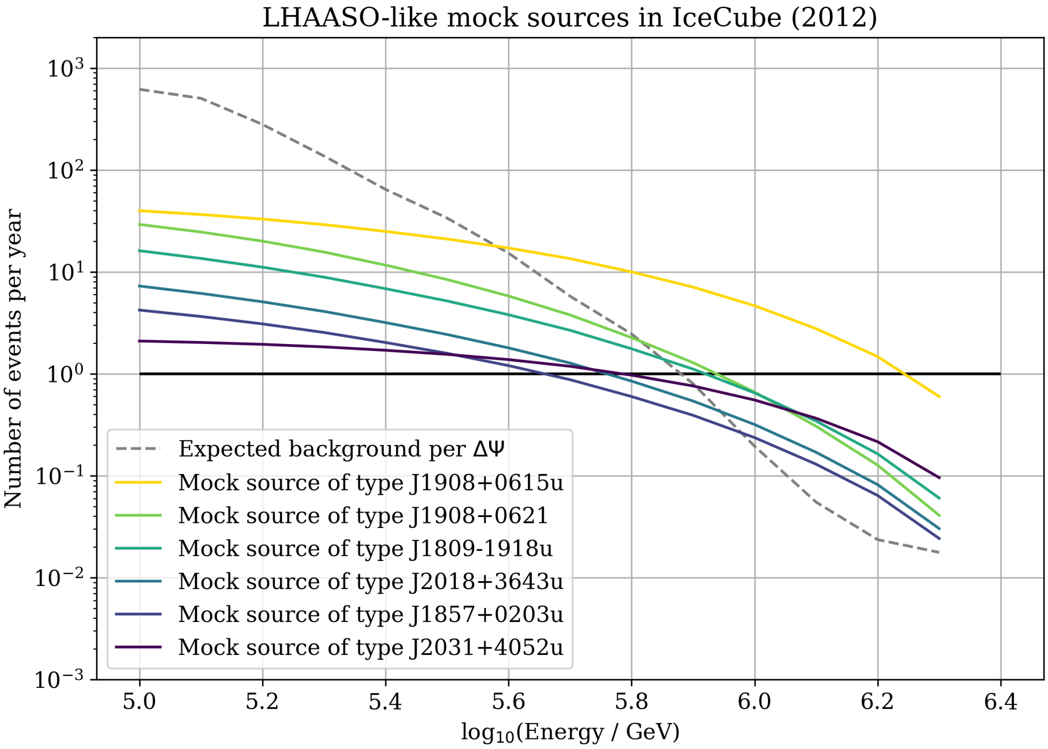

(a) Number of estimated events per energy range after the gamma-ray selection cuts. The dashed line shows the expected background per angular resolution.

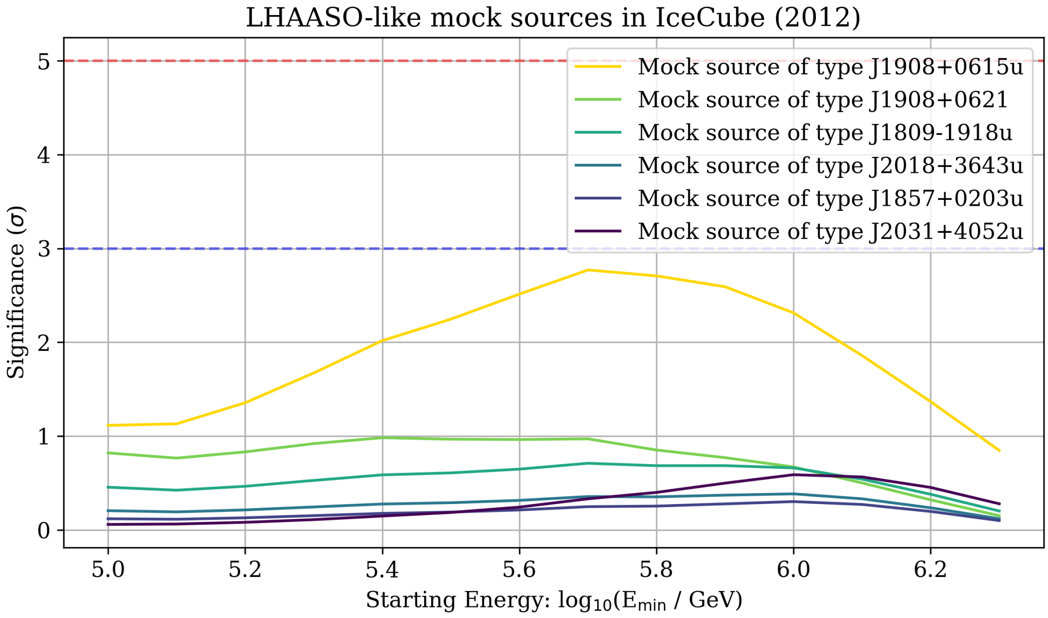

(b) Corresponding significance of all mock sources depending on the chosen minimum energy cut $E_{\text{min}}$, the maximum significance reached is $2.8\sigma$.

Figure 6.13.: The expected number of events within the angular resolution and the corresponding significance, estimated from the 2012 IceCube data.

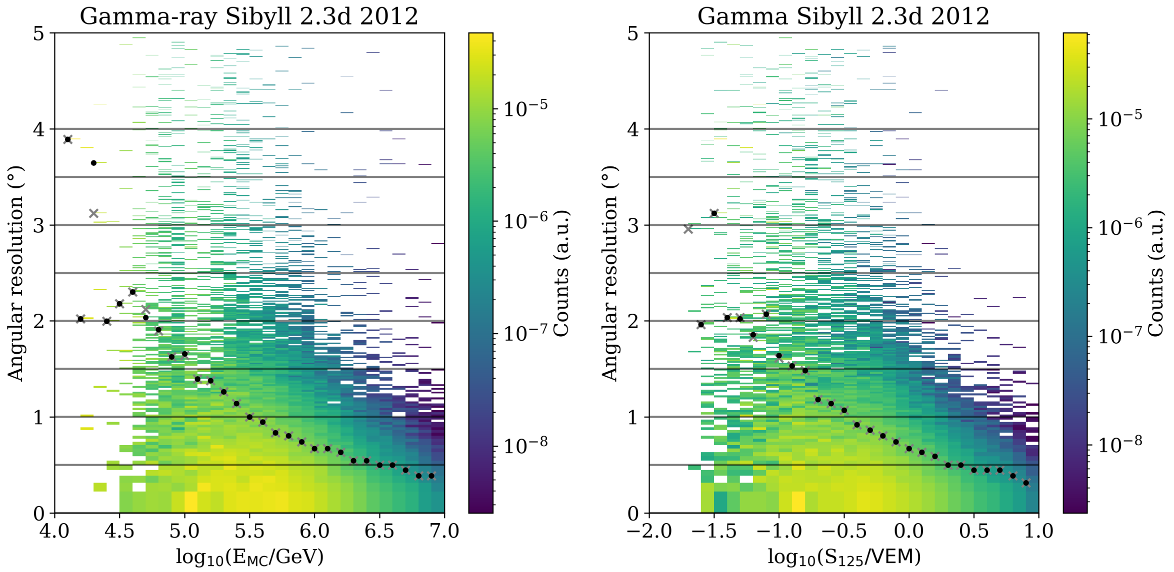

Figure 6.14.: The angular resolution as a function of the simulated energy (left-hand side) and the energy proxy (right-hand side). Both plots are 2-D histograms of simulated air showers weighted with a spectral index of $\gamma = 3$. The black dots indicate the position of the 68% quantile.

In the right-hand side plot, the difference between the reconstructed and the simulated energy is plotted. For each bin in $\log_{10}(S_{125}/\mathrm{VEM})$, a Gaussian is fitted, the mean and the $\pm 1\sigma$ region are shown.

## 6.4. Sensitivity estimation

This section studies the sensitivity that IceCube can achieve with the new method of gamma-hadron separation. In particular, the lowest source flux that gives a $2\sigma$ significance is calculated and set for multiple energy ranges and spectral indices for the year 2012.

The form of the differential flux of a gamma-ray source is the same as the one for LHAASO sources of Equation 6.4. Thus, the flux has the flux normalization constant $N_0$ with units of photons $\cdot\,\mathrm{cm}^{-2}\cdot\mathrm{s}^{-1}\cdot\mathrm{TeV}^{-1}$ and a reference energy $E_0 = 50$ TeV. Different values of $N_0$ are tested, and the smallest value that gives the $2\sigma$ sensitivity with one year of observation time is selected. The spectral index $\gamma$ of the hypothetical source is fixed, and the calculation is repeated for different values of $\gamma$. The number of signal events is obtained via the flux integration over an energy range $E_{\mathrm{min}}$ to $E_{\mathrm{max}}$ after applying the trigger and reconstruction efficiencies and the loss of events caused by the gamma-ray selection. The starting energy is shown by the value on the x-axis in Figure 6.16b, and

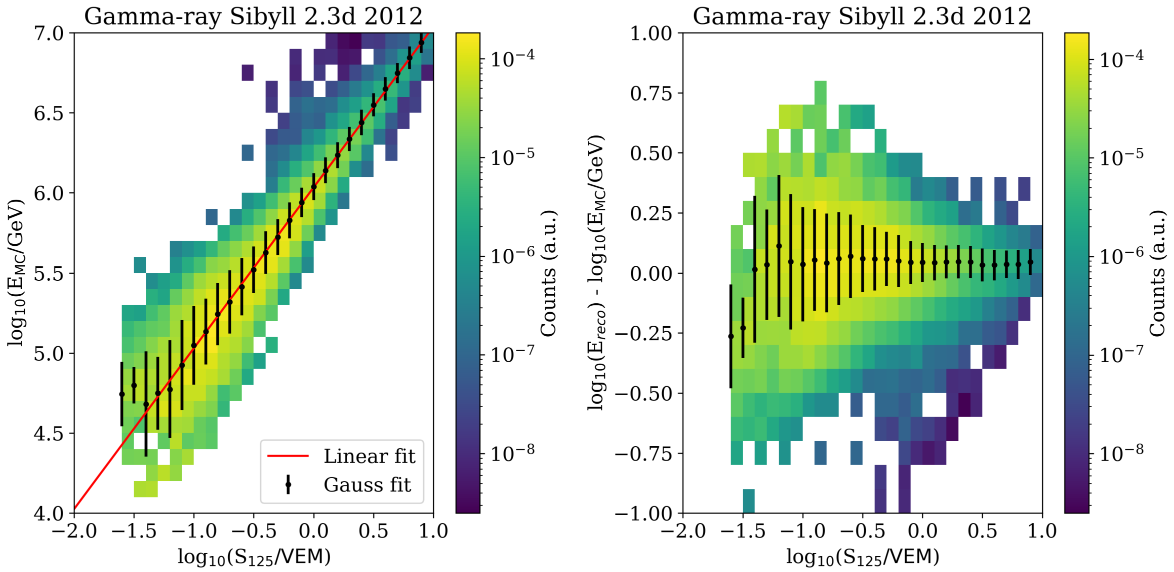

Figure 6.15.: The left-hand side plot shows the true energy of the air-shower simulation as a function of the energy proxy in a 2-D histogram weighted with a spectral index of $\gamma = 3$. The fit results in a slope $m = 1.005(0.006)$ and offset $q = 6.034(0.003)$. The right-hand side plot shows the difference between the reconstructed and the simulated energy. For each bin in $\log_{10}(S_{125}/\mathrm{VEM})$, a Gaussian fit is performed, the black dots are the mean and the bars the $\pm 1\sigma$ region. The red line is the fit of the mean values.

the maximum energy is assumed to always be infinity. Thus, the number of photons $N$ per $t = 365$ days in a circular area $A$ with a radius of 500 m is:

$$\mathrm{N} = \int_{E_{\min}}^{E_{\max}=\infty} \phi(E)\, dE, \tag{6.8}$$

with $\phi(E) = N_0 \cdot A \cdot t \cdot E^{-\gamma}$ Integrating over the entire energy, the total number of events N is obtained:

$$\mathrm{N} = N_0 \cdot A \cdot t \cdot \frac{E_0^{-\gamma}}{1-\gamma} \left( E_{\max}^{1-\gamma} - E_{\min}^{1-\gamma} \right) \tag{6.9}$$

$$= N_0 \cdot A \cdot t \cdot \frac{E_0^{-\gamma}}{\gamma - 1} E_{\min}^{1-\gamma}, \tag{6.10}$$

given that $E_{\max} = \infty$. The integral can now be performed with different values of $N_0$, and the number of signal events can be calculated for all energy ranges.

The number of background events is estimated again via 10% of the measured air-shower data for the year 2012. The same process that was done in Equation 6.3 is here repeated. A zenith range $5^\circ < \theta < 10^\circ$ has been used for calculating the total number of events, and the density per solid angle is estimated. Hence, the background flux per steradian is known, and the number of background events based on the opening angle is calculated. Because the angular resolution improves with energy, the opening angle values also change accordingly as a function of energy.

Finally, the Li & Ma significance can be estimated given the number of background events, and the smallest value of $N_0$ which exceeds the $2\sigma$ significance is plotted in Figure 6.16a. This process is repeated for all energy intervals and spectral indices $\gamma$. The $N_0$ values can be found in Appendix B, in Table B.1.

The differential flux $E^2\Phi(E) = E^2 \frac{dN}{dE\, dA\, ds}$ is also calculated given the corresponding $N_0$ and shown in Figure 6.16b.

## 6.5. Rate of gamma-ray candidates

This section discusses the rate of gamma-ray candidates and compares it to the one observed by LHAASO for the Galactic Plane [48]. The rate is calculated via the measured data. Specifically, a 20° region around the zenith of the sky is observed and the corresponding LHAASO galactic plane flux is estimated for the same solid angle region. LHAASO observed different intensities for the diffuse flux from the Galactic Plane (GP), a higher flux closer to the geometric center, and a less intense one further away from it. As previously done, the LHAASO galactic plane fluxes have to be adjusted for the trigger and reconstruction efficiencies, and the loss of events because of the gamma-ray selection. After the corrections are applied, the number of events expected for one year of IceCube is calculated and compared to the diffuse flux in the zenith region for the GP flux observed by LHAASO. Figure 6.17 shows in blue and red the inner and outer Galactic plane fluxes as a function of energy. The values above 1 PeV have been obtained by extrapolating the observed LHAASO flux. The IceCube gamma-ray candidates, passing the gamma-hadron cuts, show that in one year, the number of gamma-ray candidates observed by IceCube is generally higher than the number predicted by LHAASO. Furthermore, it is noticeable how the difference shrinks at higher energies, as expected by the enhanced gamma-hadron separation. Furthermore, the 20° zenith region of the sky, which is observed by IceTop and taken into account in this example, is an off-plane region, meaning that it cannot be directly compared to the LHAASO measurement but still provides realistic reference values. In conclusion, the rate of gamma rays is larger than expected. Hence, the gamma-ray candidate set still contains an important presence of hadronic air showers.

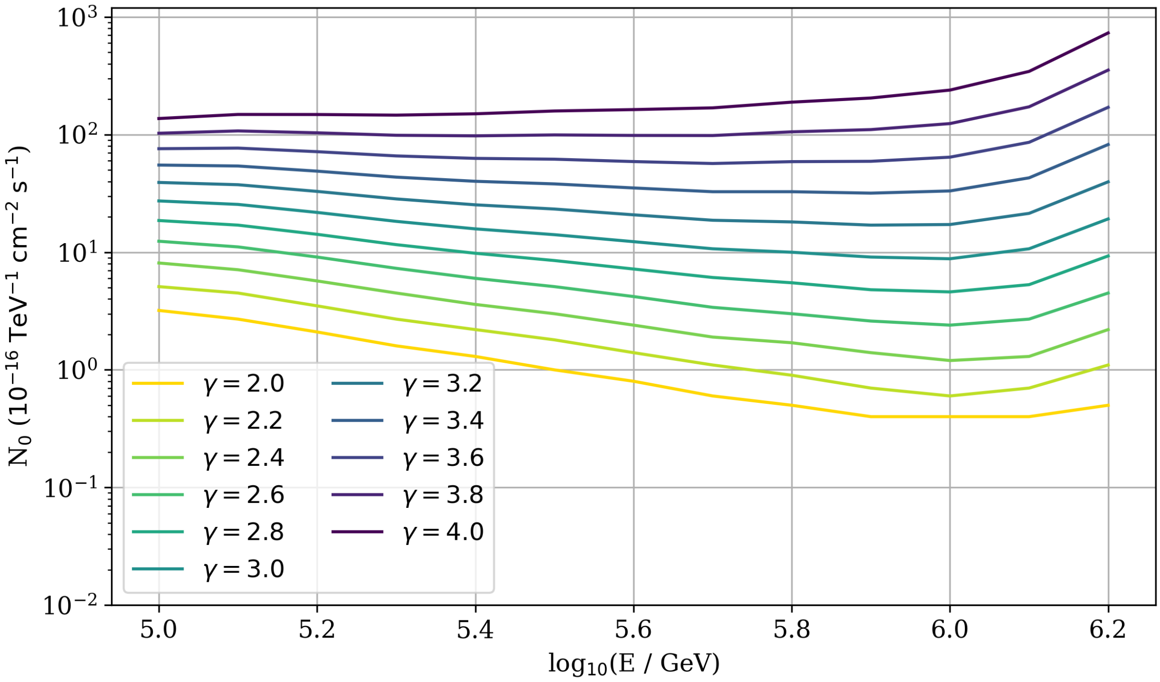

(a) The $N_0$ values of the flux that would give a $2\sigma$ sensitivity as a function of energy for different assumptions of the spectral index $\gamma$.

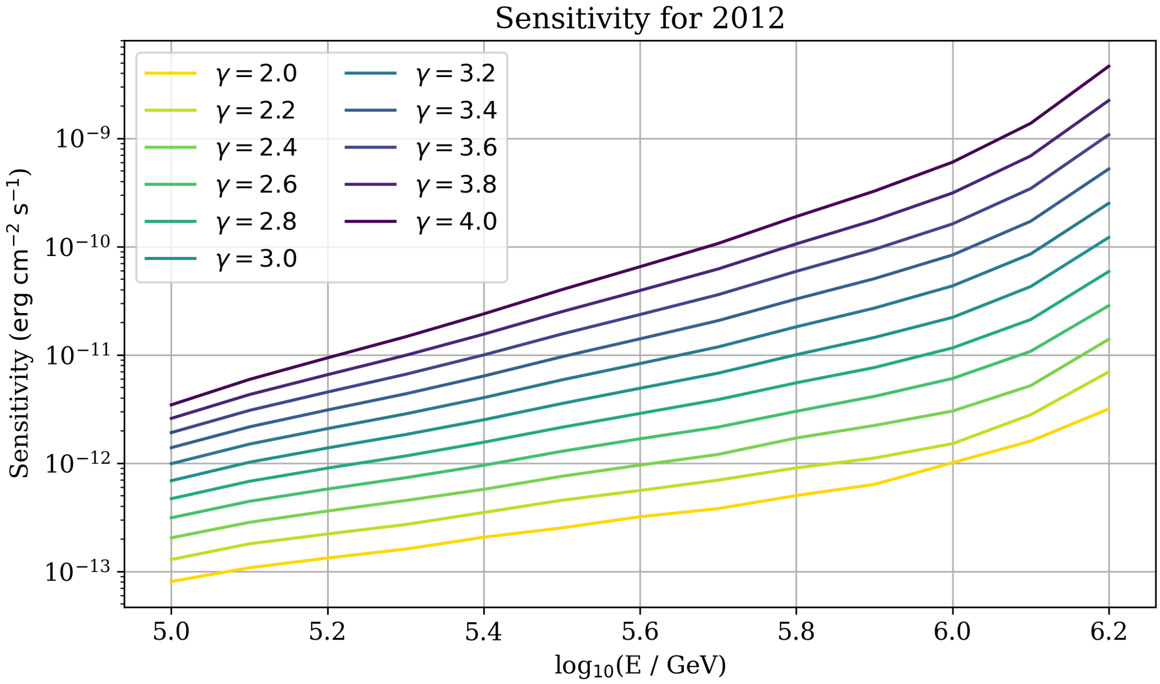

(b) The flux that would give a $2\sigma$ sensitivity asa function of energy for different assumptions of the spectral index $\gamma$.

Figure 6.16.: Sensitivity estimation for a flux that would give a $2\sigma$ sensitivity observation.

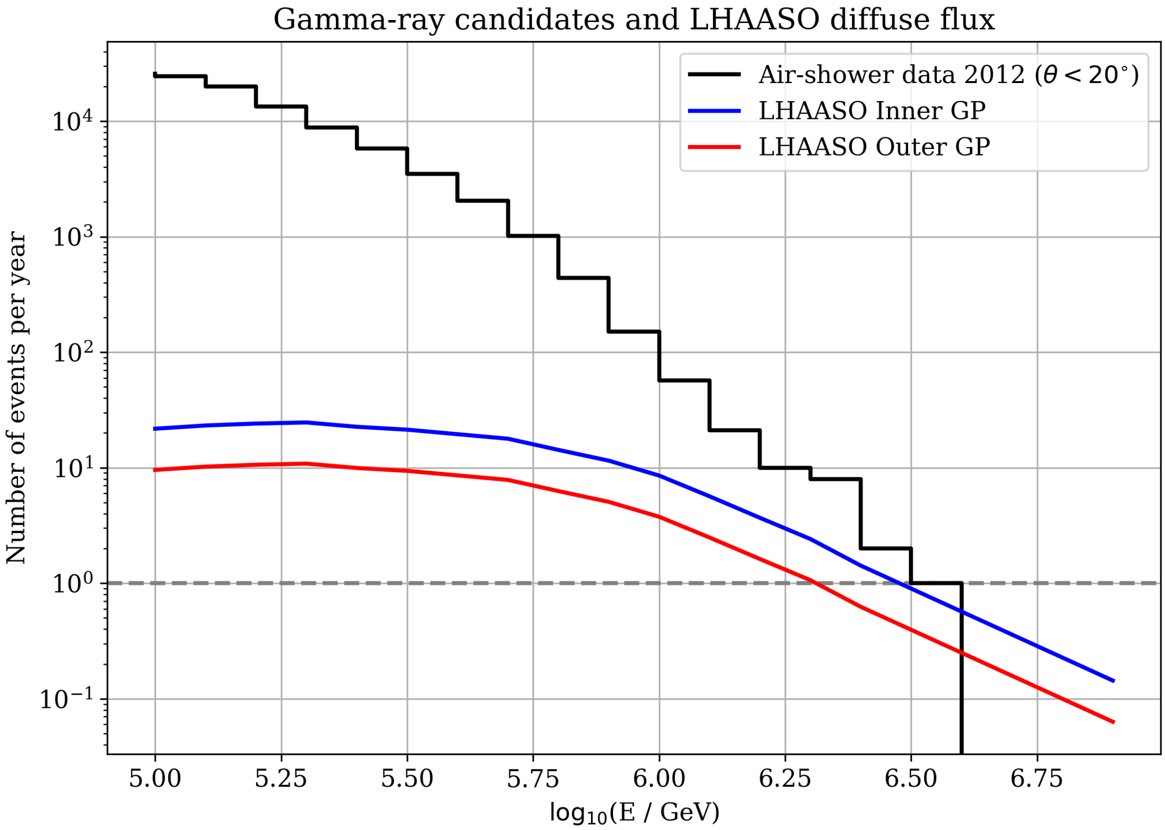

Figure 6.17.: Rate of IceCube gamma-ray candidates, i.e., air-showers events passing the gamma-hadron separation cuts, for a 20° region around the zenith. The estimated LHAASO inner and outer Galactic Plane flux of gamma-rays for the same solid angle, time, and area is shown for comparison.

## 6.6. Effective area of IceCube for gamma-rays

The Effective Area $A_{\text{eff}}$ is a useful quantity that can be used for the estimation of the sensitivity of the detector to incoming gamma rays and used to convert the number of detected events into a physical flux from a source or a diffuse flux. It has units of an area but also accounts for detector efficiency, energy dependence, directional response, and the pass fraction of gamma rays through the gamma-hadron selection cuts. Thus, it varies significantly with the energy and direction of the incoming events. For the IceTop detector array, the effective area can be calculated using the detector response of gamma-ray MC simulations (Section 3.1.2) and IceCube's `simweights` tool [74].

The calculation of a flux from the number of measured events $N(E)$ can be performed as follows:

$$\Phi(E) = \frac{N(E)}{A_{\text{eff}}(E) \cdot \Delta E \cdot \Delta t} \tag{6.11}$$

where $\Phi(E)$ is the flux, $\Delta E$ the energy step size, and $\Delta t$ the time interval.

The effective area can be calculated for multiple scenarios, e.g., the full set of simulations without any cuts, the set with only the quality cuts applied, or the one with quality cuts and gamma-ray selection applied. Each set generates different values of the effective area that can be used for the corresponding analysis. Here, the effective area with quality cuts and gamma-ray selection is discussed. The other plots of the effective areas can be found in the Appendix B.4.

Figure 6.18 shows the values for the effective area for multiple zenith ranges. Each zenith range is fitted with a third-grade polynomial:

$$p(E) = x_0 + x_1 E + x_2 E^2 + x_3 E^3. \tag{6.12}$$

The fit values of the polynomial can be found in the Table B.2 in the Appendix B.4.

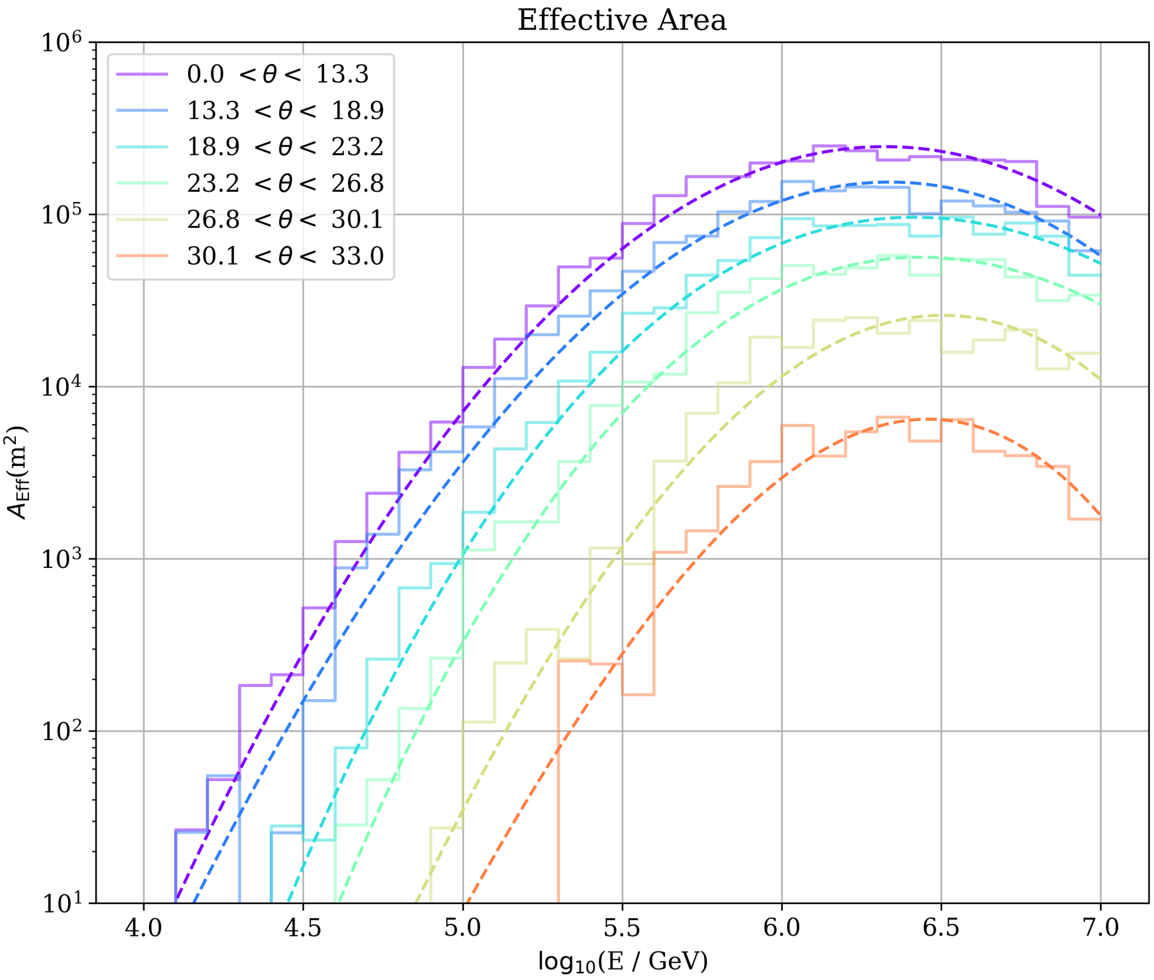

Figure 6.18.: Effective area after quality cuts and gamma-ray selection for different zenith bins.

As previously discussed, the effective area depends on the energy and the zenith angle. Its maximum values are reached in the energy range $6.0 < \log_{10}(E/\mathrm{GeV}) < 6.5$ in all zenith intervals. At lower energies, the effective area is primarily reduced due to trigger and reconstruction inefficiencies, whereas at higher energies, the decrease is due to the gamma-ray selection. However, the gamma-ray flux is also expected to decrease at energies above 2 PeV, making this a relatively minor limitation. The decrease in the effective area with increasing zenith angle is mainly due to the in-ice containment requirement.

Finally, a comparison of the effective area with the actual geometrical area of the detector can be performed. The ratio of the two provides a benchmark for evaluating the performance of this and future analyses.

For a flat detector with a geometric surface area $A_{\mathrm{geo}}$, the projected area at a zenith angle $\theta$ is:

$$A(\theta) = A_{\mathrm{geo}} \cos\theta \tag{6.13}$$

Assuming an isotropic flux per solid angle, the average projected area over a zenith range $\theta_1 < \theta < \theta_2$ is:

$$\langle A_{\mathrm{geo}} \rangle = \frac{1}{\Delta\Omega} \int_{\theta_1}^{\theta_2} \int_0^{2\pi} A_{\mathrm{geo}} \cos\theta \sin\theta \, d\phi \, d\theta, \tag{6.14}$$

where $\Delta\Omega$ is the solid angle corresponding to the zenith range:

$$\Delta\Omega = 2\pi(\cos\theta_1 - \cos\theta_2).$$

Solving the integral:

$$\langle A_{\mathrm{geo}} \rangle = \frac{A_{\mathrm{geo}}}{\Delta\Omega} \cdot 2\pi \int_{\theta_1}^{\theta_2} \cos\theta \sin\theta \, d\theta = \frac{A_{\mathrm{geo}}}{\cos\theta_1 - \cos\theta_2} \cdot \left[ \frac{1}{2} \sin^2\theta \right]_{\theta_1}^{\theta_2} \tag{6.15}$$

Given that in the first zenith interval $\theta_1 = 0°$ the integral simplifies to:

$$\langle A_{\mathrm{geo}} \rangle = \frac{1}{2} \cdot \frac{A_{\mathrm{geo}}}{1 - \cos\theta_2} \cdot \sin^2\theta_2 = 0.775\,\mathrm{km}^2 \tag{6.16}$$

with $\theta_2 = 13.3°$.

The maximum value of the effective area in this zenith range is $A_{\mathrm{eff}} = 0.250\,\mathrm{km}^2$ at about 1.5 PeV. Hence, the ratio between the maximum effective area and the average geometric area is $\frac{A_{\mathrm{eff}}^{\mathrm{max}}}{\langle A_{\mathrm{geo}} \rangle} = 0.332$.

In addition, improvements in reconstruction efficiency or a higher gamma-ray simulation retention could significantly increase the effective area, bringing it closer to the geometric value of $A_{\mathrm{geo}}$.

## 6.7. Conclusions and outlook on the gamma-hadron separation

This chapter has shown two main improvements to IceCube's prior gamma-ray analysis. The first achievement is the extension of the analysis to lower energies, and the second is the improvement in the gamma-hadron separation, especially in the PeV energy range. This enables the possibility of discovering PeV gamma-ray sources, given that PeV gamma-ray sources, such as those observed by LHAASO, were in the IceTop field of view.

This analysis has set the basis for the gamma-ray point source search and can be used for finding a set of potential gamma-ray candidates in the entire 2012 dataset. However, further steps are needed for an actual search for gamma-ray sources with IceCube. For this purpose, an IceCube software called `csky` can and has been utilized. It is an established software mainly used for neutrino source searches, but easily adaptable for gamma-ray analysis. This software provides a reliable and tested approach for analyzing the 2012 dataset and is easily extendable for all years. Appendix C summarizes this software and how the analysis has been set up and made ready for the unblinding process.

Despite tuning this analysis for the gamma-ray point source search, the same method of gamma-hadron separation can be used for studying the rate of gamma-ray candidates. The rate of the gamma-ray candidates coming from a 20° zenith range has been compared to the diffuse flux of the inner and outer galactic planes that LHAASO measured. The previous analysis [42] has set an upper limit on the gamma-ray emission from the galactic plane. However, the new method of gamma-hadron separation introduced in this work can improve that limit and extend it to lower energies.

Finally, the effective area was calculated for different zenith ranges, and a third-degree polynomial fit was performed for each range.

Before proceeding with the gamma-ray point source search, this analysis could benefit from a few minor improvements. For instance, the time window for selecting in-ice and surface SLC pulses could be improved. The adjustment may help include more early and/or late pulses, potentially enhancing gamma-hadron separation.

Additionally, the current method of counting in-ice layers could be refined by considering a cylindrical region around the shower axis instead and setting a minimum number of localized pulses above a threshold. This may further reduce the contamination of background noise.

Finally, it is important to note that the studies on trigger efficiency, reconstruction quality cuts, and variables such as Charge–Distance may differ over time due to snow accumulation on top of the IceTop tanks. For this reason, the analysis should be repeated for each year separately, and the evolution over time should be monitored.

# Conclusion

IceCube is a unique instrument for the detection of neutrinos and cosmic rays, but also for searching for gamma-ray candidates. This analysis has combined IceTop, the surface detector, and the in-ice array to achieve two major results. First, the energy range of the gamma-ray analysis was extended by developing a low-energy reconstruction method that reconstructed gamma-ray events with energies lower than 100 TeV. Secondly, the gamma-hadron separation was improved over the full energy range, particularly at PeV energies, where the background suppression by a factor of $10^{-3}$ was achieved.

Laying the groundwork for these results, the first step included the development of a scalable framework that provided CORSIKA and detector response simulations. This framework has been successfully implemented and validated for the run of the year 2012, and the setup was also made available for future simulation production, paving the way for upcoming studies.

The newly developed reconstruction method enabled the study of low-energy gamma-ray events, where the flux is expected to be significantly higher than in the high-energy regime. This reconstruction, named "Laputop3s3s", proved to be reliable and comparable to the standard one in the overlapping energy range with $10\times$ higher reconstruction efficiency at 100 TeV.

A successful calibration of Soft Local Coincidence (SLC) pulses, a single pulse from a tank of a station, has been a major technical achievement, essential for this and future work. SLC pulses of events recorded with the 3-station trigger, especially relevant for the low-energy events, were calibrated and are now consistent with those recorded with the 5-station trigger. This enabled the use of SLC pulses for the gamma-hadron separation. Thus, a new heuristic quantity was defined, named Charge-Distance, tuned as a function of energy to retain $85\%$ of the gamma signal and to be able to remove up to $70\%$ of hadron-generated air showers at 1 PeV.

In combination with the Charge-Distance, signal information from the in-ice array has been used for the gamma-hadron separation study. The signal was cleaned to remove the background in order to isolate the high-energy muons. As selection criteria, only the information from the first five layers was used for a binary *yes-no* classification.

The obtained gamma-hadron separation enhanced the results achieved by the previous analysis by up to one order of magnitude for events in the near-PeV energy range. Owing to the low-energy reconstruction method, the energy range of gamma-hadron separation at IceCube was further extended to the sub-PeV range. In the 2012 dataset, the reconstructed energy of the most energetic gamma-ray candidate that survives the selection cuts is 4.8 PeV. However, it could not be excluded that this event is a cosmic ray that passed through the selection cuts.

In addition, the results achieved for the gamma-hadron separation were optimized for the point-source search of gamma rays based on observations from the LHAASO experiment. Multiple LHAASO-like mock sources were used to estimate the expected total number of gamma-ray events in one year of data. Furthermore, the significance of all selected mock sources was calculated with the Li & Ma method [86]. It was observed that, for the optimistic scenario of such a source at a zenith angle of $\theta < 10^\circ$ above IceCube, a discovery potential of $2.8\sigma$ can be achieved within one year of data.

A further study on the flux that would generate an observation with a $2\sigma$ sensitivity has been conducted for different assumptions of the spectral index. For a spectral index of $\gamma = 3$, the flux normalization factor $N_0$ was obtained to be $N_0 = 8.8 \cdot 10^{-16}\text{cm}^{-2}\text{s}^{-1}\text{TeV}^{-1}$.

Finally, the effective area has been calculated for six different zenith ranges spanning $0^\circ$ to $33^\circ$. The maximum effective area at an energy of $\sim 1.5$ PeV is $0.250\,\text{km}^2$, a third of the average geometric area for a zenith $\theta < 13.3^\circ$.

In summary, this thesis has laid the groundwork for future sub-PeV and PeV gamma-ray searches with IceCube by improving the reconstruction efficiency in the sub-PeV range and the gamma-hadron separation by at least an order of magnitude above 1 PeV. The methods developed apply to the 2012 dataset and can be adapted for the following years. Additional years of data will increase the total statistics, improving the overall quality of the analysis. Moreover, the next generation neutrino experiment at the South Pole, IceCube-Gen2, will also increase the field of view, expanding the visible portion of the Galactic Plane and enlarging the region of interest for potential sources.

# A. Event viewer

## A.1. Event viewer: a stand-alone software

The established software for event visualization in IceCube is `steamshovel`. This software has been extensively used for the dynamic representation of neutrino events. However, it has never performed as well for cosmic-ray air-shower event displays. For this reason, a new software was developed. It exclusively uses Python libraries and can display events of both the surface and the in-ice detector. It also shows important quantities such as LDF or time distribution. Furthermore, it was designed to display events with scintillators and antenna events, for the future IceTop enhancement and IceCube-Gen2. The software is stored in a GitHub repository [81] and has been under constant update for the past years.

## A.2. Events examples

Figure A.1 shows an example of a gamma-ray simulation. The viewer shows in the top left panel some information about the simulations and the frame that is visualized. The square plot in the top center of the image shows the geometry of the IceTop detector, and the two plots on the right side show the Lateral Distribution Function (LDF) and Time with respect to the shower front. The black line is the reconstruction fit, and the gray band is the uncertainty.

Figure A.2 shows an example of a proton simulation. The right plot this time shows the 3D view of the event with the surface and in-ice detectors. The pulses are shown with the colored dots, and the track is shown with the solid line.

Figure A.3 shows an example of a measured event with scintillators and radio antennas. The square plot in the top center of the image shows the geometry of the IceTop detector with the scintillators and antennas, and the two plots on the right side show the Lateral Distribution Function (LDF) and Time with respect to the shower front measured with scintillators. The two center lower plots show the signal measured by the radio antennas in the time and frequency domains.

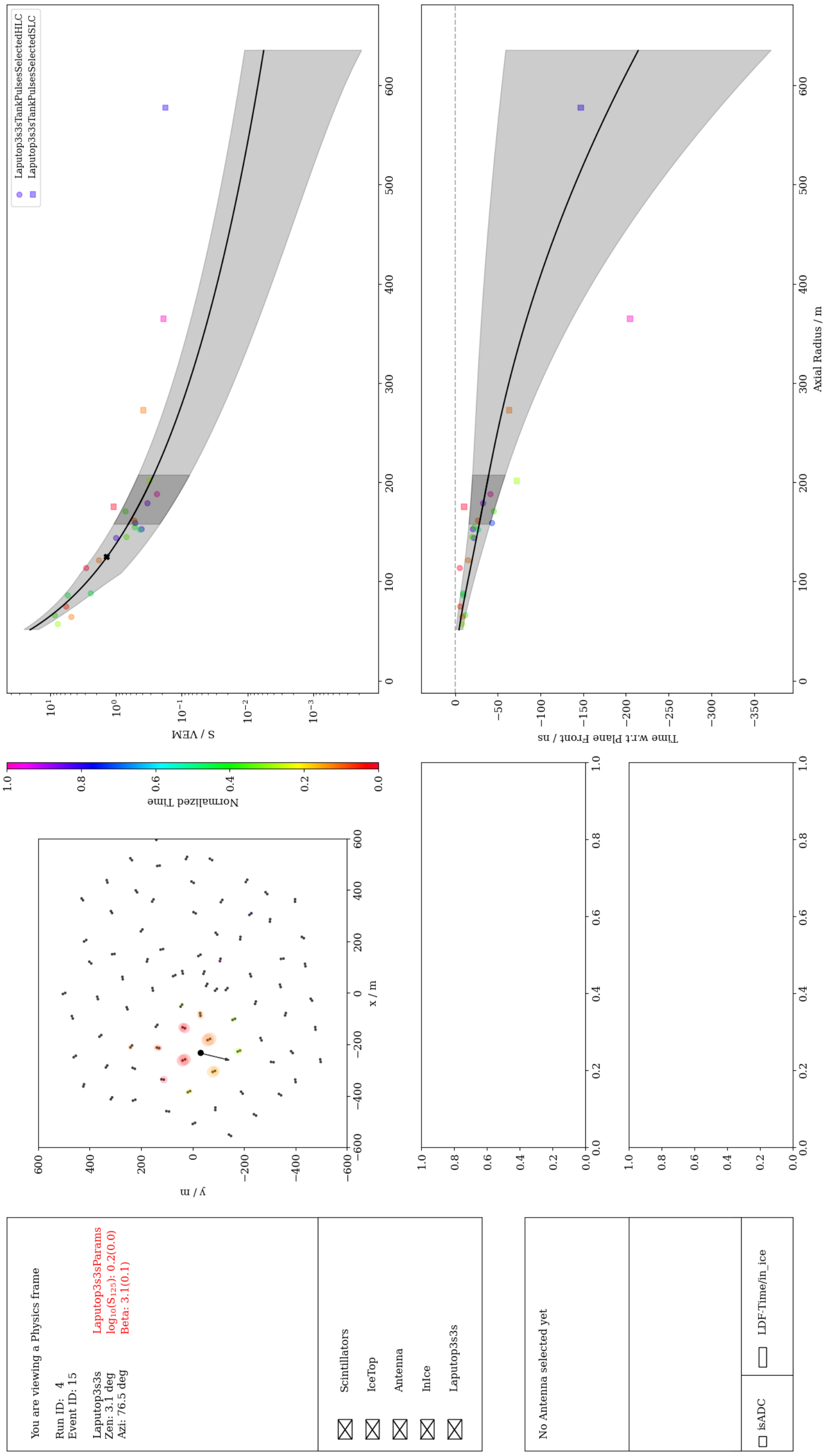

You are viewing a Physics frame

Run ID: 4
Event ID: 15

Laputop3s3s
Zen: 3.1 deg
Azi: 76.5 deg

Laputop3s3sParams
log$_{10}$(S$_{125}$): 0.2(0.0)
Beta: 3.1(0.1)

☒ Scintillators
☒ IceTop
☒ Antenna
☒ InIce
☒ Laputop3s3s

No Antenna selected yet

☐ isADC
☐ LDF-Time/in_ice

Figure A.1.: Event viewer of gamma-ray simulation with LDF and time plots

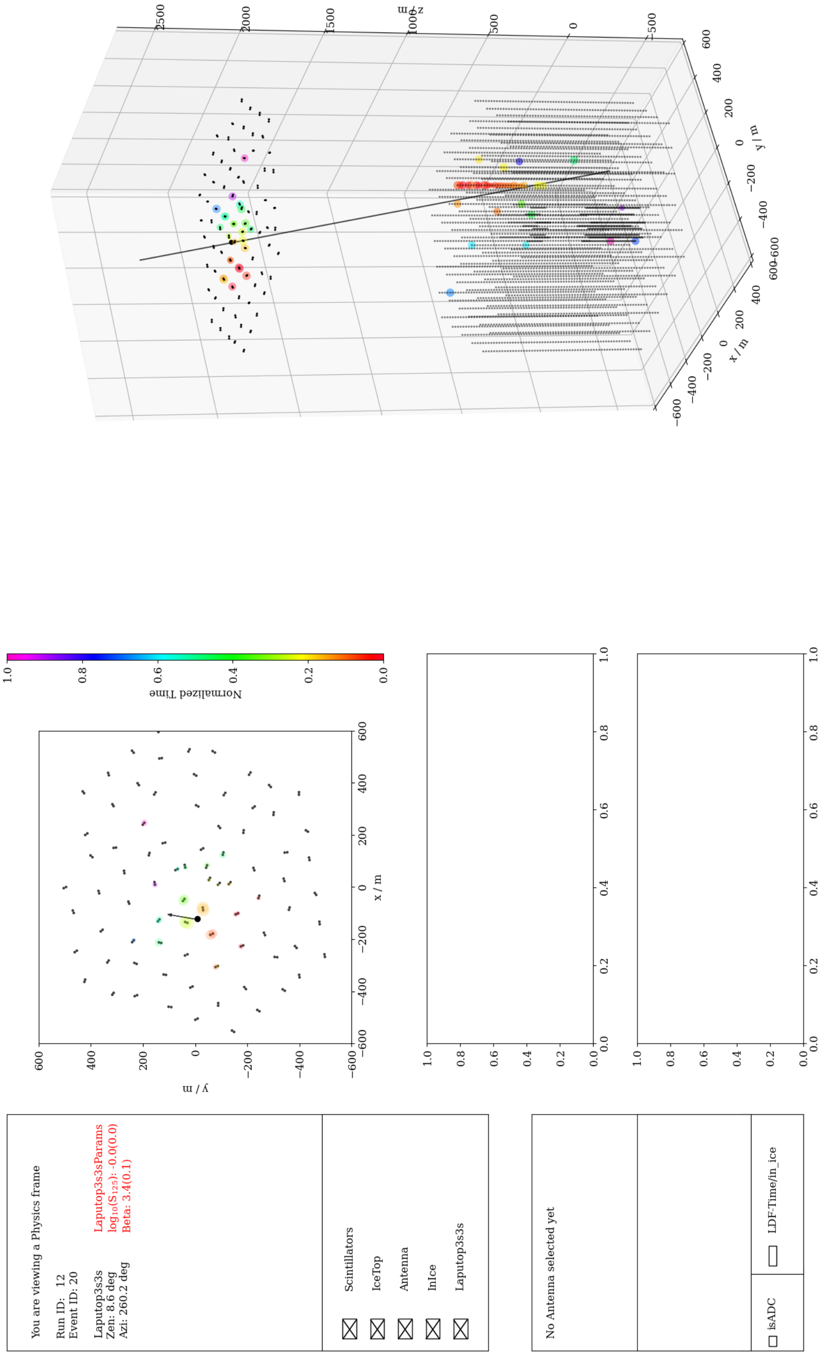

You are viewing a Physics frame

Run ID: 12
Event ID: 20

Laputop3s3s
Zen: 8.6 deg
Azi: 260.2 deg

Laputop3s3sParams
$\log_{10}(S_{125})$: -0.0(0.0)
Beta: 3.4(0.1)

☒ Scintillators
☒ IceTop
☒ Antenna
☒ InIce
☒ Laputop3s3s

No Antenna selected yet

☐ isADC
☐ LDF-Time/in_ice

Figure A.2.: Event viewer of proton simulation with the surface and in-ice detectors.

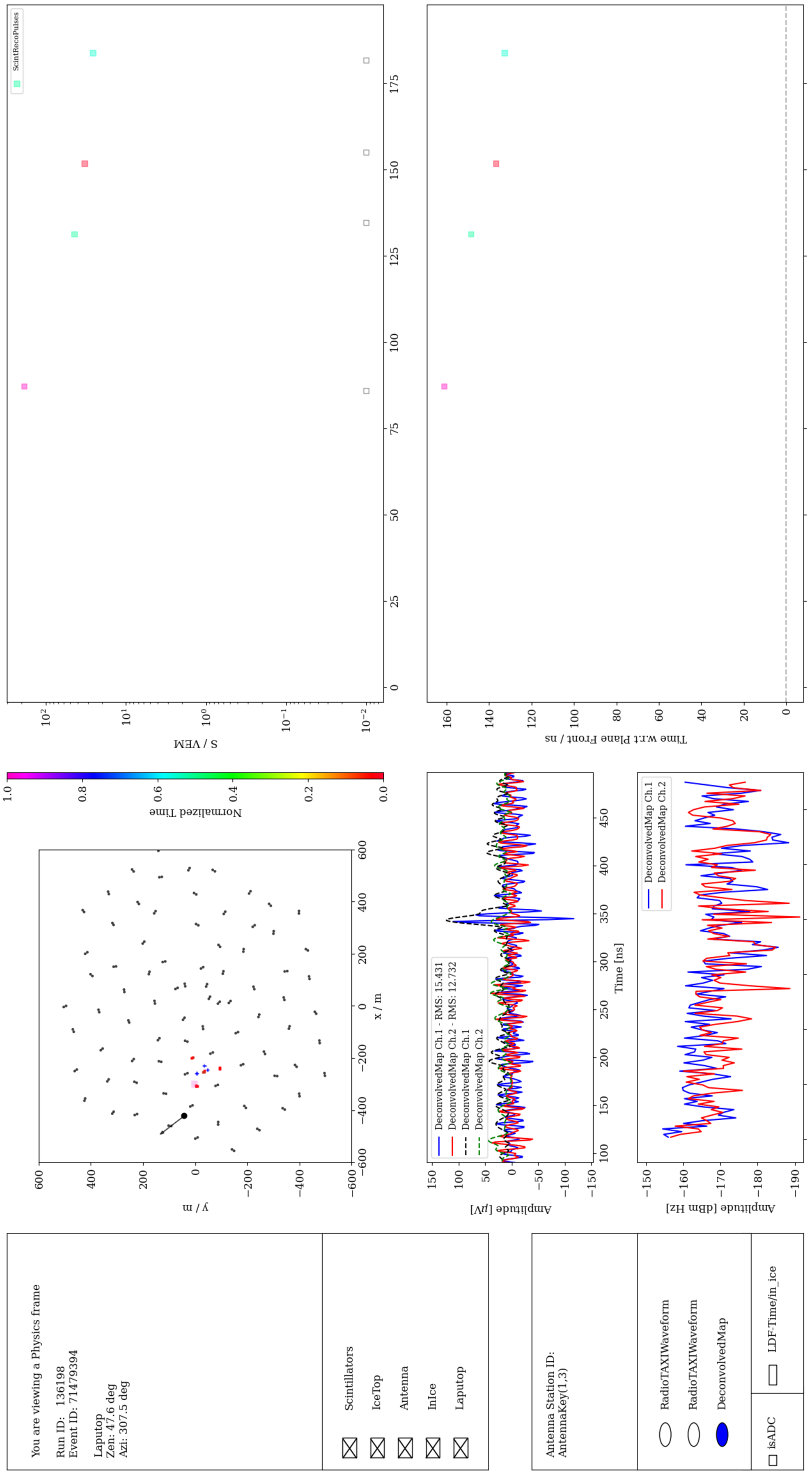

You are viewing a Physics frame

Run ID: 136198
Event ID: 71479394

Laputop
Zen: 47.6 deg
Azi: 307.5 deg

☒ Scintillators
☒ IceTop
☒ Antenna
☒ InIce
☒ Laputop

Antenna Station ID:
AntennaKey(1,3)

○ RadioTAXIWaveform
○ RadioTAXIWaveform
● DeconvolvedMap

☐ isADC
☐ LDF-Time/in_ice

Figure A.3.: Event viewer of data with scintillators and radio.

# B. Event selection

This appendix refers to Chapter 6. It shows some extra plots about the charge distance in-ice selection criteria and the effective area.

## B.1. Charge-Distance simulation comparison

Figure B.1 shows the Charge-Distance quantity for two sets of simulations and data. The gamma-ray and the proton simulations agree for both models Sibyll 2.1 and Sibyll 2.3d. Data are also contained within the Proton and Iron lines.

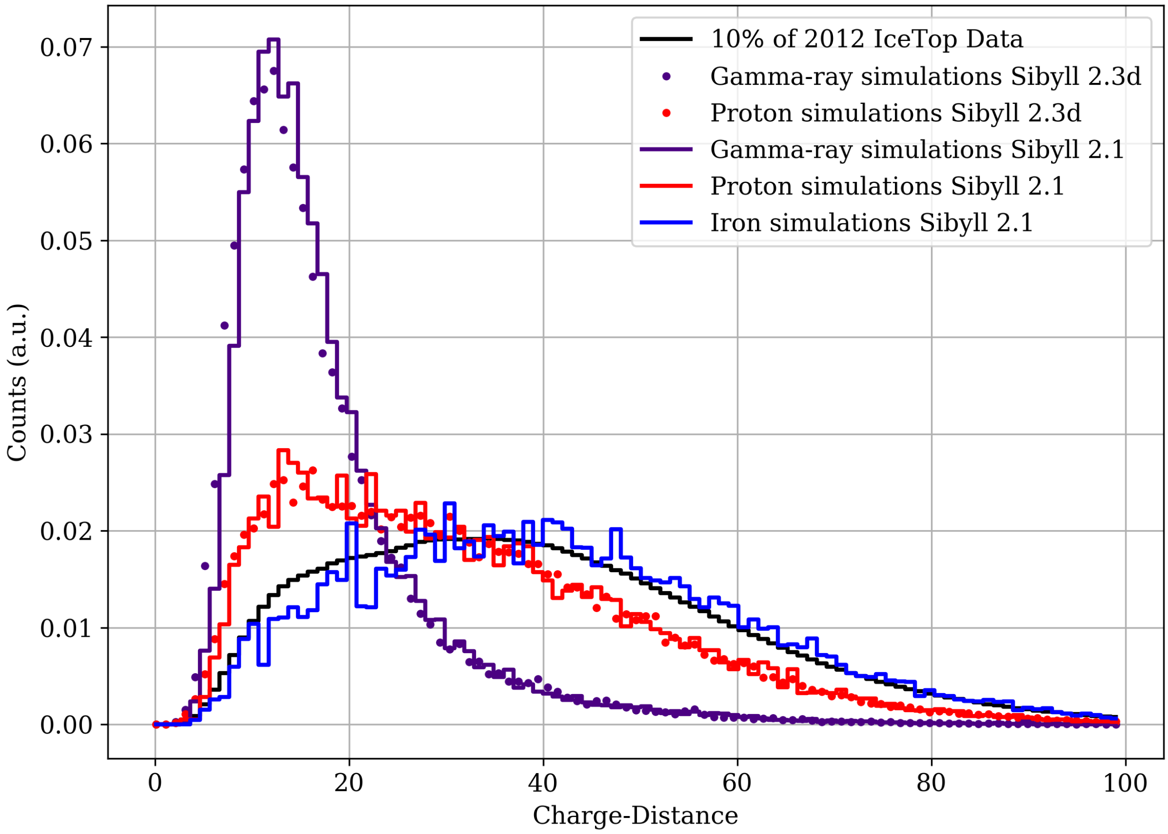

Figure B.1.: Icetop Charge-Distance for different datasets in the energy range from 5.0 to 7.0 in $\log_{10}(E/GeV)$. The solid lines show the Sibyll 2.1 simulations and the dots the Sibyll 2.3d ones.

## B.2. Only Charge-Distance selection

Figure B.2 shows the fraction of gamma-ray candidate events obtained exclusively using the Charge-Distance selection without the in-ice selection, the in-ice selection without the Charge-Distance selection, and the combined selection in the energy range from 5.0 to 7.0 in $\log_{10}(E/\mathrm{GeV})$. At lower energies, the Charge-Distance selection has a more relevant impact compared to the higher energies, because the muonic component is less energetic and does not always reach the in-ice detector.

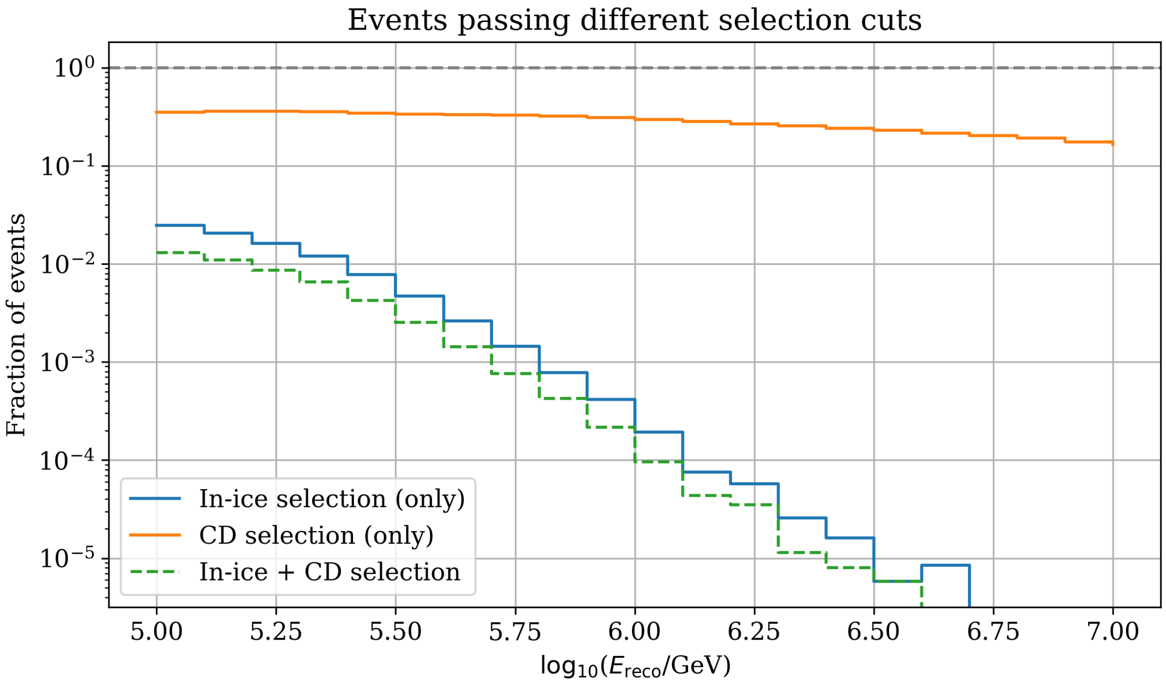

Figure B.2.: Icetop Charge-Distance selection without the in-ice selection, in-ice selection without the Charge-Distance selection, and the combined selection in the energy range from 5.0 to 7.0 in $\log_{10}(E/\mathrm{GeV})$.

## B.3. Flux normalization value for diffuse gamma-ray flux

Table B.1.: $N_0$ normalization factor as a function of spectral index $\gamma$ and $\log_{10}(E/\mathrm{GeV})$, in units of $10^{-16}\mathrm{cm}^{-2}\mathrm{s}^{-1}\mathrm{TeV}^{-1}$, as shown in Figure 6.16a.

| $\gamma$<br>$\log_{10}$(E/GeV) | 2.0 | 2.2 | 2.4 | 2.6 | 2.8 | 3.0 | 3.2 | 3.4 | 3.6 | 3.8 | 4.0 |
|---|---|---|---|---|---|---|---|---|---|---|---|
| 5.0 | 3.2 | 5.1 | 8.1 | 12.4 | 18.6 | 27.3 | 39.2 | 55.1 | 75.9 | 102.7 | 137.0 |
| 5.1 | 2.7 | 4.5 | 7.1 | 11.1 | 17.0 | 25.5 | 37.5 | 54.1 | 76.8 | 107.5 | 148.4 |
| 5.2 | 2.1 | 3.5 | 5.7 | 9.1 | 14.2 | 21.8 | 32.9 | 48.9 | 71.6 | 103.6 | 148.2 |
| 5.3 | 1.6 | 2.7 | 4.5 | 7.3 | 11.6 | 18.3 | 28.4 | 43.5 | 65.9 | 98.7 | 146.4 |
| 5.4 | 1.3 | 2.2 | 3.6 | 6.0 | 9.8 | 15.8 | 25.3 | 40.1 | 62.8 | 97.6 | 150.3 |
| 5.5 | 1.0 | 1.8 | 3.0 | 5.1 | 8.5 | 14.1 | 23.3 | 38.1 | 61.8 | 99.4 | 158.8 |
| 5.6 | 0.8 | 1.4 | 2.4 | 4.2 | 7.2 | 12.3 | 20.8 | 35.2 | 59.0 | 98.4 | 163.2 |
| 5.7 | 0.6 | 1.1 | 1.9 | 3.4 | 6.1 | 10.7 | 18.7 | 32.7 | 56.8 | 98.2 | 168.8 |
| 5.8 | 0.5 | 0.9 | 1.7 | 3.0 | 5.5 | 10.0 | 18.1 | 32.7 | 58.9 | 105.6 | 188.8 |
| 5.9 | 0.4 | 0.7 | 1.4 | 2.6 | 4.8 | 9.1 | 17.0 | 31.8 | 59.3 | 110.3 | 204.7 |
| 6.0 | 0.4 | 0.6 | 1.2 | 2.4 | 4.6 | 8.8 | 17.2 | 33.2 | 64.3 | 124.1 | 239.1 |
| 6.1 | 0.4 | 0.7 | 1.3 | 2.7 | 5.3 | 10.7 | 21.4 | 42.9 | 86.0 | 172.3 | 344.6 |
| 6.2 | 0.5 | 1.1 | 2.2 | 4.5 | 9.3 | 19.2 | 39.7 | 82.4 | 170.7 | 353.7 | 732.2 |

## B.4. Effective area and polynomial fit values

Table B.2.: Parameters of the effective area (after quality cuts and gamma-ray selection) $x_0$, ... ,$x_3$ of the polynomial $p(E) = x_0 + x_1E + x_2E^2 + x_3E^3$ with uncertainties for each zenith angle range, as shown in Figure 6.18.

| Zenith Range | $x_0$ | $x_1$ | $x_2$ | $x_3$ |
|---|---|---|---|---|
| $0.0 < \theta < 13.3$ | $-31.3 \pm 4.15$ | $11.9 \pm 2.28$ | $-1.01 \pm 0.41$ | $0.008 \pm 0.024$ |
| $13.3 < \theta < 18.9$ | $-24.3 \pm 13.8$ | $7.88 \pm 7.53$ | $-0.29 \pm 1.36$ | $-0.04 \pm 0.08$ |
| $18.9 < \theta < 23.2$ | $-55.4 \pm 10.8$ | $22.8 \pm 5.7$ | $-2.72 \pm 1.01$ | $0.10 \pm 0.06$ |
| $23.2 < \theta < 26.8$ | $-62.2 \pm 14.5$ | $25.2 \pm 7.5$ | $-2.99 \pm 1.30$ | $0.11 \pm 0.07$ |
| $26.8 < \theta < 30.1$ | $-22.6 \pm 47.4$ | $3.0 \pm 23.9$ | $1.01 \pm 4.01$ | $-0.13 \pm 0.22$ |
| $30.1 < \theta < 33.0$ | $6.5 \pm 110.9$ | $-12.6 \pm 54.0$ | $3.7 \pm 8.7$ | $-0.28 \pm 0.47$ |

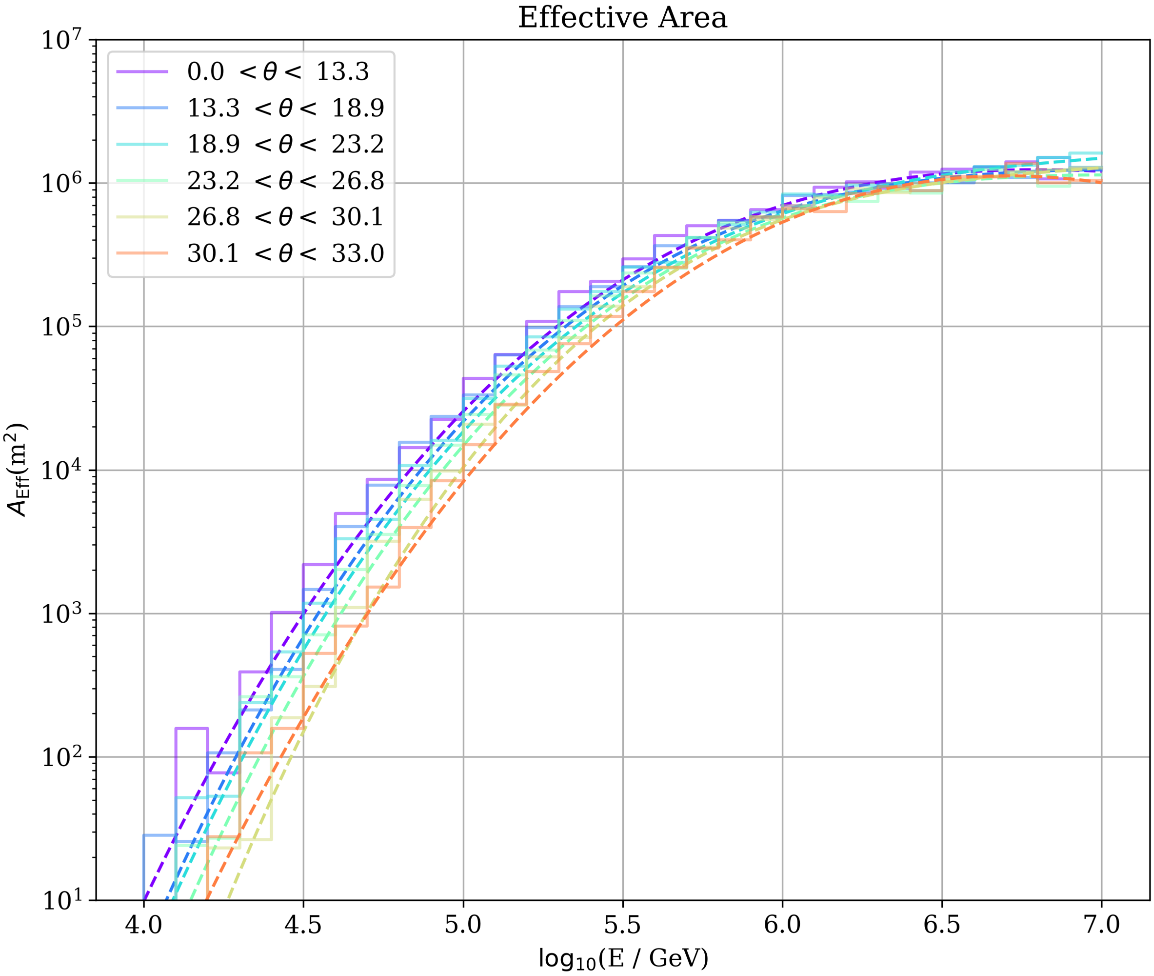

Figure B.3.: Effective area without quality cuts and gamma-ray selection for different zenith bins. Fit parameters can be found in Table B.3

Table B.3.: Parameters of the effective area (without quality cuts and gamma-ray selection) $x_0$, ... ,$x_3$ of the polynomial $p(E) = x_0 + x_1E + x_2E^2 + x_3E^3$ with uncertainties for each zenith angle range, as shown in Figure B.3.

| Zenith Range | $x_0$ | $x_1$ | $x_2$ | $x_3$ |
|---|---|---|---|---|
| $0.0 < \theta < 13.3$ | $-48.1 \pm 7.5$ | $22.0 \pm 4.1$ | $-2.94 \pm 0.74$ | $0.130 \pm 0.044$ |
| $13.3 < \theta < 18.9$ | $-57.1 \pm 5.9$ | $26.5 \pm 3.3$ | $-3.71 \pm 0.60$ | $0.174 \pm 0.036$ |
| $18.9 < \theta < 23.2$ | $-57.7 \pm 5.1$ | $26.8 \pm 2.8$ | $-3.77 \pm 0.51$ | $0.178 \pm 0.030$ |
| $23.2 < \theta < 26.8$ | $-60.1 \pm 6.4$ | $27.5 \pm 3.5$ | $-3.82 \pm 0.63$ | $0.176 \pm 0.038$ |
| $26.8 < \theta < 30.1$ | $-77.1 \pm 6.8$ | $35.7 \pm 3.7$ | $-5.14 \pm 0.66$ | $0.248 \pm 0.039$ |
| $30.1 < \theta < 33.0$ | $-46.1 \pm 5.1$ | $19.4 \pm 2.8$ | $-2.30 \pm 0.49$ | $0.085 \pm 0.029$ |

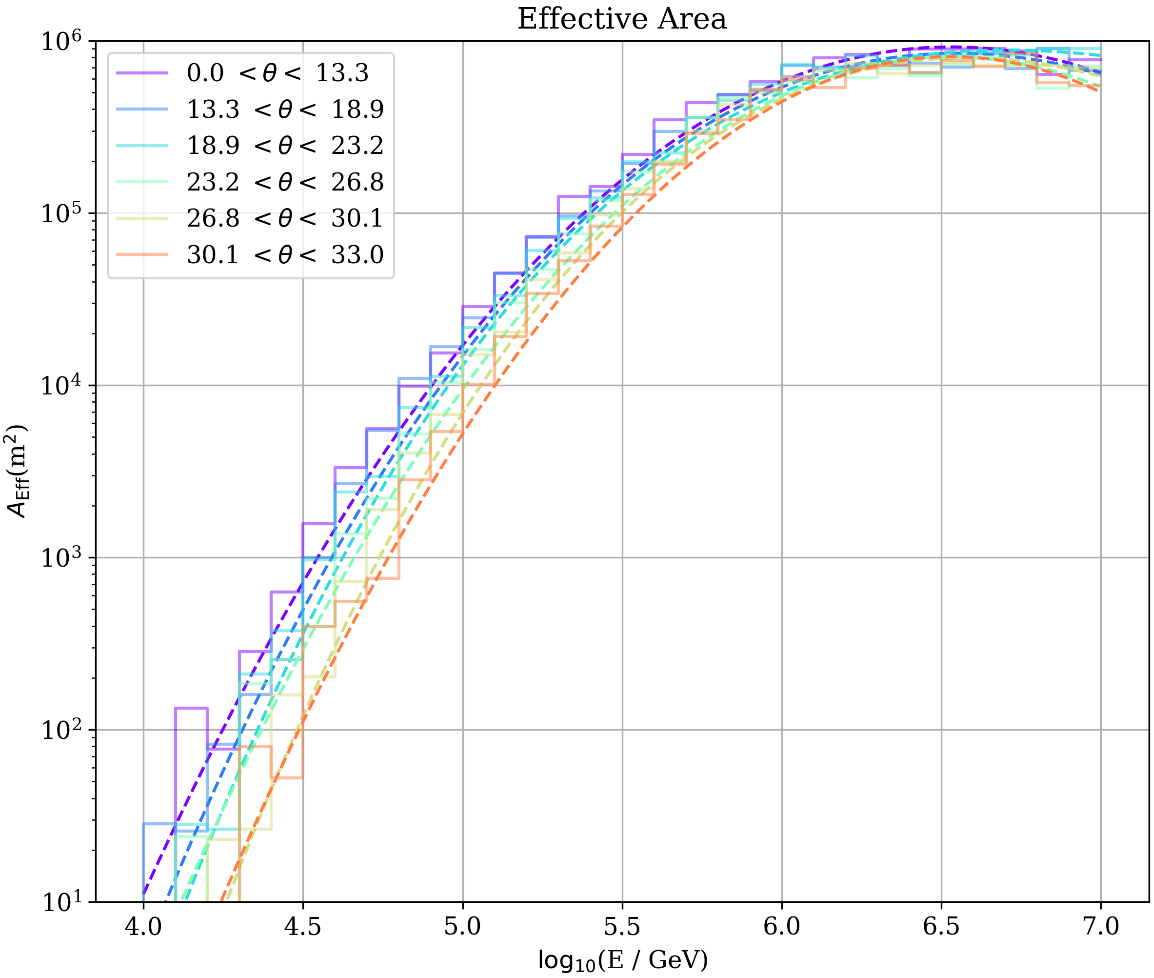

Figure B.4.: Effective area after quality cuts for different zenith bins. Fit parameters in Table B.4

Table B.4.: Parameters of the effective area (after quality cuts) $x_0$, ... ,$x_3$ of the polynomial $p(E) = x_0 + x_1 E + x_2 E^2 + x_3 E^3$ with uncertainties for each zenith angle range, as shown in Figure B.4.

| Zenith Range | $x_0$ | $x_1$ | $x_2$ | $x_3$ |
|---|---|---|---|---|
| $0.0 < \theta < 13.3$ | $-31.6 \pm 6.7$ | $12.7 \pm 3.7$ | $-1.25 \pm 0.66$ | $0.028 \pm 0.039$ |
| $13.3 < \theta < 18.9$ | $-41.1 \pm 6.4$ | $17.5 \pm 3.5$ | $-2.05 \pm 0.64$ | $0.073 \pm 0.039$ |
| $18.9 < \theta < 23.2$ | $-52.4 \pm 6.6$ | $23.4 \pm 3.6$ | $-3.08 \pm 0.66$ | $0.133 \pm 0.039$ |
| $23.2 < \theta < 26.8$ | $-33.6 \pm 5.6$ | $12.9 \pm 3.1$ | $-1.19 \pm 0.55$ | $0.020 \pm 0.033$ |
| $26.8 < \theta < 30.1$ | $-54.2 \pm 6.7$ | $23.1 \pm 3.7$ | $-2.87 \pm 0.65$ | $0.112 \pm 0.039$ |
| $30.1 < \theta < 33.0$ | $-34.5 \pm 10.6$ | $12.5 \pm 5.7$ | $-0.98 \pm 1.01$ | $0.003 \pm 0.059$ |

# C. Csky: a software for point-source searches

Csky is an IceCube software package originally developed for the analysis of in-ice cascade events. The name "csky" refers both to its origins in C++ and the idea of "seeing" the sky with neutrinos. Over time, it has evolved into a versatile tool for high-energy neutrino astronomy, supporting a wide range of analyses beyond its initial scope of application.

## C.1. Overview

The Csky software is highly versatile, enabling a variety of analyses in neutrino astronomy. The most relevant for this work is the unbinned likelihood maximization method, designed for astrophysical source searches using IceCube data.
Csky employs profiling techniques to enhance computational speed, at the cost of increasing internal complexity. Numerous analyses have been successfully conducted using csky. It also enables the user to replicate previously published results with minimal effort. The software is user-friendly and widely adopted within the community. Some of the primary applications of the software package are performing an all-sky search, externally triggered transient follow-up search, stacking analysis, and detecting significant excesses in the sky. For its modular and extensible structure, csky can be easily adapted for analyses beyond neutrino astronomy. For example, in the context of this thesis, it was used to set up a gamma-ray point source search. The software components are structured to allow for straightforward expansion and customization by both developers and users.

## C.2. Dataset Preparation

The csky software requires input files arranged in a specific format. These datasets are stored as NumPy files [87], following a well-defined structure. The input data for csky relevant to this thesis consists of two sets: one containing observational air-shower data from 2012 and the other one with corresponding Monte Carlo (MC) gamma-ray simulations. The relevant variables are stored in NumPy arrays [87] with the following structure:

- **Standard Variables (Used for Both Data and MC):**

- *time*: Timestamp of the event.
- *run*: Run number identifying the data-taking period.
- *event*: Event ID within the corresponding run.
- *subevent*: Identifier for subevents within the same event.
- *ra*: Reconstructed right ascension of the event.
- *dec*: Reconstructed declination of the event.
- *azi*: Azimuthal angle of the reconstructed event direction.
- *zen*: Zenith angle of the reconstructed event direction.
- *logE*: Logarithm (base 10) of the reconstructed energy.
- *angErr*: Angular reconstruction uncertainty.

- **MC-Specific Variables (Only in Simulations):**
  - *trueE*: Simulated energy of the event.
  - *trueRa*: Simulated right ascension of the event.
  - *trueDec*: Simulated declination of the event.
  - *ow*: One-weight, used for correcting simulation differences and for the effective area calculation.

Most of the above variables are either directly accessible or can be computed with minimal effort, except for *ow* and *angErr*. The *ow* variable depends on the simulation set and is computed using the `simweights` software [74] under the assumption of a flux with a spectral index of $\gamma = 1$. Weighting with any spectral index can be performed by multiplying the weight by the energy raised to the corresponding power. The *angErr* variable represents the uncertainty in directional reconstruction. Section 4.5.2 presented the studies for the angular resolution.

## C.3. Implementation of Unbinned Maximum Likelihood Analysis in csky

As mentioned earlier, in this work, the Unbinned Maximum Likelihood Analysis method can be been used within the csky framework to conduct a gamma-ray point source search. The main concept of this method for point source searches was first introduced in [88]. It allows for the search for "clustering" of events from astrophysical point sources, by distinguishing the signal-like events from their respective background. Hence, two competing hypotheses are needed for the likelihood test:

- Null hypothesis ($H_0$): Sample containing only background events. In this analysis, background events are hadronic cosmic rays and diffuse gamma rays.
- Signal hypothesis ($H_\mathrm{s}$): Some signal events associated with astrophysical gamma-ray point sources are present in the dataset, along with background events.

To test these hypotheses, a likelihood function $L(n_s, \gamma)$ within the csky framework is defined, named sigsub, where a signal subtraction is performed in the background:

$$L(\vec{\mu}) = \prod_{\text{events}} \left[ \frac{n_s}{N} \cdot S(\mathrm{dec}, \sigma) + \left(1 - \frac{n_s}{N}\right) \cdot D(\mathrm{dec}) \right], \tag{C.1}$$

with $D = (n_s/N) \cdot S + (1 - n_s/N) \cdot B$. $n_s$ is the parameter representing the number of signal events, $\gamma$ is the spectral index of the source, $N$ is the total number of events, $S(\mathrm{dec}, \sigma)$ is the signal probability density function (PDF), constructed from Monte Carlo simulations, where $\sigma$ is the associated angular error for each event, and $B(\mathrm{dec})$ is the background PDF, constructed from data with the signal subtraction applied, the product $\prod_i$ is taken over all events $i$ in the dataset.

The functions $S(\mathrm{dec}, \sigma)$ and $B(\mathrm{dec})$ represent the expected spatial and energy distributions of signal and background events, respectively.

Given this likelihood function, the total likelihood ratio test statistic, denoted as TS, is defined. It is a measure of the relative likelihood between two hypotheses—specifically, the null hypothesis of $n_s = 0$ (no signal), and the alternative hypothesis corresponding to the best-fit value of $n_s$, the parameter value that maximizes $L(n_s, \gamma)$.

The test statistic TS is defined as:

$$\mathrm{TS} = -2 \ln \left[ \frac{L(n_s = 0)}{L(\text{best fit } n_s)} \right]. \tag{C.2}$$

The TS values are used to estimate the p-values and are directly correlated with the signal hypothesis, as explained later.

## C.4. Background Estimation and Spline Fit

As mentioned above, csky internally defines likelihood functions and both signal and background probability density functions (PDFs). The signal PDF is constructed with gamma-ray simulations, whereas the background estimation is directly derived from data. Surviving the gamma-hadron separation explained in Chapter 6.

Furthermore, csky supports spline fitting techniques for background modeling. The following section presents an example of how background smoothing and spline fitting are applied in this analysis. In Figure C.1, the parameters obtained from the $\chi^2$ fit of the background are shown as a function of declination.

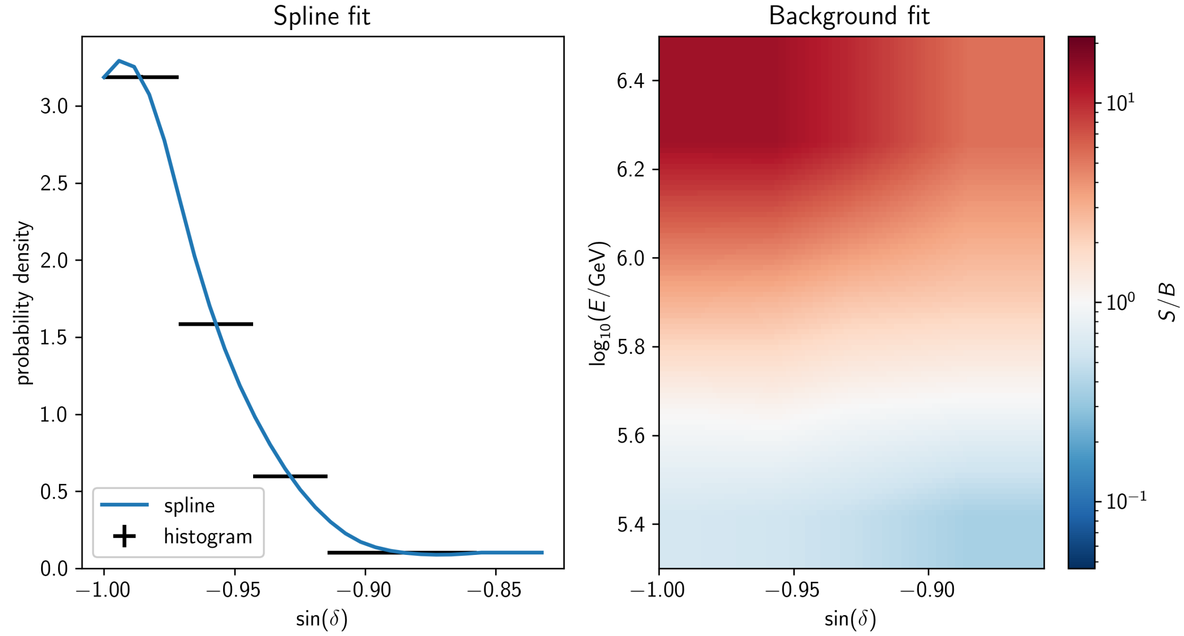

Figure C.1.: Spline fit and background estimation with a spectral index $\gamma = 3$, and declination $-90^\circ < \delta < 90^\circ$.

## C.5. Trial Analysis

Source searches in the sky are conducted after modeling the background. Once the background is established, as a first step, background trials are performed across all declinations. Following this, signal injection tests are conducted.

### C.5.1. Background Trials

While the background is supposed to be uniform in right ascension (RA), it exhibits strong declination dependence due to the declination dependence of IceCube's effective area for gamma rays, as explained in Section 6.6.

To preserve this declination dependence, the test statistic (TS) value for a background-like case is evaluated in different declination bins. For each declination bin, the RA of all events is scrambled. This procedure constructs a background-like dataset. This is also realistic by the assumption that the majority of events in the dataset do not originate from the gamma-ray sources under investigation.

This scrambling procedure is further repeated 50,000 times to generate independent background events. For each trial, a TS value is computed, resulting in a background TS distribution. These values are shown in Figure C.2. The blue points in the plots represent the TS values from all 50,000 trials. The background TS values (blue points) are fitted using a $\chi^2$ function (in red). In Fig. C.2, the results are shown for different declination bins $-89^\circ < \delta < -59^\circ$, and the corresponding parameters are plotted for all declinations in Figure C.3.

These steps involve using the complete dataset of measured air showers passing the gamma-hadron separation and the full set of simulations for scrambling. The rationale behind this approach is that scrambling the right ascension (RA) in data provides the best background estimation while preserving the declination dependence. This ensures that all potential sources are effectively removed, minimizing the risk of bias in the analysis.

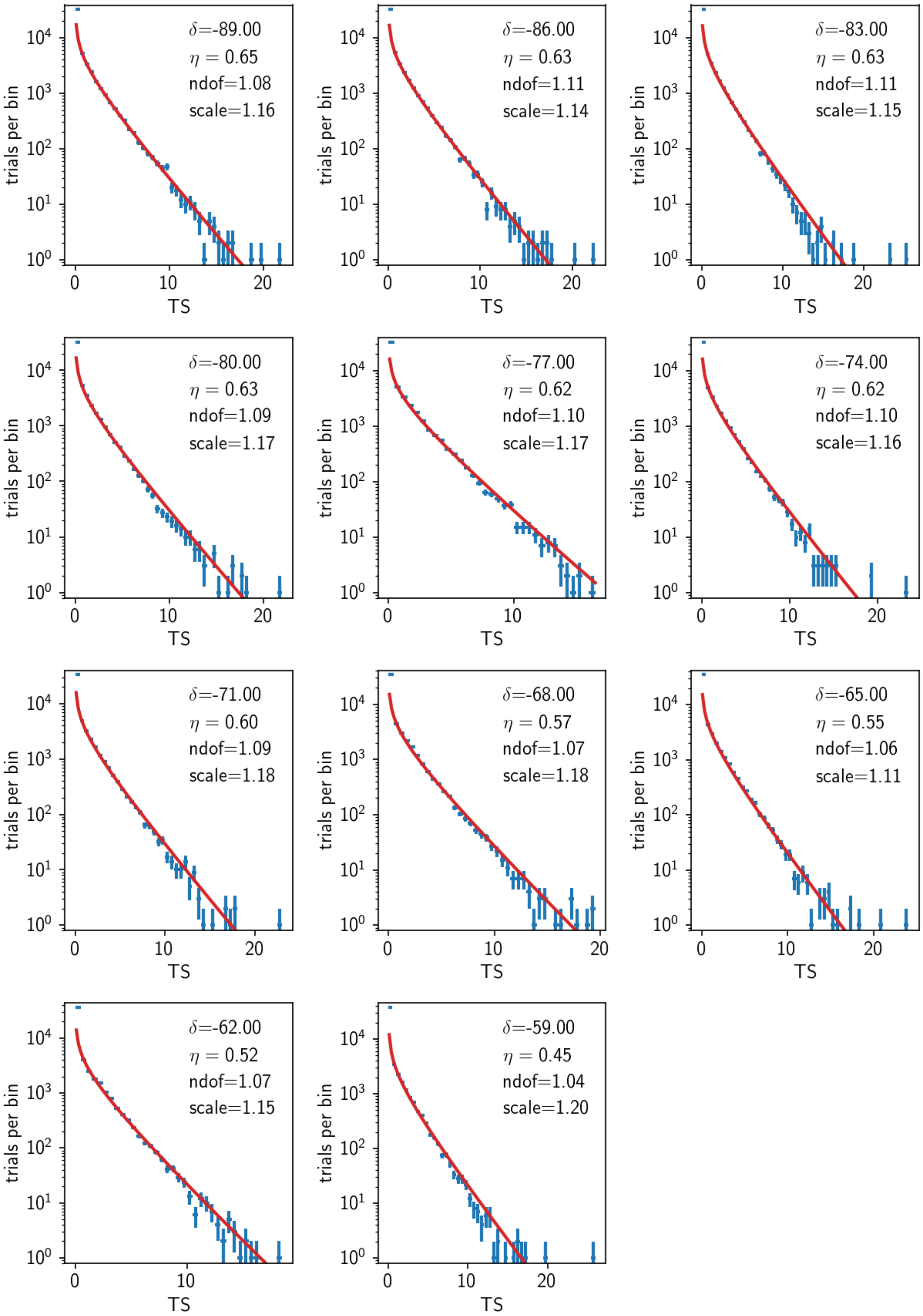

Figure C.2.: Example of background trials for multiple declinations. The red line shows the fit to the multiple backgrounds trials. The total number of trials is 50,000 per declination bin (each sub-plot). The declination $\delta$, the ndof, $\eta$, and scale are the parameters for the definition of the $\chi^2$ TS function. The values of those parameters are shown in each plot.

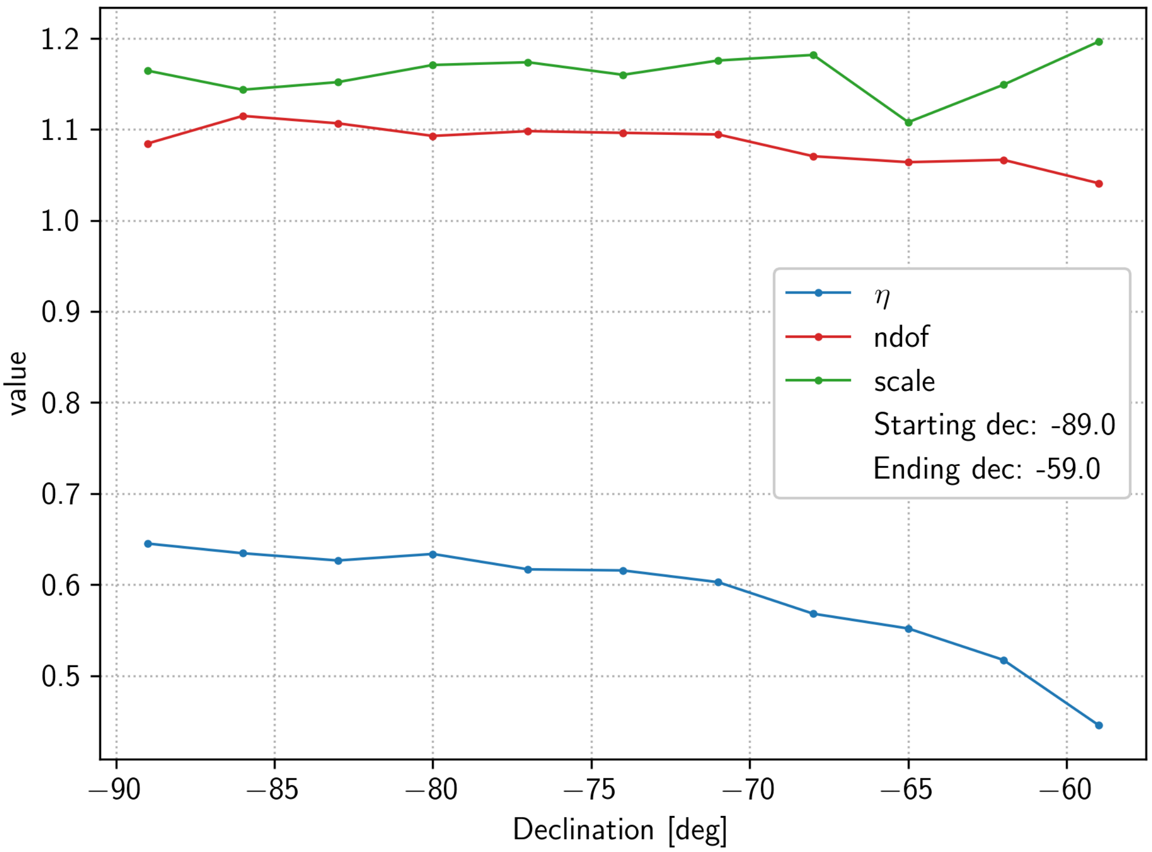

Figure C.3.: Example of background parameters for all trials for multiple declination. The red line shows the fit to the multiple backgrounds trials. The total number of trials is 50,000 per bin. The declination $\delta$, the ndof, $\eta$, and scale are the parameters for the definition of the $\chi^2$ TS function.

### C.5.2. Signal Trials

Once background trials are performed, the resulting background distribution is used as a null hypothesis against which the signal injections are tested. This process allows the evaluation of the sensitivity of the analysis for a signal flux with a given spectral index and estimates the number of signal events. The primary goal is to assess the accuracy of background modeling and signal recovery as a function of declination. The number of signal events injected per declination bins is: 0, 5, 10, 15, 25.

In Fig. C.4, some example signal recovery plots are shown. Here, the number of injected signal events, $n_{inj}$, is plotted as a function of the best fit number of recovered events, $n_s$. The bias on the spectral index $\gamma$ of the fitted recovered signal events is also shown. The injected signal events are from a flux with $\gamma = 3$, and can be compared with the recovered $\gamma$ values. For the best-case scenario $n_{inj} = n_s$ and $\gamma = 3$. Discrepancies in the plots may have been caused by the `angErr` values, which are not best represented by the model used for these plots. Because of time constraints, this could not be further investigated.

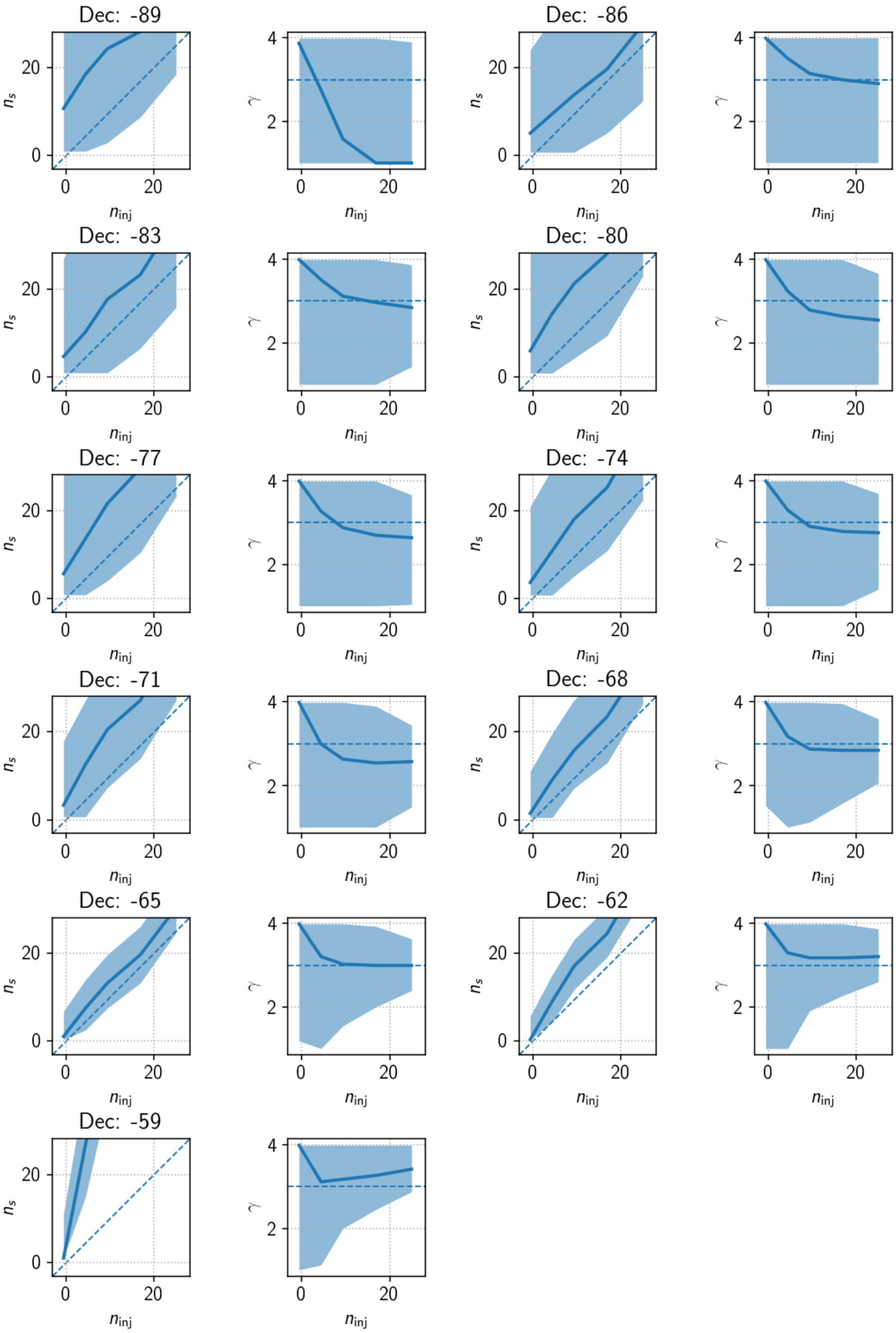

Figure C.4.: Example of signal injections for multiple declination. The total number of trials is 50,000 for each declination bin and number of signals injected. The solid line indicates the mean of the distribution of the reconstructed number of signal events or spectral index. The shaded region is the $1\sigma$ uncertainty.

## C.6. All-Sky Search

The search for point sources in the sky is conducted using both the modeled background and signal injection results. The sky map is first scrambled in RA. Then an excess is searched for across the entire sky. When an excess is detected, the statistical significance is quantified by calculating the corresponding p-value.

This process is repeated multiple times to improve statistical robustness. Then, the final p-value is obtained through post-trial corrections. To achieve a $-\log_{10}(p_{value}) = n$, at least $10^n$ trials are required. However, having trials of the order of $10^{(n+1)}$ would result in a more accurate p-value. The reason is that it is derived from the logarithm of the trial distribution. To ensure statistical stability and mitigate fluctuations, it is recommended to perform an additional order of magnitude more trials.

Figure C.5 shows the result of a single sky scan. The plots are shown in polar coordinates with the South Pole as the center of the sky. The plots show the $-\log_{10}(p_{value})$, Test Statistic (TS), number of signals ($n_s$), and spectra index $\gamma$. The plots are obtained using the full dataset of 2012, scrambled in RA.

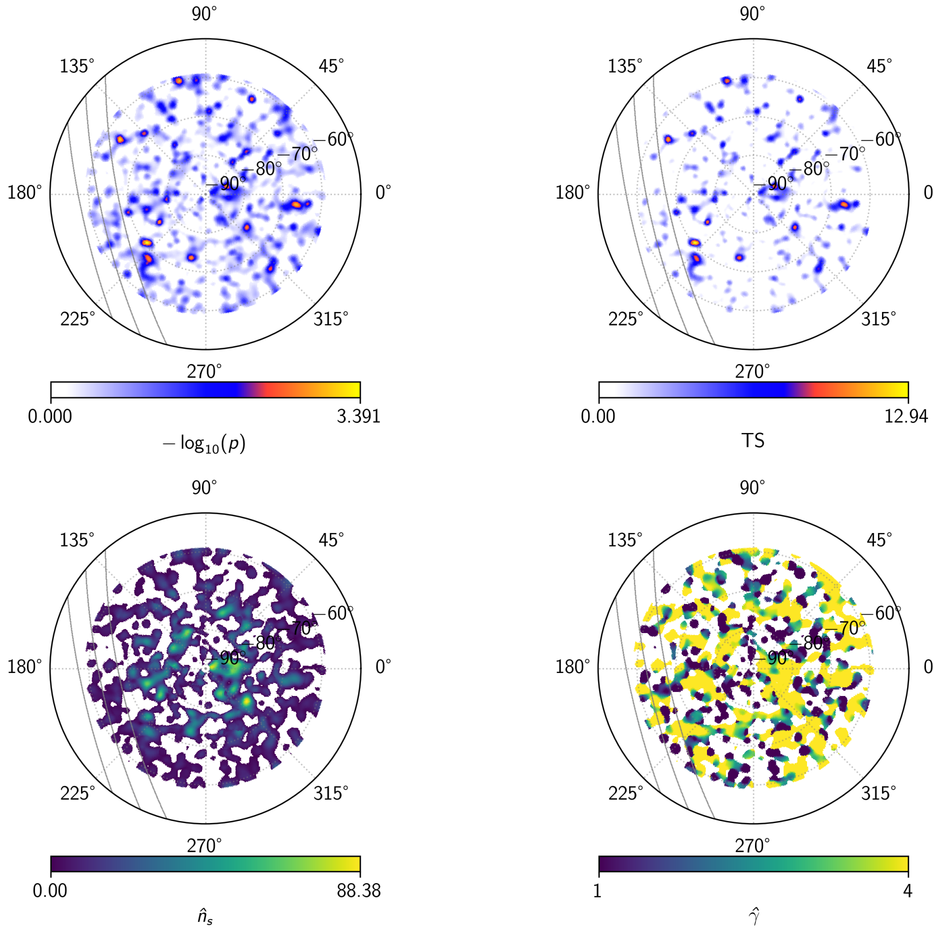

Figure C.5.: Example of an all sky scan with csky. The plots are shown in polar coordinates with the South Pole as the center of the sky. The plots show the $-\log_{10}(p_{value})$, Test Statistic (TS), number of signals ($n_s$), and spectra index $\gamma$. The plots are obtained using the full dataset of 2012, scrambled in RA.

## C.7. Future Steps

The analysis did not progress further due to time constraints, but all scripts are available on GitHub [81]. However, one remaining issue is the anomaly in the signal injection behavior that requires further investigation (Section C.5.2).

### C.7.1. Towards Unblinding

Before unblinding, additional steps are required, including code review and analysis validation. Nevertheless, this thesis has already demonstrated a reliable method for gamma-hadron separation, improving upon previous analyses. Therefore, the focus can now shift to finalizing the search for gamma-ray sources.

### C.7.2. Trial Correction

After performing the all-sky search, the most significant p-value in the sky will be identified. This value must then be corrected through post-trial analysis.
Post-trial analysis is essential because the full-sky search involves testing multiple locations, increasing the probability of statistical fluctuations mimicking a signal. Once the post-trial correction is applied, the true p-value is determined, allowing for an assessment of statistical significance and a potential discovery claim.

## C.8. Outlook

This analysis was conducted using only a single year of data, but can be extended to all years of IceCube data. Each year, a dedicated simulation set is required due to the snow accumulation on top of the tanks. Producing simulations for multiple years was not feasible within the given time frame of this PhD work. However, the methods developed in this work can be easily extended to include additional years of data. Future studies can adopt and apply these techniques for a more comprehensive multi-year analysis.

# D. Software and data storage

All the scripts can be found in the GitHub repositories [81].
The data, environments, and software can be found on the IceCube server in Madison and the analysis wiki [89, 90, 91].
Table 3.1 shows the total number of events simulated for the analysis. However, the simulations have been extended. Specifically, CORSIKA gamma rays were simulated up to 10,000 showers for each energy bin $4.0 < \log(E/\mathrm{GeV}) < 7.0$ in 0.1 log-binning. CORSIKA protons were simulated up to 10,000 showers for each energy bin $4.5 < \log(E/\mathrm{GeV}) < 6.5$ in 0.1 log-binning. The corresponding detector response was also simulated for both primaries for the year 2012 up to level 3, including the in-ice detector response.
Thanks to Megha Venugopal, Sebastian Carrasco, and Andrea Parenti, the simulations have been copied to Madison, tested, and validated.

# E. Bibliography

[1] V. Hess, *On the Observations of the Penetrating Radiation during Seven Balloon Flights*, *Phys. Z.* **13** (1912) 1084 [`1808.02927`].

[2] T.K. Gaisser, R. Engel and E. Resconi, *Cosmic Rays and Particle Physics*, Cambridge University Press, 2 ed. (2016), https://doi.org/10.1017/CBO9781139192194.

[3] TELESCOPE ARRAY collaboration, *An extremely energetic cosmic ray observed by a surface detector array*, *Science* **382** (2023) abo5095 [`2311.14231`].

[4] FERMI-LAT collaboration, *Fermi Large Area Telescope Fourth Source Catalog*, *Astrophys. J. Suppl.* **247** (2020) 33 [`1902.10045`].

[5] S. Vernetto and for the LHAASO collaboration, *Gamma ray astronomy with lhaaso*, *Journal of Physics: Conference Series* **718** (2016) 052043.

[6] H.E.S.S. collaboration, *The energy spectrum of cosmic-ray electrons at TeV energies*, *Phys. Rev. Lett.* **101** (2008) 261104 [`0811.3894`].

[7] CTA CONSORTIUM collaboration, *Design concepts for the Cherenkov Telescope Array CTA: An advanced facility for ground-based high-energy gamma-ray astronomy*, *Exper. Astron.* **32** (2011) 193 [`1008.3703`].

[8] HAWC collaboration, *Multiple Galactic Sources with Emission Above 56 TeV Detected by HAWC*, *Phys. Rev. Lett.* **124** (2020) 021102 [`1909.08609`].

[9] ICECUBE collaboration, *Cosmic ray spectrum and composition from pev to eev using 3 years of data from icetop and icecube*, *Phys. Rev. D* **100** (2019) 082002.

[10] AMS collaboration, *Precision Measurement of the Proton Flux in Primary Cosmic Rays from Rigidity 1 GV to 1.8 TV with the Alpha Magnetic Spectrometer on the International Space Station*, *Phys. Rev. Lett.* **114** (2015) 171103.

[11] PIERRE AUGER collaboration, *The energy spectrum of cosmic rays beyond the turn-down around* $10^{17}$ *eV as measured with the surface detector of the Pierre Auger Observatory*, *Eur. Phys. J. C* **81** (2021) 966 [`2109.13400`].

[12] T. Sanuki, M. Motoki, H. Matsumoto, E.S. Seo, J.Z. Wang, K. Abe et al., *Precise measurement of cosmic-ray proton and helium spectra with the bess spectrometer*, *The Astrophysical Journal* **545** (2000) 1135.

[13] CALET collaboration, *Direct Measurement of the Cosmic-Ray Proton Spectrum from 50 GeV to 10 TeV with the Calorimetric Electron Telescope on the International Space Station*, *Phys. Rev. Lett.* **122** (2019) 181102 [`1905.04229`].

[14] Y.S. Yoon, H.S. Ahn, P.S. Allison, M.G. Bagliesi, J.J. Beatty, G. Bigongiari et al., *Cosmic-ray proton and helium spectra from the first cream flight*, *The Astrophysical Journal* **728** (2011) 122.

[15] DAMPE collaboration, *Direct detection of a break in the teraelectronvolt cosmic-ray spectrum of electrons and positrons*, *Nature* **552** (2017) 63 [`1711.10981`].

[16] ICECUBE collaboration, *Probing the PeV Region in the Astrophysical Neutrino Spectrum using $\nu_\mu$ from the Southern Sky*, `2502.19776`.

[17] KASCADE collaboration, *KASCADE measurements of energy spectra for elemental groups of cosmic rays: Results and open problems*, *Astropart. Phys.* **24** (2005) 1 [`astro-ph/0505413`].

[18] KASCADE collaboration, *Energy Spectra of Elemental Groups of Cosmic Rays: Update on the KASCADE Unfolding Analysis*, *Astropart. Phys.* **31** (2009) 86 [`0812.0322`].

[19] A. Turundaevskiy, D. Karmanov, I. Kovalev, I. Kudryashov, A. Kurganov, A. Panov et al., *The cosmic ray all-particles spectrum from the nucleon experiment in comparison with ground-based experiments data*, *Advances in Space Research* **70** (2022) 2696.

[20] PAMELA collaboration, *PAMELA Measurements of Cosmic-ray Proton and Helium Spectra*, *Science* **332** (2011) 69 [`1103.4055`].

[21] TELESCOPE ARRAY collaboration, *The surface detector array of the Telescope Array experiment*, *Nucl. Instrum. Meth. A* **689** (2013) 87 [`1201.4964`].

[22] TIBET III collaboration, *The All-particle spectrum of primary cosmic rays in the wide energy range from* $10^{14}$ *eV to* $10^{17}$ *eV observed with the Tibet-III air-shower array*, *Astrophys. J.* **678** (2008) 1165 [`0801.1803`].

[23] TUNKA-REX collaboration, *Radio measurements of the energy and the depth of the shower maximum of cosmic-ray air showers by Tunka-Rex*, *JCAP* **01** (2016) 052 [`1509.05652`].

[24] VERITAS collaboration, *The first VERITAS telescope*, *Astropart. Phys.* **25** (2006) 391 [`astro-ph/0604119`].

[25] C. Evoli, *The cosmic-ray energy spectrum*, 2020. 10.5281/zenodo.4396125.

[26] Abu-Zayyad, T. and Ivanov, D. and Jui, C. C. H. and Kim, J. H. and Matthews, J. N. and Smith, J. D. and Thomas, S. B. and Thomson, G. B. and Zundel, Z., *The Knee and the Second Knee of the Cosmic-Ray Energy Spectrum*, *arXiv* (2018) [`1803.07052`].

[27] W.D. Apel et al., *KASCADE-Grande measurements of energy spectra for elemental groups of cosmic rays*, *Astropart. Phys.* **47** (2013) 54 [`1306.6283`].

[28] X.-J. Lv, X.-J. Bi, K. Fang, Y.-Q. Guo, H.-H. He, L.-L. Ma et al., *Precise measurement of the cosmic-ray spectrum and $< \ln a >$ by lhaaso: Connecting the galactic to the extragalactic components*, *Astrophys. J.* **979** (2025) 225 [`2403.11832`].

[29] K. Fujisue, H. Dembinski, R. Engel and A. Fedynitch, *Global Spline Fit (GSF) 2024*, in *7th International Symposium on Ultra High Energy Cosmic Rays (UHECR2024)*, vol. 484 of *Proceedings of Science*, p. 087, 2025, DOI.

[30] A. Sandage and G.A. Tammann, *Absolute magnitude calibrations of population i and ii cepheids and other pulsating variables in the instability strip of the hertzsprung-russell diagram*, *Annual Review of Astronomy and Astrophysics* **44** (2006) 93.

[31] L.A. Anchordoqui, *Ultra-High-Energy Cosmic Rays*, *Phys. Rept.* **801** (2019) 1 [`1807.09645`].

[32] A. Bell, K. Schure, B. Reville and G. Giacinti, *Cosmic ray acceleration and escape from supernova remnants*, *Mon. Not. Roy. Astron. Soc.* **431** (2013) 415 [`1301.7264`].

[33] K.V. Ptitsyna and S.V. Troitsky, *Physical conditions in potential sources of ultra-high-energy cosmic rays. I. Updated Hillas plot and radiation-loss constraints*, *Phys. Usp.* **53** (2010) 691 [`0808.0367`].

[34] AMS collaboration, *Precision Measurement of the Boron to Carbon Flux Ratio in Cosmic Rays from 1.9 GV to 2.6 TV with the Alpha Magnetic Spectrometer on the International Space Station*, *Phys. Rev. Lett.* **117** (2016) 231102.

[35] ICECUBE collaboration, *Cosmic Ray Anisotropy with 11 Years of IceCube Data*, *PoS* **ICRC2023** (2023) 360 [`2308.02331`].

[36] PIERRE AUGER collaboration, *An Indication of anisotropy in arrival directions of ultra-high-energy cosmic rays through comparison to the flux pattern of extragalactic gamma-ray sources*, *Astrophys. J. Lett.* **853** (2018) L29 [`1801.06160`].

[37] M. Breuhaus, J.A. Hinton, V. Joshi, B. Reville and H. Schoorlemmer, *Galactic gamma-ray and neutrino emission from interacting cosmic-ray nuclei*, *Astron. Astrophys.* **661** (2022) A72 [`2201.03984`].

[38] V. Lenok, *Measurement of the Cosmic-Ray Energy Spectrum Using a Novel Approach to Model the Aperture of Radio Arrays*, Ph.D. thesis, Karlsruher Institut für Technologie (KIT), 2022. 10.5445/IR/1000143479.

[39] A. Zilles, *Introduction to Cosmic Rays and Extensive Air Showers*, Springer International Publishing, Cham (2017), 10.1007/978-3-319-63411-1.

[40] D. Heck, J. Knapp, J.N. Capdevielle, G. Schatz and T. Thouw, *CORSIKA: A Monte Carlo code to simulate extensive air showers*, .

[41] J. Oehlschläger and P.D.R. Engel, *Corsika shower images*, 2015.

[42] ICECUBE collaboration, *Search for PeV Gamma-Ray Emission from the Southern Hemisphere with 5 Years of Data from the IceCube Observatory*, *Astrophys. J.* **891** (2019) 9 [`1908.09918`].

[43] M.G. Aartsen et al., *Search for galactic pev gamma rays with the icecube neutrino observatory*, *Physical Review D* **87** (2013) .

[44] T.L. collaboration, *Ultrahigh-energy photons up to 1.4 petaelectronvolts from 12 $\gamma$-ray galactic sources*, *Nature* **594** (2021) 33.

[45] T.L. collaboration, *Peta–electron volt gamma-ray emission from the crab nebula*, *Science* **373** (2021) 425 [`https://www.science.org/doi/pdf/10.1126/science.abg5137`].

[46] W. Li, T.-Q. Huang, D. Xu and H. He, *Search for Neutrino Emission from the Cygnus Bubble Based on LHAASO $\gamma$-Ray Observations*, *Astrophys. J.* **969** (2024) 6 [`2402.17352`].

[47] LHAASO collaboration, *The First LHAASO Catalog of Gamma-Ray Sources*, *Astrophys. J. Suppl.* **271** (2024) 25 [`2305.17030`].

[48] LHAASO collaboration, *Measurement of Ultra-High-Energy Diffuse Gamma-Ray Emission of the Galactic Plane from 10 TeV to 1 PeV with LHAASO-KM2A*, *Phys. Rev. Lett.* **131** (2023) 151001 [`2305.05372`].

[49] IceCube collaboration, *In situ estimation of ice crystal properties at the South Pole using LED calibration data from the IceCube Neutrino Observatory*, *The Cryosphere* **18** (2024) 75.

[50] IceCube collaboration, *Neutrino Emission from the direction of the blazar TXS 0506+056 prior to the IceCube-170922A alert*, *Science* **361** (2018) 147.

[51] IceCube collaboration, *Characterization of the astrophysical diffuse neutrino flux using starting track events in IceCube*, *Phys. Rev. D* **110** (2024) 022001 [`2402.18026`].

[52] IceCube collaboration, *Recent neutrino oscillation result with the IceCube experiment*, in *38th International Cosmic Ray Conference*, 2023 [`2307.15855`].

[53] IceCube collaboration, *The IceCube Neutrino Observatory: Instrumentation and Online Systems*, *JINST* **12** (2017) P03012 [`1612.05093`].

[54] IceCube collaboration, *Highlights from the IceCube Neutrino Observatory*, *PoS* **ICRC2023** (2024) 017 [`2310.12840`].

[55] IceCube collaboration, *Study of mass composition of cosmic rays with IceTop and IceCube*, *PoS* **ICRC2021** (2021) 323 [`2107.09626`].

[56] IceCube collaboration, *Observation of Cosmic-Ray Anisotropy in the Southern Hemisphere with 12 yr of Data Collected by the IceCube Neutrino Observatory*, *Astrophys. J.* **981** (2025) 182 [`2412.05046`].

[57] IceCube collaboration, *Seasonal variation of atmospheric muons in IceCube*, *PoS* **ICRC2019** (2020) 894 [`1909.01406`].

[58] IceCube collaboration, *IceTop: The surface component of IceCube*, *Nucl. Instrum. Meth. A* **700** (2013) 188 [`1207.6326`].

[59] IceCube collaboration, *The Effect of Snow Accumulation on Signals in IceTop*, in *33rd International Cosmic Ray Conference*, p. 1106, 2013.

[60] S. Bravo, *IceCube Upgrade for precision neutrino physics and astrophysics kicks off*, 2018.

[61] A.S. Leszczyńska, *Potential of the IceTop Enhancement with a Scintillation Detector Array*, Ph.D. thesis, Karlsruher Institut für Technologie (KIT), 2021. 10.5445/IR/1000131245.

[62] IceCube collaboration, *Status and plans for the instrumentation of the IceCube Surface Array Enhancement*, *PoS* **ICRC2023** (2023) 342 [`2402.17854`].

[63] ICECUBE collaboration, IceCube, “Internal material.”

[64] ICECUBE-GEN2 collaboration, R. Abbasi et al., *IceCube-Gen2 Technical Design: The IceCube-Gen2 Neutrino Observatory*, 2024.

[65] ICECUBE-GEN2 collaboration, *IceCube-Gen2: the window to the extreme Universe*, *J. Phys. G* **48** (2021) 060501 [`2008.04323`].

[66] J.A. Aguilar et al., *The Next-Generation Radio Neutrino Observatory – Multi-Messenger Neutrino Astrophysics at Extreme Energies*, 2019.

[67] DESY, “https://www.desy.de.”

[68] J.A. et all, *Geant4 developments and applications*, *IEEE Transactions on Nuclear Science* **53** (2006) 270.

[69] R. Engel, F. Riehn, A. Fedynitch, T.K. Gaisser and T. Stanev, *The hadronic interaction model Sibyll – past, present and future*, *EPJ Web Conf.* **145** (2017) 08001.

[70] FLUKA collaboration, *The FLUKA code: Overview and new developments*, *EPJ Nuclear Sci. Technol.* **10** (2024) 16.

[71] E.-J. Ahn, R. Engel, T.K. Gaisser, P. Lipari and T. Stanev, *Cosmic ray interaction event generator SIBYLL 2.1*, *Phys. Rev. D* **80** (2009) 094003 [`0906.4113`].

[72] Feusels, Tom, *Measurement of cosmic ray composition and energy spectrum between 1PeV and 1EeV with IceTop and IceCube*, Ph.D. thesis, Ghent University, 2013.

[73] “This work was performed on the horeka supercomputer funded by the ministry of science, research and the arts baden-württemberg and by the federal ministry of education and research.”

[74] ICECUBE collaboration, IceCube, “https://github.com/icecube/simweights.”

[75] T.K. Gaisser, *Spectrum of cosmic-ray nucleons, kaon production, and the atmospheric muon charge ratio*, *Astropart. Phys.* **35** (2012) 801 [`1111.6675`].

[76] S. Vergara Carrasco, *Low-energy cosmic-ray and gamma-ray air shower simulation study using icetop*, Master’s thesis, University of Canterbury, 2024, doi.org/10.26021/15452.

[77] ICECUBE collaboration, *A multi-detector EAS reconstruction framework for IceCube*, *PoS* **ICRC2023** (2023) 366.

[78] IceCube collaboration, *A Two-Component Lateral Distribution Function for the Reconstruction of Air-Shower Events in IceTop*, *PoS* **ICRC2023** (2023) 357 [`2309.00741`].

[79] "Private discussion with Prof. Katherine Rawlins and Julian Saffer."

[80] P. Virtanen, R. Gommers, T.E. Oliphant and et al., *SciPy 1.0: Fundamental algorithms for scientific computing in python*, *Nature Methods* **17** (2020) 261.

[81] F. Bontempo, "https://github.com/fedbont94."

[82] J. Saffer, *Spectrum of PeV Cosmic-Ray Protons and Helium Nuclei with IceCube (Preliminary title)*, Ph.D. thesis, Karlsruher Institut für Technologie (KIT), 2025.

[83] F. Bontempo and for the IceCube collaboration, *Improving the gamma-hadron separation for air showers at the icecube neutrino observatory*, 2022. 10.5281/zenodo.6301067.

[84] F. Bontempo and for the IceCube collaboration, *New approaches for gamma-hadron separation at the icecube neutrino observatory*, 2023. 10.1051/epjconf/202328004004.

[85] F. Bontempo and for the IceCube collaboration, "Reconstruction and identification methods of sub-pev gamma rays at the icecube neutrino observatory." Presented at TEVPA 2023, Napoli, Italy, https://agenda.infn.it/event/33457/contributions/204832/, 2023.

[86] T.-P. Li and Y.-Q. Ma, *Analysis methods for results in gamma-ray astronomy*, *Astrophysical Journal, Part 1 (ISSN 0004-637X), vol. 272, Sept. 1, 1983, p. 317-324.* **272** (1983) 317.

[87] C.R. Harris et al., *Array programming with numpy*, *Nature* **585** (2020) 357–362.

[88] J. Braun, J. Dumm, F. De Palma, C. Finley, A. Karle and T. Montaruli, *Methods for point source analysis in high energy neutrino telescopes*, *Astropart. Phys.* **29** (2008) 299 [`0801.1604`].

[89] F. Bontempo, "Gamma-rays point-source search." https://wiki.icecube.wisc.edu/index.php/Gamma-rays_point-source_search.

[90] F. Bontempo, "Gamma-hadron separation plot approval icrc2025." https://wiki.icecube.wisc.edu/index.php/Gamma-Hadron_separation_plot_approval_ICRC2025.

[91] F. Bontempo, "Laputop3s3s." https://wiki.icecube.wisc.edu/index.php/Laputop3s3s.

# F. List of Figures

# G. List of Tables

# Acknowledgement

First and foremost, I would like to express my deepest gratitude to Prof. Dr. Frank G. Schröder for this unique opportunity, his invaluable guidance, support, and encouragement throughout the course of this work. His insight and mentorship have been instrumental to my academic growth and the completion of this project.

I am also thankful to Prof. Dr. Ralph Engel for always bringing fresh ideas to the research and trusting me in the process, especially when I was doubting myself. And thanks to Dr. Andreas Haungs for his helpful discussions, suggestions, and feedback, and for bringing positivity with his laugh, in particular in the lowest moments.

I would like to thank the IceCube Collaboration as a whole, and in particular the working group leads Dennis, Agnieszka, Matthias, and Stef. Special thanks go to Prof. Dr. Katherine Rawlins, who helped immensely and was always available, particularly with the SLC calibration and the development of Laputop3s3s. And to my reviewer, Paolo Deisati. I am also grateful to Chiara, Will, and Lisa for their assistance with the point-source analysis.

I am grateful to you all at KIT — Sabine, Anna, Bianca, Doris, Mo, Darko, Markus, Donghwa, and David — who contributed in different ways throughout this journey and know well the importance of their help. I also thank the colleagues at DESY, in particular Markus and Timo, for providing the final funding support that allowed me to complete my PhD.

A heartfelt thank you goes to my colleagues and fellow researchers at the Institute and in the broader astroparticle physics community. Thanks also to the PostDocs, Hrvoje and Alan, who made my entry into the collaboration smoother and more welcoming. Paras for the countless discussions, and Julian for checking the simulation set and making sure that the collaboration was aware of that.

To my fellow (and former) PhD students and PostDocs — Roxanne, Sara, Felix, Mark, Wenjie, Vika, Nikos, Keito, Simon, Marie, Steffen, Berenika, Fiona, Emily, Olena, Tobias, Luca, Robin, Fahim, and in particular to Lukas, who made the bitter days sweeter with his baking, shared the dancing journey and finally made sure I watched the Star Wars saga. Thank you to my current office mates for listening to my not-always-happy moments Marvin and Luca. And thank you to all the others whose names I might forget — thank you for sharing this journey. And thanks to Ben for making my US stay super enjoyable!

To the former KSETA representative who shared the experience with me, Lucas, Kathrin, and Robert, thank you! It was worth it!

Thanks to the particle physics colleagues from Campus South, Alessandro, Stefan, Sauro(n), Giacomo, Sofaia, Greta, Alexander, Cedric, Isa, Jorst, Karo, Kylian, Lars, Lea, Nils and all the others who I did not forget to mention but could not because of the limited ink available.

Special thanks to Pranav, who helped with coding, provided incredibly useful feedback, and most importantly, introduced me to the one and only holy Deivam, spreading the religion like a true prophet; to Jelena for *the German*, the amazing cover design, and the thorough proofreading; to Shefali for understanding my thoughts, translating them into proper sentences, and helping me improve my writing; to Tista (sweet as her beloved tiramisu) for the incredible help in summarizing the point-source analysis in an understandable manner; and to Megha for being such a good listener and making me aware of how good I am at "ending" things. I want to thank all of you for your countless hours spent revising the thesis, checking endless mistakes, and providing unwavering support and patience. You truly made the PhD journey enjoyable.

Thank you to Sebastian, who, despite the distance, performed an outstanding job during all these years, quickly grasping the basics and working on every topic we faced together. Your work and support have been invaluable; never stop! Thanks also to Vaghdan and Jacob for trusting me to supervise their projects.

A special thanks to my former colleague and friend Vova, who supported and helped regardless of the topic discussed, and who was always there during both the good and difficult moments.

Beyond academia, I am deeply grateful to my family — my mom, dad, and brother Paolo — for their unwavering support, patience, and encouragement. Their belief in me has been a constant source of strength. My aunt Anita, uncle Romeo, cousin Nila, grandpa Nicola, and also I must remember my other grandparents, who were there when this journey began, but sadly not at its conclusion.

Finally, I would like to thank my friends in Italy, Angelo, Giulio, Riccardo, Francesca, Paolo, Simona, and Piero. My Friends in Erlangen, Sefora, Sebastian, Samuele, Benedetta, Philipp, Daniel, Marlene, and of course you, Luis, you taught me to never give up! Thank you to my ex-colleagues and now pizza-friends, Andreas, Dennis, Franzi, Florian, Jo, Markus, Naomi, and Basti. To all of you whom I may have forgotten to mention, both near and far, apologies and THANK YOU!

Closing remarks and thanks to you, Lorenzo, for your countless moments of listening and support that provided me with balance, laughter, and perspective whenever it was most needed, and together with Amina, Emiliano and FraSu, for helping me overcome stress and difficult times with humor and friendship.

Also, thanks to chess and gym for always being there and helping me get back on my feet, especially when my calves alone weren't enough to carry me.
A special thanks also to ChatGPT, Gemini, and Grammarly for their assistance during the writing process, especially for improving writing correctness (also of this acknowledgment :P).

Federico Bontempo
June 25, 2025

The authors gratefully acknowledge the computing time provided on the high-performance computer HoreKa by the National High-Performance Computing Center at KIT (NHRKIT). This center is jointly supported by the Federal Ministry of Education and Research and the Ministry of Science, Research and the Arts of Baden-Württemberg, as part of the National High-Performance Computing (NHR) joint funding program (`https://www.nhr-verein.de/en/our-partners`). HoreKa is partly funded by the German Research Foundation (DFG).
This project has received funding from the European Research Council (ERC) under the European Union's Horizon 2020 research and innovation program (grant agreement No 802729)
The last six months have been supported by the common activities of KIT and DESY in the IceCube-Upgrade project

## Statutory Declaration

I declare that I have developed and written the enclosed Doctoral Thesis completely by myself, and have not used sources or means without declaration in the text. The Doctoral Thesis was not used in the same or in a similar version to achieve an academic grading or is being published elsewhere.

Date

Bontempo, Federico